Microstructural effects on fatigue damage evolution in Advanced High Strength Sheet (AHSS) steels

A Dissertation
Presented to
The Academic Faculty

By

Anshul Godha

In Partial Fulfillment of the
Requirements for the Degree
Doctor of Philosophy in the
School of Materials Science and Engineering

Georgia Institute of Technology

May 2015

Microstructural effects on fatigue damage evolution
in Advanced High Strength Sheet (AHSS) steels

Approved by:

Dr. Arun M. Gokhale, Adviser
School of Materials Science and Engineering
Georgia Institute of Technology

Dr. Shrikant P. Bhat
ArcelorMittal Global R&D
East Chicago, Indiana

Dr. Stephen D. Antolovich
School of Materials Science and Engineering
Georgia Institute of Technology

Dr. Preet Singh
School of Materials Science and Engineering
Georgia Institute of Technology

Dr. Kimberley E. Kurtis
School of Civil and Environmental Engineering
Georgia Institute of Technology

Date approved: September 24, 2014

Acknowledgements

The present work has been made possible due to the constant help and support of a number of people and institutions. I will try to acknowledge their contributions in the following lines.

First and foremost, I must mention the contribution of my doctoral adviser, Dr. Arun Gokhale. His technical expertise in the field of stereology and quantitative microscopy has proved to be a source of constant inspiration. I have tried my best to learn as much as I can from him during my time as a graduate student. My interest in the subject has grown leaps and bounds ever since I joined as a student in his group. My first couple of years were a struggle trying to formulate a feasible problem statement but he never pushed me into doing anything I did not feel comfortable with. He was always accessible for any problems or questions I faced, and I will always be thankful for that. His motivation was always positive and constructive and I believe it really inspired me to give my best every day. Apart from his technical expertise, I always looked at him as a mentor and guide in my personal life and in honing my soft skills such as public speaking, technical writing and networking. For all of these, I am extremely grateful to him and hope that I can prove myself to be a worthy alumnus of his lab.

Next, I would like to recognize the contribution of ArcelorMittal Global R&D, East Chicago who were the project sponsors for this work. They not only provided financial support but also constant cooperation in terms of raw samples as well as crucial data and expertise, all of which were critical for the successful completion of this work. This is a good time to acknowledge the immense contribution of Dr. Shrikant Bhat from

ArcelorMittal Global R&D. Dr. Bhat has practically been my co-mentor right from the beginning of this work. He is an extremely well known authority in the field of High Strength Steels and fatigue and I consider myself blessed to have had a chance to know him and learn from him. He was instrumental in the formulating of the problem statement that was of practically significance for the industry, something that I am proud of. He was also responsible for making raw materials available to me and for helping me clear my concepts of steel metallurgy, fatigue of metals as well as interpreting my results. Also noteworthy is his contribution in bringing this thesis to fruition.

I would also like to acknowledge the constant help and feedback I have received from my committee members, Dr. Stephen Antolovich, Dr. Preet Singh and Dr. Kimberly Kurtis. I would like to thank all of them and acknowledge that it has been my honor to have been associated with them both in a technical and personal capacity.

Next I want to thank the Materials Science Laboratory at the Georgia Tech Research Institute (GTRI) and especially Mr. Gautam Patel, who allowed me to use their facilities and experience in sample preparation, characterization and electron microscopy. Mr. Patel always showed keen interest in my work and was available to help me out at all times, sometimes even during the weekends and late hours of the day. In the same breath, I would like to acknowledge Mr. Richard Brown who, despite his severe health problems, went the extra mile to train me on mechanical testing and fatigue analysis. It is with his help that I feel comfortable in my ability as an experimentalist in the area of mechanical testing.

My lab colleagues, especially Dr. Ashok Gurumurthy and Ranbir Singh Jamwal have been both a source of help and encouragement over the years. I sincerely thank them and wish them the best in their future endeavors.

I would also like to mention the help I received from my friends, especially Anurag Goyal, Hardik Shah, Bharath Ravi and Ajay Srinivasamurthy, my old roommates. They proved to be sources of inspiration and intellectual development as well as a sink to vent out my frustrations during the course of this work.

The last two years of this work became a pleasure largely due to the encouragement provided by my wife, Paridhi Jain. The constructive feedback and fresh perspective she provided has undoubtedly helped me become a better researcher as well as a better person. She has always been there when I needed her and for this, I will always be grateful.

Last, but not the least, I would like profoundly thank my family, especially my parents who have, over the years, instilled in me the values of hard work, sincerity, patience and pursuit of excellence. It was due to their encouragement that I could pursue my field of interest get the best possible research experience. I hope that by this work I have, at least partially, vindicated their confidence in me.

The list of the people I feel indebted to for enabling me to produce this work is very long and I cannot possible thank them enough in these pages. But I hope that they all continue to support me in future and help me reach my potential, both as a person and as a researcher.

Table of Contents

List of Tables

List of Figures

Summary

An understanding of the damage evolution prior to crack initiation in advanced structural materials is of vital importance to the fatigue community in both academia and industry. Features known as the Persistent Slip Bands (PSBs) play an integral role in this damage evolution. Therefore, PSBs have been the focus of a lot of science-based investigations over the years. However, most existing studies in this area are restricted to analysis of PSBs in single crystal face centered cubic (FCC) materials. Moreover, these studies lack a quantitative analysis of the evolution of the fatigue damage (or PSBs) as a function of the material microstructure. This is especially true for relatively modern materials such as the Advanced High Strength Structural (AHSS) steels that are gaining a lot of importance in the automotive sector. Accordingly, the objective of this research is to quantitatively characterize evolution of PSBs in three AHSS steels having different microstructures as a function of number of fatigue cycles and strain amplitude. For this purpose strain controlled interrupted fatigue tests have been performed on two dual phase steels (DP-590 and DP-980) having different relative amounts of tempered martensite and a ferritic high strength low alloy steel (HR-590). Digital image analysis and Stereology have been used for unbiased quantitative characterization of the evolution of global geometry of the PSB colonies as function of number of fatigue cycles and strain amplitude. Evolution of PSB colonies has been couched in terms of variation of PSB colony volume fraction and total surface area unit volume, and total surface area of individual PSBs per unit volume and three-dimensional angular orientation distribution of the PSBs. For this purpose, new stereological techniques have been developed for estimation of the three-dimensional angular orientation distribution. The stereological

data reveal that during strain controlled in these AHSS steels, volume fraction of the PSB colonies varies *linearly* with the their total surface area per unit volume. Detailed analysis of the stereological data leads to a simple geometric model for evolution of the PSB colonies in the three AHSS steels, which accounts for all observed data trends.

Chapter 1

Introduction, Motivation, and Objectives

Structural members are often subjected to cyclic stresses in service. Consequently, there have been many investigations on the effects of loading conditions, environmental parameters, chemistry, and microstructure on the mechanical response of structural materials under cyclic loads [1-7]. A significant part of this literature deals with the mechanisms of initiation of fatigue crack(s) in an initially crack-free material subjected to fatigue stresses [8-15]. Understanding of fatigue crack initiation is particularly of interest in the engineering applications where useful component life is the period prior to the fatigue crack initiation.

It is well-known that substantial damage evolution precedes and ultimately causes fatigue crack initiation [1, 16-19]. In metals and alloys, plastic deformation under cyclic loads often gives rise to the formation and growth of *distinct* regions of concentrated slip and plastic strain localization having a *unique* dislocation structure called persistent slip bands (PSBs). These damage features are often the sites of fatigue crack initiation. As a result, there have been a large number of studies on the formation and growth of PSBs using numerous techniques including optical, electron, and atomic force microscopy [13, 20-24]. A majority of these investigations are on *single crystals* of FCC metals like Cu [22, 25-28]. There have been a few studies on PSBs in polycrystalline multi-phase alloys where the matrix does not have FCC crystal structure [13, 16, 23, 24, 29-33]. On the other hand, many engineering alloys such as structural carbon steels, where fatigue crack initiation is of prime concern, are polycrystalline and multi-phase, and the dominant

phases are not necessarily FCC. Therefore, it is of interest to systematically investigate evolution of PSB damage and its relationships to microstructure in such materials of technological importance.

It is important to point out that majority of the studies on PSBs reported in the literature are of qualitative nature. None of the investigations report statistically unbiased estimations of ensemble averaged geometric attributes of *populations* of PSBs in three-dimensional microstructural space; relationships of such attributes with the material microstructure; and their quantitative linkages to the fatigue crack initiation. Such quantitative microstructural description of damage evolution leading to fatigue crack initiation is likely to provide new insights into our understanding of the *science* of fatigue crack initiation. Accordingly, the focus of this work is on the development of a stereology and digital image processing based methodology for unbiased quantitative description of three-dimensional PSB damage evolution preceding fatigue crack initiation and application of the methodology to understand the damage evolution and crack initiation in polycrystalline, multi-phase, non-FCC structural alloys of technological importance.

Polycrystalline Advanced High Strength Sheet (AHSS) steels are technologically important. These steels are being used for commercial applications where monotonic mechanical properties such as strength and ductility as well as fatigue life and fatigue crack initiation are of significant practical concern. For several applications of AHSS steels, the *useful component life* is considered to be the period prior to crack initiation. As numerous processing routes and compositions are technologically feasible for AHSS steels, it is possible to commercially produce two (or more) types of AHSS steels that have comparable monotonic mechanical properties but very different microstructures. In

such cases, it is of interest to understand the effects of microstructure on the damage evolution preceding fatigue crack initiation so that the microstructure can be designed to obtain the desired monotonic mechanical properties and required resistance to fatigue crack initiation. Accordingly, in the present work, a stereology and digital image processing based methodology has been applied to quantitatively characterize three-dimensional PSB damage evolution in AHSS steels. This information helps in understanding the effects of the microstructural parameters such as volume fractions of ferrite and martensite on the fatigue damage evolution and its linkages to the fatigue crack initiation.

For the present research, the materials chosen are two types of AHSS steels, namely, the hot-rolled High Strength Low Alloy (HSLA) steels (HR590) and the cold-rolled Dual Phase (DP) steels (DP590 and DP980). HSLA steels are almost entirely ferritic and low-carbon precipitation hardened steels with close to 1.5% manganese, strengthened by small additions of elements such as niobium, vanadium and titanium and manufactured by controlled thermomechanical processing. The DP steels, on the other hand, provide a unique opportunity to study the effects of a second phase on fatigue crack initiation. This is mainly due to the presence of two microstructural constituents, ferrite and tempered martensite. DP steels of different compositions containing 20 to 80% tempered martensite can be commercially produced, and different combinations of monotonic mechanical properties can be achieved via appropriate design of steel chemistry and processing. Therefore, it is of interest to understand the effects of martensite volume fraction on the PSB evolution and fatigue crack initiation in these steels.

The present work involves a combination of theoretical and experimental work. The specific objectives and tasks of the research are as follows.

- Development of a theoretical framework for statistically unbiased quantitative description of PSB damage evolution in terms of ensemble averaged geometric attributes of evolving PSB populations.
- Observations of PSB damage at fatigue specimen surfaces using scanning electron microscopy and atomic force microscopy.
- Quantitative characterization of PSB damage evolution as a function of the number of fatigue cycles and strain amplitude during uniaxial fully-reversed (R= -1) strain-controlled fatigue in HR 590, DP 590 and DP 980 steels.
- Quantitative characterization of the effects of ferrite and martensite volume fractions on PSB damage evolution and fatigue crack initiation.
- Application of quantitative experimental data to develop a physics-based model to explain observed effects of AHSS steel microstructure on PSB damage evolution and fatigue crack initiation.

The next chapter presents a critical review of the literature on fatigue crack initiation and damage evolution, and a background on physical metallurgy of AHSS steels and relevant stereology and image analysis techniques. The theoretical development on the estimation of 3-D angular orientation distribution of PSBs is presented in the subsequent chapter, and that is followed by details of the experimental work along with discussion and summary of the results obtained. Finally the conclusions drawn from the research are mentioned in the last chapter.

Chapter 2

Background and Literature Review

The objective of this thesis is to conduct systematic quantitative investigation of the effects of microstructure on the damage evolution preceding fatigue crack initiation in Advanced High Strength Sheet (AHSS) steels. This work builds on the current literature in the field. Consequently, a critical review of the literature on damage evolution and fatigue crack initiation is presented in this Chapter. The present work involves extensive applications of stereology and digital image analysis for quantitative microstructure characterization, and therefore, a background on these techniques is also presented. These methodologies are utilized in the experimental work reported in the next chapter.

2.1 Advanced High Strength Sheet (AHSS) steels

AHSS steels are low-carbon low-alloy structural steels where microstructure is optimized using a variety of chemical compositions and thermo-mechanical processing methods. Due to their high strength-to-weight ratio and ductility, and excellent weldability and formability, these steels are extensively used for structural automotive applications where light-weighting is an important design criterion. With the constant need for development of materials that can provide better safety and fuel-efficiency to the automobiles, the demand for AHSS steels is projected to increase significantly over the next decade [34, 35].

Alloying elements such as C, V, Ti, Nb, Mn, Cr, Mo and Al are the most common alloying additions to commercial AHSS steels. Traditional high-strength non-AHSS

steels derive strength from high carbon concentrations via solid solution hardening. However, the high carbon content also results in poor weldability, toughness and formability. Refinement of the steel microstructure has resulted in stronger steels with lower carbon content. Such low-carbon AHSS steels achieve strengths that are comparable to traditional high- strength non-AHSS via utilizing a combination of strengthening mechanisms including solid solution hardening, precipitation hardening and/or grain-refinement. Alloying elements affect the stability of phases in steel and the kinetics of phase transformations resulting in microstructures with varying combinations of volume fraction, morphology and distribution of phases, which in turn affect material properties such as fatigue behavior. It is important to point out that it is possible to produce different microstructures that have similar monotonic strengths, but not necessarily the same fatigue response. More details about the effect of alloying elements on the fatigue behavior of steels have been reported in great detail by a number of researchers [36-40].

The thermo-mechanical processing of these steels can also play a major role in determining their microstructure and consequently their mechanical response especially fatigue behavior. For example, the initial annealing treatment is critical in determining the final grain size in AHSS steels [41]. Initial annealing is necessary for thermo-mechanical rolling in the austenite phase. The hot rolling elongates the austenite grains, providing more surface area for nucleation of ferrite and assisting in the nucleation of grain refining precipitates, thus affecting the mechanical response of these steels. Similarly, the rolling direction and heat treatment can cause the fatigue behavior to exhibit anisotropy [42]. Such anisotropy can cause the fatigue life of steels to vary

significantly depending on the loading directions. Additionally, the textured surface caused by rolling can be a source of fatigue crack initiation [43]. Several other effects of thermo-mechanical processing on fatigue response have been studied and can be found elsewhere [40, 44, 45].

Depending on the chemistry and processing route, the AHSS steels may contain ferrite, tempered martensite, bainite and/or retained austenite, and carbide phases. The different phases can also play an important role in determining the mechanical response of the steels. For example, ferrite phase provides ductility to these steels. Refinement of the ferrite grain size can also provide high strengths. The martensite and/or bainite phases provide increased strengths. These phases are relatively hard and often lead to increased dislocation activity in the nearby softer phases. This can lead to hardening and prior crack initiation under monotonic as well as cyclic loading. In steels containing carbide phases, Picas et al [46] have shown that cracks often nucleate at the primary carbides when the applied stress is higher than the fracture strength of the carbide. Even under cyclic loading, carbides can act as stress concentrators and thus localization of strain in the surrounding matrix is more likely to take place in their vicinity.

AHSS steels can be broadly divided into four groups, namely, high strength low alloy (HSLA) steels, dual phase (DP) steels, transformation induced plasticity (TRIP) steels, and twinning induced plasticity (TWIP) steels. The experimental work of the present research was performed on high strength low alloy (HSLA) steels and two varieties of dual phase (DP) steels. A brief discussion on the composition, microstructure and properties of these steels with a focus on their fatigue behavior is presented in the following sub-section.

2.1.1 *HSLA steels*

HSLA steels are micro-alloyed plain-carbon steels with <0.1% carbide and nitride formers (e.g. Nb, Ti, V etc). These alloying additions improve mechanical properties by improving abrasion, corrosion and elevated temperature oxidation resistance. These steels exhibit better weldability and increased choices of coatings. They exhibit excellent cold forming and low-temperature brittle fracture strength as well as good fatigue strength. The alloying additions also allow these steels to achieve similar monotonic strengths as high carbon steels, but with significantly higher toughness. These properties make them ideal for structural applications such as vehicle chassis, wheels, side rails etc. [47].

The microstructure of HSLA steels consists largely of ferrite grains and a very fine dispersion of alloy carbides/nitrides. Strengthening in these steels is achieved due to refinement of ferrite grain size, strain-induced precipitation of carbides/nitrides and precipitation strengthening of ferrite. Grain refinement is the preferred method because it increases both strength and toughness.

The precipitates in HSLA steels increase the strength of the material at the expense of ductility and may be detrimental to fatigue behavior in large concentrations, especially if they form a continuous network [45]. The carbides may alter fatigue life by dictating crack path morphology or arresting the crack propagation. The micro-alloying elements have also been known to improve the fatigue life of the HSLA steels as compared to similar steels without the micro-alloying elements [48].

2.1.2 *DP steels*

The DP steels have a high versatility and have become extremely popular in the automotive industry. DP steels are also plain carbon steels having continuous yield

behavior, low yield strength and larger total elongation as compared to other similar strength steels. As compared to the conventional steels, they offer better component-weight reduction, higher formability, higher bake hardenability and higher capacity to absorb crash energy. In addition they show higher work hardening rate, better bendability, better weldability and higher shelf life.

In comparison with micro-alloyed HSLA steels, DP steels have negligible amounts of micro-alloying additions. Therefore, DP steels are not designated micro-alloyed steels. The absence of micro-alloying additions in the DP steels is dictated by the fact that DP steels derive their strength primarily from the presence of martensite/bainite constituents rather than dispersion/precipitation hardening effects. The amount of the harder martensite phase increases the monotonic strength of the DP steels in a way that follows the *rule of mixtures* [6, 41] but its effect on fatigue behavior is not as straight-forward. Sherman and Davies [49, 50] and Mediratta [51] have shown that the fatigue properties of the dual phase steels such as cyclic stress levels and intermediate-to-large fatigue lives increased while fatigue notch-sensitivity decreased with increasing martensite content up to about 30% martensite. A possible reason for this could be a more uniform dislocation substructure in the ferrite matrix [52]. However beyond about 30% martensite, these properties did not show much change. This can be explained by the reduced ductility as well as increased high-energy strain fields between the martensite and the ferrite constituents.

The carbon content of the *martensite* phase further complicates the effect of martensite content on fatigue behavior of DP steels. The martensite carbon content is dependent on the initial carbon composition and processing parameters. The effect of

martensite content on the overall properties of dual phase steels has been studied quite extensively over the years. These studies have used multiple approaches for varying the martensite content within the dual phase steels. Some studies like Mediratta et al. [51] have used the same intercritical treatment for steels of different chemistry (varying the carbon or the manganese content) . The advantage of this method is that the use of similar intercritical treatment implies that the steels formed have similar carbon content within the ferrite and the martensite phases. However, the uniformity in the overall chemistry is lost in this approach. The other approach that has been used is to start with steels of the same overall chemistry and vary the intercritical heat treatment in order to generate varying volume fractions of the martensite phase [53-57]. This approach is especially useful for the automotive industry where changing the chemistry can have many undesired consequences in downstream compatibility (phosphating, painting etc.). DP steels having varying carbon content of the martensite phase are obtained in this manner. Decreasing the carbon content of the martensite creates a BCT (Body Centered Tetragonal) phase that is more compatible with the ferrite matrix. This is important because it has been shown that increased incompatibility between the phases can provide a site for crack initiation during cyclic loading [42]. As described in Chapter 4, the DP steels used in this study are of the type having similar overall carbon contents but varying *martensite* carbon content.

The distribution and morphology of the martensite/bainite phases formed as a result of the final processing may also affect the fatigue behavior of dual-phase steel. With regards to the dual phase microstructure, these changes in morphology and distribution may be attributed to 1) change in the shape of martensite and ferrite leading to improved

stress transfer, 2) work hardening, 3) deformation of ferrite grains 4) strain-induced interphase precipitation [58]. Their effect on fatigue behavior was studied by Dutta et. al. [59] who showed that microstructures containing fine globular or coarse martensite in a coarse grained ferrite matrix demonstrated exceptionally high crack growth resistance as compared to other morphologies.

2.2 Fatigue damage evolution

Typically, the fatigue damage evolution in a material comprises of the following four stages:

Stage I: Microstructural changes including formation of surface features

Stage II: Formation of microcracks

Stage III: Coalescence of microcracks to form macrocracks

Stage IV: Propagation of macrocracks leading to final failure

Vast amount of literature exists that deals with Stages III and IV that primarily constitute the crack growth regime [10, 60, 61]. However, for a lot of the applications, a majority of the life and often the *useful* life of the material is over by the time a crack initiates. The focus of this work is on the evolution of damage caused due to cyclic loading *prior* to crack initiation, particularly with respect to mechanical response of the material under cyclic loading as well as the changes in its microstructure, both on the surface as well as in the bulk.

Fatigue loading can lead to irreversible microscopic changes resulting from the accumulation of very small irreversible cyclic plastic microstrains. These irreversible microscopic changes form the basis of fatigue damage. Several factors like strain-

amplitude, crystal structure, strain rate and temperature are known to play a significant role in determining the nature of fatigue damage evolution. Some of these are discussed below:

A) Effect of strain amplitude: The mechanism of crack initiation can be a function of the applied strain amplitude. Hadianfard [62] showed that at high strain amplitudes the martensite particle fracture led to the initiation of the crack while at low strain amplitudes, cracks initiated either at the ferrite-martensite interfaces or within the ferrite grains. Similar observations were made earlier by Llanes et al. [44] . Similarly, it has been shown that as the strain amplitude increased, the tendency of cracking changed from transgranular to intergranular [63, 64] in polycrystalline α-iron. However, in HSLA steels, cracking along the grain boundaries was very rare and cracking at the grain interior was largely the dominant cracking mechanism even at high strain amplitudes [7, 29, 63]. This could be either because of small grain size in these steels and/or due to coherent precipitates promoting strain localization and cracking at slip bands within the grain interior [65, 66].

B) Effect of crystal structure and alloying elements: The theory behind the initiation of cracks has been formulated mainly using FCC materials [16, 67, 68]. The behavior of BCC materials containing interstitial impurities (like in steels) is quite similar to the FCC materials but quite different from pure BCC behavior. This is because the behavior of dislocations, especially the screw dislocations, is very different in a BCC structure containing interstitials as compared to a pure BCC material. In pure BCC materials at room temperature, the mobility of screw

dislocations is lower as compared to the edge dislocations. This is because of the extended core structure of screw dislocations in a pure BCC structure [69]. The presence of sessile screw dislocations means that under room temperature conditions, dislocation glide occurring during the fatigue process takes place mainly by the glide of edge dislocations. This also means that higher stresses are required to induce mobility in the screw dislocations, which, in turn, increases the yield stress at low temperatures, a characteristic of BCC materials. Another characteristic of pure BCC materials is that at high plastic strain amplitudes, bulk cyclic hardening occurs with an increasing participation of screw dislocations. These screw dislocations glide in different slip planes in tension and compression leading to "*slip plane asymmetry"*. This slip plane asymmetry manifests itself as marked shape changes in the case of single crystals [70-72](cross sections of initially round specimens becoming increasingly elliptical during cyclic loading) and development of characteristic surface roughness in the case of polycrystals [71]. Addition of impurities, especially interstitial carbon atoms leads to a preferential decrease in the mobility of the edge dislocations in a pure BCC structure caused by "dynamic strain aging" [73]. This causes the mobilities of the edge and the screw dislocations to become comparable, a behavior similar to FCC materials.

C) <u>Effect of crystallographic orientation:</u> Interestingly, it has been observed that the crystallographic orientation, with respect to the loading direction, has no significant impact on the total fatigue life of a material, irrespective of its crystal structure [19, 74, 75] (as cited in [76]). However, its impact on the fatigue crack

initiation can be quite significant, especially for BCC materials. This is due to the possibility of slip plane asymmetry in the BCC materials. Bhat et al. [76] have proposed that there must be a similar but opposite effect of the crystal orientation in the crack propagation stage such that it compensates for the earlier observations.

D) Effect of temperature and strain rate: Temperature and strain rate can influence the fatigue behavior during cyclic loading. For example, Krishnadev et al. [77] showed that in case of Nb-Mo "acicular ferrite" as well as for high Nb HSLA steels, the fatigue life increased at temperatures lower than the transition temperatures of the steels, primarily due to the improvement in the tensile strength of the materials. The nature of dislocation substructure that developed due to cyclic loading was also affected by temperature as was shown for single crystal copper by Boehme et al. [78] and for nickel-based superalloys by Gabb et al. [79] and Obrtlik et al. [80]. Similarity of slip behavior has been reported by Wilson and Tromanas [73] for low carbon steels at slightly elevated temperatures (between 60^0 C and 130^0 C) and by Mughrabi et al. [16] for α-iron-30 ppm carbon at 'low' strain rates (2.5×10^{-5} s^{-1}). This was attributed to the nearly equal mobilities of the edge and the screw dislocations at lower strain rates and temperatures greater than transition temperature, T_0 for the materials. This was in contrast to the behavior of α-iron-30 ppm carbon at high strain rate (10^{-2} s^{-1}) when the behavior became more similar to pure α-iron [81].

2.2.1 *Crack initiation*

The term crack initiation can have different meanings for different people. The detection of a crack is very much dependent on the resolution of the observational techniques employed to detect cracking [82]. For an engineer, initiation is likely to mean the smallest crack that can be determined using a reliable non-destructive evaluation (NDE) technique [5]. For some scientists, initiation sets the limit on the minimum size of a small fatigue crack, assuming that the component was initially crack-free [83]. In this respect, Mughrabi [84] proposed to define the initiation process to include in it all stages of the cracking process until the crack becomes large enough to describe its propagation by fracture mechanics. The definition implied that the crack initiation period would also include early slow crack growth. A similar description of the transition from the crack nucleation stage to the crack propagation stage based on the surface crack length at which the theory of fracture mechanics become applicable has been suggested by Lukas [85]. While these definitions may seem arbitrary, it is important to state clearly what is meant by initiation and propagation.

Some authors have used a different approach based on energetics to detect crack initiation. Mura and co-workers [86-88] as well as some other works [76, 89] have based this approach on the concept of Gibbs free energy change accompanying the transition of the bulk deformation stage to that containing microcracks. Consequently according to this approach, when the energy accumulated within the slip bands reaches a critical value given by the maximum in the plot of Gibbs free energy change, ΔG, v/s number of fatigue cycles, N, a fatigue crack spontaneously nucleates.

2.2.2 *Mechanical response due to fatigue*

A) HSLA steels: The mechanical response to cyclic loading in HSLA steels is determined by the inherent dislocation activity [90]. Roven and Nes [91] studied the cyclic stress response of HSLA steels at varying plastic strain amplitudes. This response is shown in Figure 1. At low plastic strain ranges, a softening towards a plateau level was observed. Similar observations have also been reported elsewhere [92, 93]. This range was between 0 and 1.2% plastic strain. For higher values, the response was cyclic hardening. The cyclic softening can be attributed to the formation and spreading of dislocation sources along the gage length during the first few cycles. During this stage, even though there is an increase in the dislocation density, any consequent cyclic hardening is suppressed by the spread of the dislocations to newer areas until a saturation stage is approached. At this point, softening may still continue for a while due to the formation of soft low dislocation density channels and Persistent Slip Bands (PSBs) within a matrix of hard veins [25, 94]. More details about PSBs are presented in the next section. At high strain amplitudes, cyclic hardening was observed in the initial cycles. This was due to the work hardening caused because of the rearrangement of the dislocation structure from walls, labyrinths and cells to subgrains and microbands and from the refinement of these features with increasing plastic strain accumulation [91]. The plateau region observed for the HSLA steels from Figure 2.1 is similar to those reported by Wang and Laird [95] and Bhat and Laird [96]. Some observers such as Kettunen et al. [97] have observed that the plateau region exists only with a coarse grained material. Laird et al. [98] made similar observations and suggested that the stress gradients associated with grain incompatibility can act to suppress the plateau when the

grain size is small. Roven et al [91] have characterized the plateau region by a balancing act between the plastic strain activity in some grains and mainly elastic strain displacements in the complementary grains. Similar observations on other HSLA varieties have been made elsewhere [99, 100].

B) DP steels: The mechanical response for DP steels and the underlying dislocation activity has also been studied at great length. It has been observed that in virgin DP steels, the dislocation density decreases steeply from the region adjacent to the martensite to the center of a large ferrite grain [101, 102]. During fatigue, this heterogeneous distribution of dislocations becomes much more homogeneous to minimize energy. The cyclic stress response for DP steels can vary a lot depending on the plastic strain amplitude as well as microstructure. For steels containing ~15% martensite, continuous cyclic softening was observed for strain amplitudes <0.005 [103] due to the formation and spreading of dislocation sources at low strain.

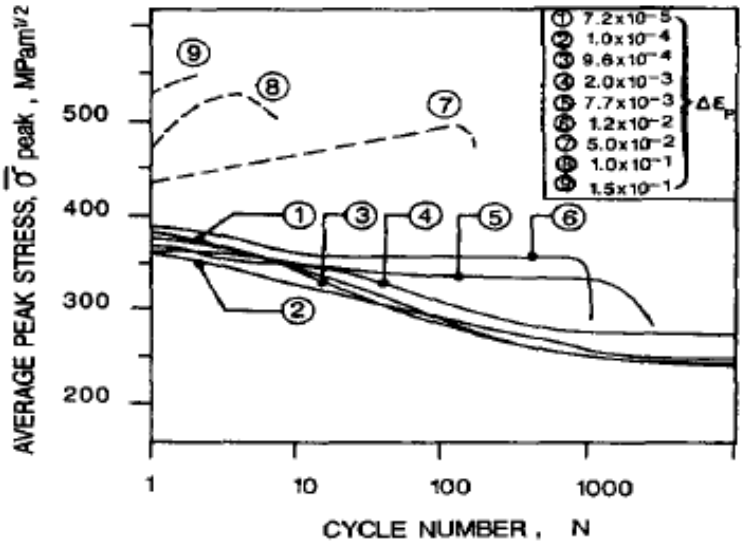

Figure 2.1: Cyclic stress response at different plastic strain ranges ($\Delta\varepsilon_p$'s). Continuous and dotted curves refer to single-strain tests and a multiple step test respectively [91].

Zhengming et al. [101] have shown that at low strain amplitudes (5.7×10^{-4}), the DP steel

specimen containing 23% martensite showed almost continual hardening over a large number of cycles, probably due to the formation of dislocation clusters. However, at higher strain amplitudes (3×10^{-3}), the specimens hardened rapidly at first followed by slight softening, probably due to the formation of dislocation walls and cells. One reason for this is because the martensite in these steels is a low carbon martensite that can not only act as obstacles against dislocation movement giving rise to initial hardening, but also can deform plastically later giving rise to softening. Sarosiek and Owen [104] have also reported that dual phase steels with a martensite matrix showed softening due to the same phenomenon. Strain partitioning between the ferrite and the martensite phases is an important consideration in these steels [105]. The strain heterogeneity in areas that contain ferrite constrained by martensite is much higher than the other areas.

2.2.3 *Persistent Slip Bands (PSBs)*

Since about a century it has been known that cyclic loading of metals leads to the formation of bands of concentrated slip. They were first observed in 1903 by Ewing and Humfrey [17] in Swedish iron using a metallurgical microscope as shown in Figure 2.2. These bands are regions of cyclic slip localization and are often visible both on the surface and deep within a material on sectioning and subsequent etching [106]. Mughrabi [107], Lukas and Kunz [13] and more recently Antolovich and Armstrong [108] have reviewed various aspects of their formation and associated phenomena in great detail. Some salient features are described below.

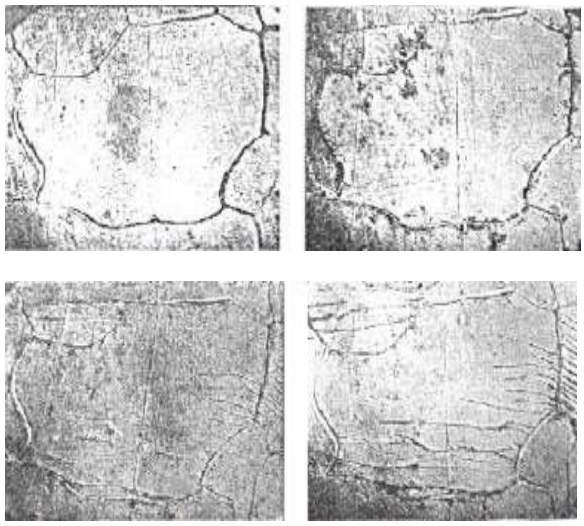

Figure 2.2: Slip band evolution in "Swedish Iron" fatigued at a stress amplitude of approximately 196 MPa at (a) 1,000 cycles; (b) 2,000 cycles; (c) 10,000 cycles and (d) 170,000 cycles [17].

A) Formation of PSBs: During fatigue of a material, the dislocation behavior may differ in the tension and the compression portions of the cycle. Any dislocation that emerges onto the surface in the forward cycle and does not return back leads to the formation of a slip step [107] in a particular crystallographic direction. Accumulation of such slip steps over a number of cycles leads to the surface roughening of the material with sites of local stress concentration that may lead to crack initiation. This phenomenon is termed as "cyclic slip irreversibility (CSI)". In BCC materials, the mechanism of strain accommodation during CSI may manifest itself either by slip plane asymmetry or by the formation of slip bands. While slip plane asymmetry is more common for pure BCC materials, the formation of slip bands are more common in commercial alloys of BCC materials such as steels.

As has been discussed in section 2.2-B, addition of impurities, especially interstitial carbon, leads to a preferential decrease in the mobility of the edge dislocations in a BCC structure. This causes the mobilities of the edge and the

screw dislocations to become comparable, even at room temperature. On application of cyclic loading, dislocation rearrangements occur. The screw dislocations cross slip and annihilate each other while the remaining edge dislocations arrange themselves in clusters of elongated dipolar loops, which can be of vacancy or interstitial type. The loops often get further chopped by cross slip into shorter loop segments. The elongated dipole loops then cluster together to form di-/multipolar veins [109]. On further cyclic loading, at some stage the work-hardened dislocation distribution can no longer accommodate the imposed plastic strain. At this stage, the vein structure often breaks down locally giving way to the softer, newly formed lamellae of the **Persistent Slip Band** ladder-like structure [107] of the kind shown in Figure 2.3. At high values of plastic strain amplitudes, the microstructure is transformed yet again resulting in bulk cyclic hardening with increasing participation of the screw dislocations, dislocation multiplications, and dislocation cell formation. Thompson et al. [1] have showed that even when the surface traces of these bands were polished away, they would reappear at the same location upon further cyclic loading, hence the term "persistent". These PSBs are the main focus of this study.

The extent of PSB formation in polycrystals is less than in single crystals fatigued at the same strain amplitude. This can be attributed to the mutual constraints due to the neighboring grains [13]. The effect of grain size was further evident in ultrafine grained copper where the PSB formation was found to be completely absent [110]. These constraint effects are also responsible for the PSBs in polycrystals having higher density on surface grains (lower constraints)

than in the interior grains (higher constraints) [111].

It has been reported that in materials with a planar slip character, such as Cu-Zn and Cu-Al alloys with sufficiently high zinc or aluminum content, PSBs do not form [112]. In such cases, the dislocation structure consists of planar arrays of edge dislocations on the activated slip systems. Within these arrays are denser and less dense slabs leading to inhomogeneity of cyclic slip. Such slabs are known as Persistent Ludar Bands (PLBs)[113]. Contrary to PSBs, PLBs are not permanent and do not represent zones of dislocation structure different from the surrounding matrix. However, they may still lead to surface slip markings where microcracks may initiate [13].

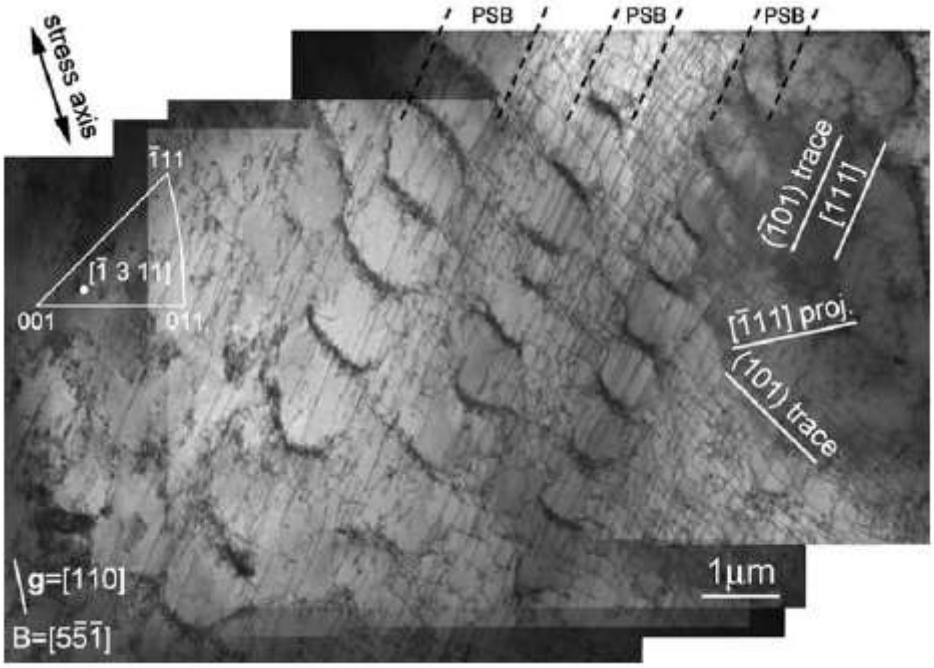

Figure 2.3: Characteristic ladder structure of PSBs as revealed by TEM in ferritic steel cycled at plastic strain amplitude of 0.002 for 9000 cycles [31].

B) Characteristics of PSB structure: These bands are generally formed along the primary slip direction which is also the direction having the maximum value of

critical resolved shear stress [22] (as cited in [107]). The fully developed PSBs are often upto 2 μm in height [8]. They can extend across an entire single crystal and across grains in polycrystalline materials [52]. The formation of PSB's divides the microstructure into two parts, the dislocation rich regions of the slip bands where the cyclic slip is localized and the dislocation poor matrix that surrounds the PSB's. An instance of PSBs formed in the softer ferrite phase along with the surrounding matrix in a ferrite-austenite duplex steel is shown in Figure 2.4.

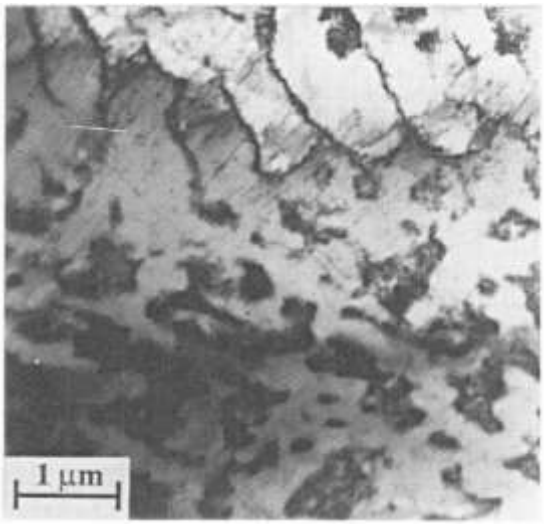

Figure 2.4: TEM micrograph of a duplex steel showing the boundary between the matrix (lower part of the image) and area of slip localization – PSBs (upper part of the image) in a ferrite grain [114].

The PSBs appear on the free surface in the form of surface hill-and-valley like features. The 'hills' are called extrusions while the 'valleys' are called intrusions. Together, the extrusions and the intrusions lead to the roughening of the surface, especially as the cumulative strains increase, either because of the increase in the number of cycles and/or because of an increase in the load/strain amplitudes. The combination of extrusions and

intrusions on the surface is often referred as Persistent Slip Markings (PSMs). A schematic of a classic well-developed PSB-PSM structure is shown in Figure 2.5.

C) Role of PSBs in crack initiation: The strain applied during cyclic loading is almost completely concentrated within the slip bands. The interface between the PSB and the matrix is a plane of discontinuity across which there are abrupt strain gradients, resulting in a preferred site for crack initiation as shown in the case of single crystal copper in Figure 2.6. PSBs can play a part in crack initiation in mainly three ways [13].

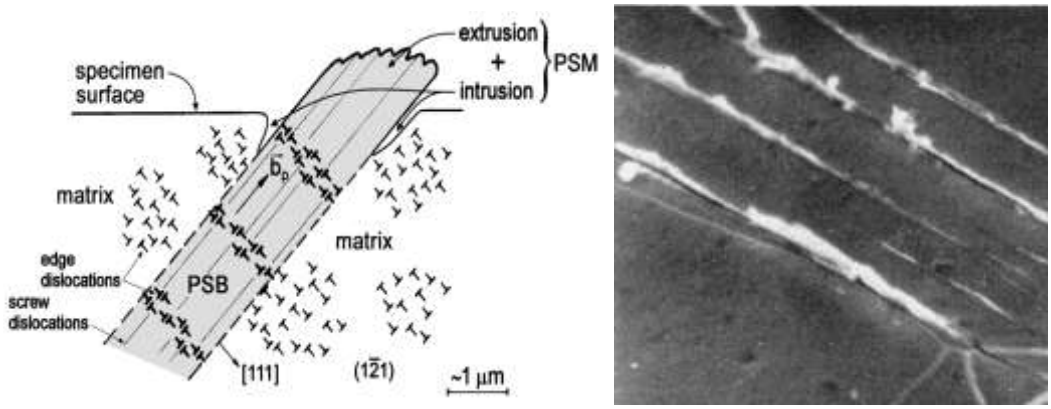

a) b)

Figure 2.5: a) A mature fully grown PSM observable at the site where a PSB intersects the free surface [115]; b) Intrusions and extrusions as seen in ferritic steel at 5000X [73].

1. Initiation at the PSB: With increased accumulated plastic strain, the PSBs themselves can become a site for crack initiation.
2. Initiation at grain and twin boundaries: The cracks can often initiate at the large-angle grain boundaries at sites where the PSBs impinge on them [116].

3. Initiation at inclusions, pores and other inhomogeneities: PSBs can also interact with the inhomogeneities within the microstructure and these interaction locations can become crack initiation sites.

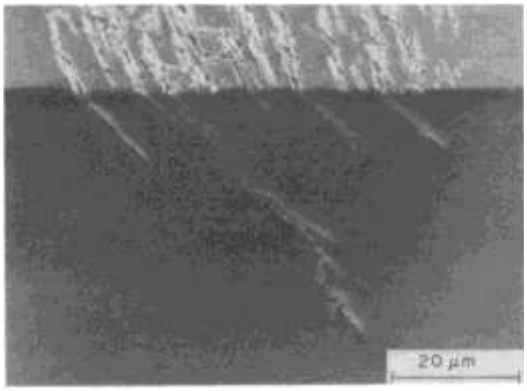

Figure 2.6: A 90^0 section through a single PSB after, (1) overstraining at γ_{pl} = 0.2% for 10^4 cycles, 2) electropolishing, (3) cycling with a reduced local plastic strain amplitude (γ_{pl} = 0.3%) for 2 x 10^6 cycles at 20Hz at γ_{pl} = 0.02% [117].

The tendency to form intragranular cracks due to slip bands increases in a material at a) lower plastic strain amplitudes, b) lower strain rates and c) lower grain sizes as well as increasing temperature and impurity content [31]. In dual phase steels, the surface markings that are associated with the formation of the PSB's were found to be more intensive for the ferrite grains. Very little is known about the exact mechanism in operation. The harder martensite phase is believed to act like a microstructural barrier to the propagation of the slip bands and the cracks, especially at the low to medium strain amplitudes. It has been reported that an increase of the martensite content promotes the crack initiation along the slip bands formed near the ferrite-martensite interfaces [56]. This is explained by the fact that an increase in the martensite content leads to a lowering of martensite hardness. This allows better strain compatibility between ferrite and the softer martensite. In a simplistic argument, this compatibility leads to lower strain localization at the interface and a more homogeneous distribution of dislocations in the

grain interior. Thus, the authors conclude that interface cracking is suppressed and cracking at the PSB becomes dominant.

2.2.4 *Experimental techniques to study PSBs*

Several experimental techniques have been used over the years to study the qualitative and quantitative behavior of the PSBs and/or PSMs. The earliest works used different forms of optical microscopy in order to study the surface relief that occurred as a result of fatigue [17, 118] or to understand the 3-D form of the initiated crack itself [119]. The use of plastic replicas for all kinds of surface characterizations was also fairly common. However very often, the scope of these studies was severely limited by low lateral resolution. Moreover, these studies were also hampered by the presence of inherent artifacts that made it difficult to make deductions from the observations.

Transmission electron microscopy has been a very useful tool in making qualitative assessments on the PSB structures as well the inherent dislocation substructure of cyclically loaded materials. Carbon shadowing as well as two–stage carbon replica processes [19] have often been used together with this technique. However experimental difficulties such as the difficulty in preparing metal foils for the surface observations along with the problems in the accurate interpretation of the observations makes this technique rather difficult to use for quantitative studies.

Scanning electron microscopy has been extensively used in the study of PSBs. This is because of a) the relative ease of use and b) its ability to provide high-resolution images at high magnifications. These benefits make SEM techniques ideal for making surface observations on fatigued materials. SEM techniques have often been used for

qualitative study of the PSB/PSM topography [67] or for characterization of extrusion profiles for single crystal FCC and BCC materials [16]. In fact, the use of SEM coupled with Focused Ion Beam (FIB) techniques has made it possible to study the subsurface structure of PSBs as well [120]. However, some of the limitations of these techniques have been the lack of their ability to study the dislocation substructure and the inability to study the intrusion profiles.

.

2.2.5 *Quantitative analysis of damage evolution*

Quantification of early fatigue damage in materials has been attempted using several different parameters of PSBs. While some studies have concentrated on the phenomenon of strain localization and its variation as a function of strain amplitude and number of cyclic reversals, others have characterized aspects of PSBs such as their width, height or orientations. A brief summary of these works is attempted in this section.

One way to characterize the damage during cyclic loading is to consider the extent of irreversibility in the slip. As mentioned earlier, this irreversibility of slip manifests itself in the form of slip steps on the surface. However, these slip steps are as much a result of surface behavior as they are of what changes the bulk of the material goes through. Essmann [121] and Mughrabi et al. [122] have quantified cyclic slip irreversibility, p as the fraction of plastic shear deformation that is irreversible as shown in Equation 2.1:

$$p = \frac{Irreversible\ plastic\ shear\ strain}{Cumulative\ total\ plastic\ shear\ strain} \tag{2.1}$$

This cyclic slip irreversibility, p will depend on the plastic shear strain amplitude, γ_{pl}. This irreversible part of the plastic shear strain amplitude (= p x γ_{pl}) *is* what is responsible

for the irreversible changes that occur in the microstructure. Thus the cumulative plastic shear strain after N cycles can be written as:

$$\gamma_{pl} = 4 \text{ N x } p \text{ x } \gamma_{pl} \tag{2.2}$$

In general, it is not easy to quantitatively determine this *bulk* cyclic irreversibility for materials. Therefore, till now, these values have been estimated for only a few materials. Nonetheless, this method provides a way to quantify the number of cycles to the bulk irreversibility caused due to cyclic loading.

In terms of quantifying the attributes of the slip bands themselves, one way is to look at the 2-D length of the extrusions as a function of the number of cycles. Baxter and McKinney [123] made such a study on polycrystalline 6061-T6 aluminum and compared the behavior in two samples having distinctly different grain sizes. They reported that in the two materials, 2-D growth ($\frac{dl}{dN}$), where l = 2-D length of an individual slip band varied with the number of cycles, N in the following manner:

For small grained sample:

$$\frac{dl}{dN} \propto (N - N_0)^{1/2} \tag{2.3}$$

While for large grained sample:

$$\frac{dl}{dN} = const. \tag{2.4}$$

This behavior is explained by the combined effects for the incremental increase in the damage per cycle of the loading and the effect of the grain boundary. For a large grained material, the latter has only a limited effect in the development of a slip band. Thus the change in length is linear with number of cycles. However, in case of a small-grained material, the “back-stresses” due to the grain boundaries can hinder the free movement of

dislocations thus retarding the growth of the slip bands. This was also the reason why the growth rates of the bands in the smaller grains were found to be an order of magnitude less than in the large grains.

As mentioned earlier, several studies on single crystals have been conducted to understand the behavior of slip bands. One such study by Sestak et. al. [124] on single crystals of Fe-13.6 wt.% Cr observed the average surface fraction occupied by PSBs over the entire gage length. This was plotted as a function of $\Delta\varepsilon_{pl}$ and is shown in Figure 2.7. It was observed that the slip bands grew linearly initially and covered the entire surface within a few cycles. Since $\Delta\varepsilon_{pl}$ is directly proportional to N, one can notice that the behavior for single crystals is similar to the one shown by the polycrystalline material with large grain sizes in Equation 2.4.

Man et al [31] studied fatigue of ferritic X10CrAl24 stainless steels with average grain size ~ 38μm and performed measurements on the extrusion heights throughout the life. They found that the growth rate per cycle was high for the initial part of life ($0.1N_f$). It decreased later but did not drop to zero. This study was conducted using AFM and over certain selected extrusions over a number of cycles.

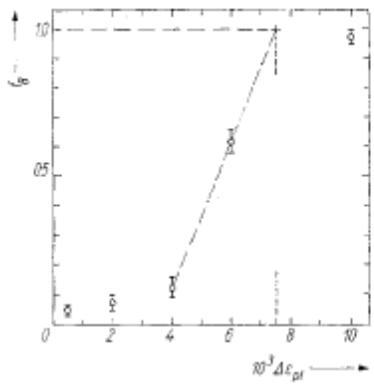

Figure 2.7: Plot of surface fraction, f_B of persistent slip bands as a function of $\Delta\varepsilon_{pl}$; $\dot{\varepsilon} = 1.7 \times 10^{-2}$ [124].

Yet another characteristic of PSBs that has been analyzed quantitatively is their angular orientation in a polycrystalline material. Polak et al [125] as well as Girones et al [126] have made 2-D angular measurements on the angle made by the PSBs. Both studies found that the angle with respect to the loading axis was in the range of 25^0-90^0 with the peak at 45^0. Similar study has been conducted in the present work along with an analysis of the 3-D angular distribution of the PSBs with respect to the loading axis. The results as well as possible explanations are also presented later.

Thus, it can be seen that while a lot of work has been conducted in understanding the qualitative and phenomenological aspects of PSB related damage evolution, comparatively limited quantitative literature is available for PSB evolution especially with regard to their properties such as orientation, distance between the PSBs etc. These limitations along with the experimental difficulties often restricted the studies to analyzing only FCC single crystals. Almost all studies are quite *localized* in nature. Studies on the angular orientation of the PSBs analyze the behavior in 2-D that gives an incomplete picture of the true (3-D) orientations. However, it is felt that with the availability of highly advanced equipment, many of the limitations of the traditional microscopy techniques have been either eliminated or their effect minimized. Hence it is now possible to carry out systematic studies on the surface of more complicated materials (*for example* BCC polycrystals). Also, to the best of the author's knowledge, there has been a very limited application of quantitative stereology to the study of the PSBs. However, stereology can be a very useful tool, especially for making statistical 3-D estimates from 2-D observations. Therefore, using some of these experimental techniques and stereological calculations (as described in the next section), this study provides new

insights into the understanding of the formation, nature and evolution of the PSBs as a function of strain amplitudes and/or number of cycles.

2.3 Stereological Techniques

Stereological techniques involve sampling of three-dimensional (3-D) microstructure by lower dimensional geometric probes such as test planes, test lines or points. The required quantitative metallographic measurements are performed on a systematic uniform random (or independent random) statistical sample of a large number of fields of view in representative two-dimensional (2-D) section(s). The 3-D microstructural attributes are then estimated from such 2-D measurements using *unbiased*[1], unambiguous, and assumption-free stereological equations. The stereological techniques used in the experimental part of this research are presented in the following sub-sections.

2.3.1 *Volume fraction estimation*

The volume fraction of a microstructural constituent or phase, V_V, is the fraction of the reference 3-D microstructural space occupied by that constituent/phase, and therefore, it is a quantitative measure of the relative amount of that microstructural constituent/phase in the microstructure. Numerous material properties depend on volume fractions of the constituent/phases present in the microstructure [5, 51, 53, 127-130]. Volume can be estimated from the measurements performed in representative 2-D metallographic sections without involving any assumptions concerning the shapes, sizes

[1] In this context, the term *unbiased* implies that as the number of 2-D measurements approach infinity, the estimated 3-D microstructural attribute approaches its exact value in the 3-D microstructure.

orientations, or spatial randomness of the features of interest. Moreover, it is not necessary to know the microscope/image magnification for estimation of volume fraction because it is dimensionless. The following stereological techniques can be used for estimation of volume fraction.

2.3.1.1 Areal analysis

Areal analysis involves measurements of the area fraction of the phase/constituent of interest in representative 2-D metallographic sections/planes [131]. The *average* value (or more precisely, statistical expected value,) $\langle A_A \rangle$ of the area fraction A_A is equal to the volume fraction V_V of that phase/constituent in the 3-D microstructure.

$$V_V = \langle A_A \rangle \tag{2.5}$$

Theoretical basis of the areal analysis and other details are described elsewhere [132, 133]. Areal analysis is a convenient and efficient method for estimation of volume fraction if automated digital image analysis can be used. In such a case, the area fraction of the constituent/phase of interest is simply equal to the number of pixels of binary microstructural image in the constituent/phase of interest divided by the total number of pixels in the binary image frame. The average value of this parameter is then related to the volume fraction via Equation 2.5. In some microstructures appropriate image segmentation to generate reliable binary images is not possible. In such microstructures, the area fraction measurements have to be performed manually, which is tedious and inefficient [134]. When manual measurements have to be performed, the point counting method of volume fraction estimation described below is efficient and useful in practice.

2.3.1.2 Point counting

In the point counting technique, test points are used to probe the 3-D microstructure. A set of test points are placed at random locations in the microstructure and the test points contained in the constituent/phase of interest are counted. The fraction of test points in the constituent/phase of interest P_P is calculated. In general, P_P is a random variable whose value varies from one measurement frame to another. Nonetheless, it can be mathematically shown that the population average value or expected value $\langle P_P \rangle$ of P_P is an unbiased estimator of the volume fraction of the corresponding constituent/phase in the 3-D microstructure [131-133, 135, 136].

$$V_V = \langle P_P \rangle \tag{2.6}$$

Point counting can be performed be using a grid containing periodic array of test points (*systematic point counting)* or by using randomly distributed test points (*random point counting*). The two methods have been illustrated in Figure 2.8 (a) and (b). Systematic uniform random point counting involves placement of the test point grid at uniformly spaced locations in the metallographic plane once the first grid placement is chosen at random. On the other hand, independent random point counting involves placing a set of random test points in randomly chosen microstructural fields in the metallographic plane(s). Both systematic uniform random point counting and independent random point counting constitute *unbiased sampling*[1] of microstructure and Equation 2.6 is equally applicable to both of these sampling procedures. However, it can be shown that systematic uniform random point counting is significantly more *efficient*[2] as compared to

[1] In this context, unbiased sampling implies that when such statistical sampling design is used, the measured average approaches the true population average of the corresponding parameter in the 2-D section, as the number of measurements approaches infinity.
[2] It leads to lower random sampling error for the same measurement effort.

the independent random point counting; as well as systematic uniform random sampling is more efficient than independent random sampling [131, 133, 137-143].

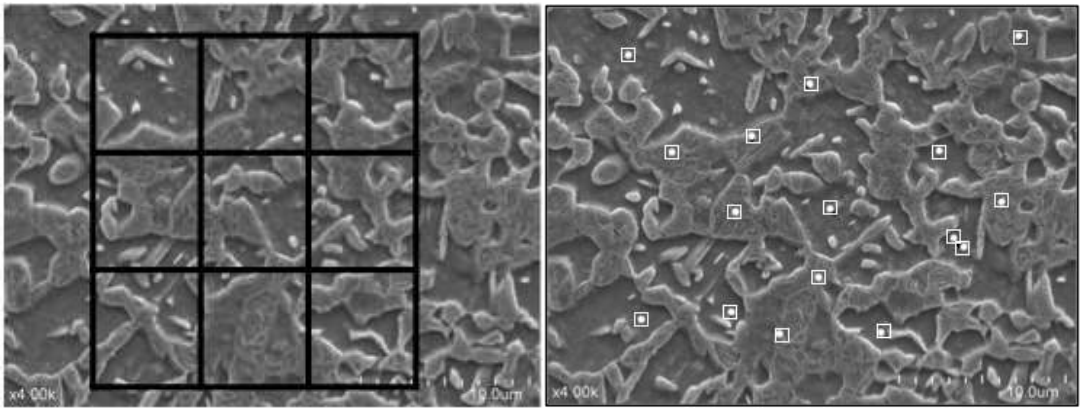

(a) (b)

Figure 2.8: (a) A systematic grid of 16 points and (b) A set of 16 randomly distributed test points. Both sets of points overlaid on a microstructure of DP 980 steel to estimate the volume fraction of martensite using point counting method.

2.3.2 *Total surface area per unit volume (S_V)*

Microstructures often contain internal surfaces or boundaries such as grain boundaries, precipitate-matrix interfaces, surface of internal voids/cavities, and so forth. S_V represents the total area of the surfaces of interest per unit volume of the microstructure. S_V can be used to characterize how fine (or coarse) the microstructure is. The dimensions of S_V are $\mu m^2/ \mu m^3$. Since it is not dimensionless, it is important to know the magnification of the micrographs for its estimation.

The stereological estimation of the total surface area of the grain boundaries or any other type of internal surfaces can be made using the line intersection counting method. In this method, the test probe is a line. The intersections of the features of interest with the test line are measured (P). The number of intersections per unit test line length is calculated then ($P_{L)}$ is related to the total surface area S_V by the following relationship [136, 144]:

$$S_V = 2 <P_L> \quad (2.7)$$

where $<P_L>$ denotes the average value of the number of intersections per unit test line length. For a microstructure having randomly oriented and uniformly distributed internal grain boundaries/interfaces of interest, S_V can be estimated from measurements performed in a single representative metallographic plane. Equation 2.7 is applicable to anisotropic microstructures as well, provided the intersection counts are performed on metallographic planes of many different orientations and $<P_L>$ is an average of such measurements. Such measurement is tedious and time consuming. For anisotropic microstructures, estimation of S_V is significantly more efficient and precise when the measurements are performed using vertical section sampling design and cycloid shape test lines [145, 146].

An alternate stereological method for estimation of S_V involves measurement of the total perimeter of the microstructural boundaries/interfaces of interest per unit area of metallographic plane, L_A utilizing the following equation [136, 144]:

$$S_V = (4/\pi)<L_A> \quad (2.8)$$

In Equation 2.8, $<L_A>$ is the average value of L_A obtained by averaging it over the planes of all possible orientations in the 3-D space. If microstructural boundaries/interfaces of interest have uniform random orientations (such as those in isotropic microstructures), L_A does not vary systematically with the angular orientation of metallographic plane, and therefore, measurements of L_A on plane(s) of a single angular orientation yield precise estimate of the average $<L_A>$ [134].

For anisotropic microstructures, application of Equation 2.8 requires measurements of L_A on metallographic planes of many different angular orientations in

the 3-D space, which is tedious and time consuming, and highly inefficient. Gokhale and Underwood [147] proposed a stereological method for efficient estimation of fracture surface roughness that is equally applicable for efficient estimation of L_V in anisotropic microstructures. The technique involves measurements on vertical metallographic planes and it requires measurement of length weighted orientation distribution *f(α)* of the line elements of the boundaries/interfaces and total perimeter length per unit area L_A in the vertical metallographic planes. Gokhale and Underwood's equation can be cast into the following form for estimation of S_V.

$$S_V = < \psi \, L_A > \tag{2.9}$$

In Equation 2.9, ψ is the structure factor given by the following equation.

$$\psi(\phi_p) = \int_0^{\pi} \left[\sin\alpha + \left(\pi/2 - \alpha\right)\cos\alpha\right] f(\alpha, \phi_p) \cdot d\alpha \tag{2.10}$$

In Equation 2.10, ϕ_p is the orientation angle of the vertical sectioning plane and α is the angle between an infinitesimal line element of boundary/interface of interest observed in a vertical metallographic plane and the chosen vertical axis (see Figure 2.9). It can be shown that measurements on vertical metallographic planes of more than three different angular orientations are never required for estimation of S_V using Equations 2.9 and 2.10 [146]. If the microstructural anisotropy has an axis of symmetry and that direction is chosen as the vertical axis, then measurements of L_A and *f(α)* on just one vertical plane are sufficient.

In Chapter 4, these basic stereological parameters as well as some derived parameters calculated using these basic parameters are utilized for quantification of microstructure and microstructural damage due to formation and growth of PSBs. The

next Chapter presents development of some new stereological techniques particularly suited for quantitative characterization of the PSBs.

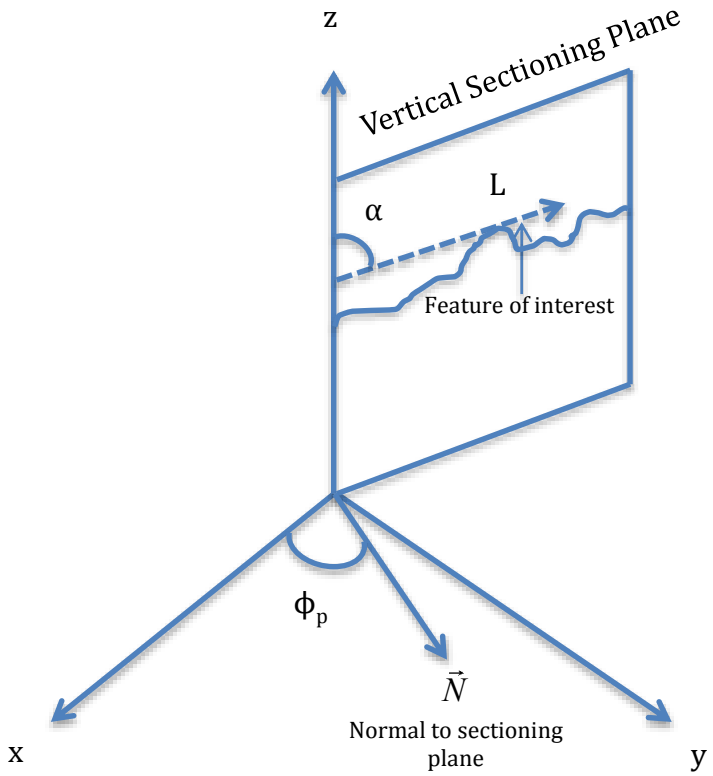

Figure 2.9: Geometry involved in calculation of S_V using 2-D orientation and length of a feature (adapted from [147]).

Chapter 3

Theoretical development

The stereological techniques for estimation of volume fraction and total surface area per unit volume have been presented in the previous chapter. In the present research, these well-known stereological methods are applied for estimation of volume fraction and total surface area of the PSB colonies. In this Chapter, new stereological techniques are developed for estimation of 3-D angular orientation distribution of PSBs and average spacing between the PSBs in 3-D microstructure from the measurements performed on the persistent slip markings (PSMs) and their colonies in the 2-D fatigue specimen surfaces. Practical applications of these theoretical results are described in detail in the next chapter for quantitative characterization of the evolution of 3-D angular orientation distribution of PSBs and average spacing between PSBs as a function of number of fatigue cycles, strain amplitude, and AHSS steel microstructure. The next section of this chapter presents the derivation of the stereological relationship between 2-D angular orientation distribution of the PSMs that can be experimentally measured in the fatigued specimen surfaces and the corresponding 3-D angular orientation distribution of the PSBs. Stereological relationship for estimation of the 3-D average distance between the PSBs in the PSB colonies is derived in the subsequent section.

3.1 3-D Angular distributions from 2-D angular measurements

Most studies on PSBs are restricted to single crystals. Within a crystal, the orientation of all the PSBs is more-or-less the same. However, for a polycrystal, an orientation distribution of the PSBs across the different grains is expected. To the best of the author's knowledge, this orientation distribution in 3-D has never been quantitatively analyzed. However, using stereology, simple 2-D measurements of the orientations of the extrusion colonies can be used to predict the statistical 3-D angular orientation distributions of the PSBs. This technique is described as under:

Choose XYZ reference coordinate system such that the Z-axis is parallel to the loading direction of the fatigued specimen. Let YZ plane be the observation plane in the fatigued specimen surface in which the slip markings are observed and characterized. In general, this can be any plane parallel to the loading direction. X-axis is then the direction perpendicular to the observation plane. In the present context, a band is a volume between two parallel planar segments (slip planes) of finite extent separated by a small distance t, where there is intense localized slip. The angular orientation of a band is specified by the orientation of the normal to its faces given by the two spherical polar angles θ and Φ, where θ is the angle between the normal and Z-axis (loading direction) and Φ is the angle between the projection of the normal on the XY plane and the X-axis (*ref.* Figure 3.1).

The orientation distribution of the bands with respect to the loading axis (i.e., distribution of the angles θ) is of primary interest. Under uniaxial cyclic loading, polycrystalline metals having equiaxed grains and no preferred crystallographic texture, the band orientations are expected to be symmetric with respect to the loading direction

(Z-axis), i.e., in an ensemble of bands, all Φ values are equally likely, and consequently, the orientation distribution of the bands does not depend on Φ. Accordingly, it is assumed that the orientation distribution of the bands is independent of Φ, and therefore, it is a function of a single variable θ. As the z-axis is a symmetry axis, it is sufficient to consider the angle ranges $0 \leq \theta \leq 90$ degrees and $0 \leq \Phi \leq 90$ degrees.

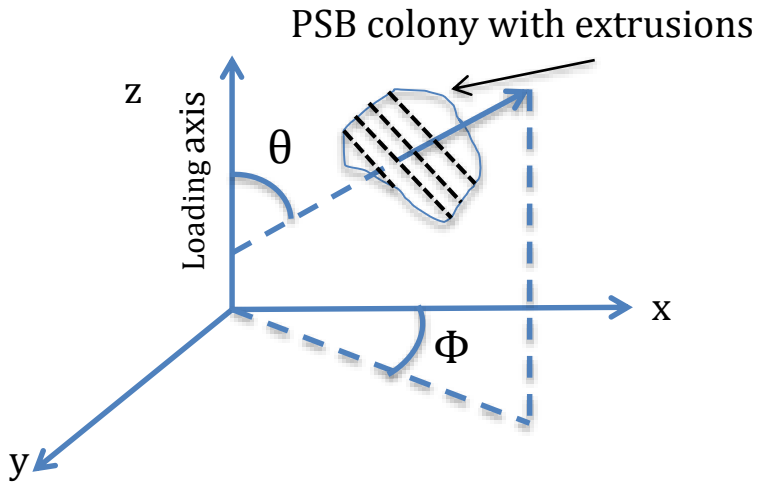

Figure 3.1: Image displaying the angular orientations used in the calculation of the 3-D angular distribution of the PSB.

To develop a simple practical numerical solution to the problem, it is further assumed that slip bands are present only at discrete orientation angles θ. As θ approaches 0 or 90 degrees, the Schmidt factor for the corresponding slip planes approaches zero. Therefore, bands of orientations very close to θ equal 0 and 90 degrees are very unlikely to occur. Consequently, θ orientation angles are discretized to have values 10, 20, …., 80 degrees that are at intervals of 10 degrees. Thus, θ admits discrete values $\theta_j = j\Delta$ degrees, where $j = 1, 2, \ldots, 8$, where Δ is the class interval, which is equal to 10 degrees. Let G_j be the angular orientation distribution function of the bands such that $2G_j d\Phi/\pi$ is the fraction of the surfaces area of the ensemble of bands having $\theta = \theta_j$ and Φ orientation

angle in the range of Φ to (Φ +d Φ). Thus, θ takes only discrete values θ_j in the range $10 \leq \theta_j \leq 80$ degrees but Φ is a continuous variable that takes all values in the range $0 \leq \Phi \leq 90$ degrees with equal probability. Let dS (θ_j, Φ) be the total surface area of faces of the bands having the orientation angle $\theta = \theta_j$ and Φ angle in the range Φ to (Φ +d Φ) per unit volume of the specimen and let S_0 be the total surface area of the bands of all orientations per unit volume of specimen. Therefore,

$$dS(\theta_j, \Phi) = 2S_0 G_j d\Phi/\pi \quad (3.1)$$

Slip markings in the YZ observation plane of the fatigued specimen can be regarded as the traces (lines of intersections) of the bands with the YZ plane. Figure 3.2 illustrates such slip markings in a fatigued specimen. Note that slip markings appear in colonies such that slip markings in different colonies may have different angular orientations. Let α be the acute angle ($0 \leq \alpha \leq 90$ degrees) between slip marking and the loading direction.

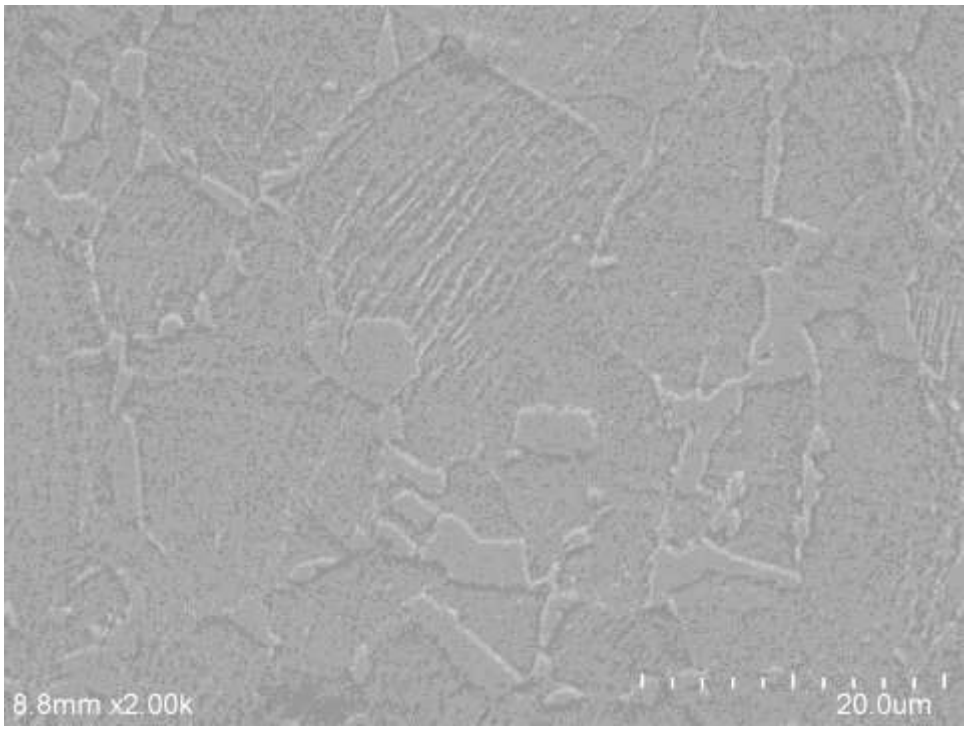

Figure 3.2: A figure showing slip markings within a slip colony in DP590 steel fatigued at 1% strain amplitude for 25 cycles. The horizontal direction represents the loading axis.

Let F(α) be the orientation distribution of the slip markings such that the fraction of the slip marking length in the orientation range α to (α+dα) is equal to F(α)dα. Let dB (α) be the total length of the slip markings in the orientation range α to (α +dα) per unit area of the observation plane and let B_0 be the total length of slip markings of all orientations per unit area of the observation plane. Therefore,

$$dB(\alpha) = B_0 F(\alpha) d\alpha \tag{3.2}$$

The normal to the YZ observation plane is at angle of 90 degrees with Z-axis and at angle of 0 degrees with X axis. For this orientation of the observation plane, the relationship between orientation of a band face (θ_j, Φ) and orientation α of its trace (slip marking) in the YZ plane is given as follows [146, 148].

$$\text{Cot}\alpha \, \text{Cot}\theta_j = - \text{Sin}\Phi \tag{3.3}$$

Therefore, a slip of marking of orientation range α to (α+dα) can originate from slip bands of different orientation angles θ_j and Φ that satisfy Equation 3.2.

Let dB (α, θ_j, Φ) be the length of slip markings in the orientation range α to (α +dα) per unit area of the observation plane originating ONLY from slip bands having the orientation angle $\theta = \theta_j$ and all Φ values that yield α in the range α to (α+dα) as dictated by equation 3.2. Let dP_L (α, θ_j, Φ) be the expected value of the number of intersections between the slip markings in the orientation range α to (α+dα) present in the observation plane originating only from slip bands of orientation $\theta = \theta_j$ and all Φ values that yield α in the range α to (α+dα) as dictated by Equation 3.3 and test lines placed parallel to the loading direction (Z-axis) in the observation plane per unit test line length. Stereology gives the following general relationship.

$$dP_L(\alpha, \theta_j, \Phi) = [\text{Sin}\alpha] \, dB(\alpha, \theta_j, \Phi) \tag{3.4}$$

Now consider a thought experiment, where a large number of straight test lines parallel to the loading direction (Z-axis) are placed in the 3D structure. The expected number of intersections of such test lines with band faces of orientation $\theta = \theta_j$ and all Φ values that yield α in the range α to $(\alpha+d\alpha)$ as dictated by Equation 3.3, i.e., $dP_L(\alpha, \theta_j, \Phi)$ is also alternately given by the following general stereological relationship [12, 13].

$$dP_L(\alpha, \theta_j, \Phi) = S_0 G_j \tag{3.5}$$

In Equation 3.5, the orientation range $d\Phi$ is such that corresponding slip markings have orientation in the range α to $(\alpha+d\alpha)$. Combining Equations 3.4 and 3.5 yields the following key result.

$$dB(\alpha, \theta_j) = 2\{\text{Cos}\,\theta_j/\text{Sin}\alpha\}\, S_0 G_j\, d\Phi/\pi \tag{3.6}$$

Equation 3.4 pertains to a specific value of $\theta = \theta_j$ and all Φ values that yield α in the range α to $(\alpha+d\alpha)$ and satisfy Equation 3.3. Therefore, it can be also written in the following alternate form.

$$dB(\alpha, \theta_j) = 2\{\text{Cos}\,\theta_j/\text{Sin}\alpha\}\, S_0 G_j\, (\partial\Phi/\partial\alpha)_{\theta j}\, d\alpha/\pi \tag{3.7}$$

Partial differentiation of Equation 3.3 with respect to α at constant θ_j yields the following result.

$$(\partial\Phi/\partial\alpha)_{\theta j} = \{\text{Cot}\,\theta_j/\text{Sin}^2\alpha\}\, \{1 - \text{Cot}^2\theta_j\, \text{Cot}^2\alpha\}^{-1/2} \tag{3.8}$$

Combining Equations 3.5 and 3.6 leads to the following result.

$$dB(\alpha, \theta_j) = \{2S_0/\pi\}\, \{\text{Cos}\,\theta_j/\text{Sin}\alpha\}^2\, \{\text{Sin}^2\alpha - \text{Cos}^2\theta_j\}^{-1/2}\, G_j\, d\alpha \tag{3.9}$$

Or,

$$dB(\alpha, \theta_j) = 2\{[\text{Cos}\,\theta_j/\text{Sin}\alpha]^2\, [\text{Sin}^2\alpha - \text{Cos}^2\theta_j]^{-1/2}\, d\alpha/\pi\} S_j \tag{3.10}$$

In Equation 3.10, S_j is the total surface area of the bands having orientation angle $\theta = \theta_j$ and <u>all</u> possible values of Φ in the range 0 to 90 degrees. To calculate S_j

numerically, the measured slip marking angles α are divided into 8 class intervals. As θ_j is in the range of 10 degrees to 80 degrees, Equation 3.3 dictates that the minimum possible value of α is 10 degrees. Consequently, α is in the range $10 \leq \alpha \leq 90$ degrees. Let B [i, j] be the total length of the slip marking per unit area of the observation plane having the orientation angles α in the range $i\Delta \leq \alpha < (i+1)\Delta$ originating ONLY from the bands having orientation angle $\theta = \theta_j$, where i = 1, 2,…..8 and Δ = 10 degrees. Integration of Equation 3.10 yields the following result.

$$B [i, j] = b [i, j] S_j \tag{3.11}$$

Where, S_j is the total surface area of all band faces per unit volume having $\theta = \theta_j$ and all values of Φ in the range of 0 to 90 degrees. The coefficients b [i, j] are given as follows.

$$b [i, j] = (2/\pi) \int_{i\Delta}^{(i+1)\Delta} [\text{Cos}\,\theta_j/\text{Sin}\alpha]^2 [\text{Sin}^2\alpha - \text{Cos}^2\theta_j]^{-1/2}\, d\alpha \tag{3.12}$$

where, i = 1, 2,…..8, for each i, j = [8-(i-1)], [8-(i-2)], …. 8, $\theta_j = j\Delta$ degrees, and Δ is equal to 10 degrees. The coefficients b [i, j] can be calculated via numerical integration of the integral in the right hand side of Equations 3.9. The computed values of the coefficients are given in Table 3.1, which can be used for calculation of S_j pertaining to any microstructure using the unfolding procedure given below.

Table 3.1: Coefficients b[i, j] as computed from Equation 3.12

	j = 1	j = 2	j = 3	j = 4	j = 5	j = 6	j = 7	j = 8
i = 1								0.56146776
i = 2							0.503643585	0.053182245
i = 3						0.476875651	0.090412907	0.019350612
i = 4					0.474248697	0.115262282	0.043004383	0.009973734
i = 5				0.495600824	0.138566409	0.06484267	0.026361483	0.006310441
i = 6			0.54947931	0.167626281	0.088525133	0.045141793	0.019001373	0.004619145
i = 7		0.665918183	0.212728297	0.119888106	0.068709074	0.036231209	0.015502014	0.003798101
i = 8	0.992418441	0.304162549	0.172007883	0.10378542	0.061082696	0.032628619	0.014055638	0.003455354

Let B_i be the total measured length of slip markings per unit area of the observation plane having measured orientation angles in the range $i\Delta \leq \alpha < (i+1)\Delta$ originating from all θ_j and Φ orientation angles of the bands that satisfy Equation 3.3. Therefore,

$$B_i = \sum_{j=9-i}^{j=8} b\,[i, j]\, S_j \qquad (3.13)$$

where, i = 1,2,3,…….,8. We now have 8 independent simultaneous linear equations, one for each value of i. B_i are the measured experimental data. Consequently, one can solve these equation to compute unknown quantities S_j because the coefficients b [i, j] are known (see Table 3.1). The solution is as follows.

$$S_8 = B_1 / b\,[1, 8] \qquad (3.14)$$

and,

$$S_j = \{B_{9-j} - \sum_{m=j+1}^{m=8} b\,[(9-j), m]\, S_m\} / b\,[(9-j), j] \qquad (3.15)$$

where, j = 7, 6, 5, ……1.

Equations 3.11 and 3.12 can be transformed into the following form that simplifies calculations.

$$S_j = \sum_{i=1}^{i=9-j} a\,[i, j]\, B_i \qquad (3.16)$$

The coefficients $a\,[i, j]$ are given in Table 3.2, and B_i are the experimental data on the total length of the persistent slip markings per unit area of the observation plane in the orientation angle range $10i \leq \alpha < 10(i+1)$ degrees. Thus, using Equation 3.13 the quantities S_j can be computed in a straight-forward manner using simple spread-sheet.

The total surface area of the bands per unit volume S_V is given by the following equation.

$$S_V = \sum_{j=1}^{j=8} S_j \tag{3.17}$$

Table 3.2: Coefficients a[i, j] obtained after simplifying Equations 3.14, 3.15 and 3.16

	j = 1	j = 2	j = 3	j = 4	j = 5	j = 6	j = 7	j = 8
i = 1	-0.00043	-0.00106	-0.00218	-0.00467	-0.0115	-0.03661	-0.18807	1.781046
i = 2	-0.0026	-0.0065	-0.01383	-0.0316	-0.08855	-0.37645	1.985531	0
i = 3	-0.00844	-0.02181	-0.04994	-0.13187	-0.50965	2.096983	0	0
i = 4	-0.02192	-0.06036	-0.15986	-0.58955	2.108598	0	0	0
i = 5	-0.05326	-0.16663	-0.61554	2.017753	0	0	0	0
i = 6	-0.13725	-0.58137	1.819905	0	0	0	0	0
i = 7	-0.46025	1.501686	0	0	0	0	0	0
i = 8	1.007639	0	0	0	0	0	0	0

Alternately, S_V can be also computed using the following stereological relationship [12].

$$S_V = \psi B_A \tag{3.18}$$

In Equation 3.18, B_A is the total length of the PSMs per unit area of the observation plane and ψ is the length-weighted mean value of the quantity [Sin α + (π/2 - α) Cosα], which can be calculated directly from the experimental data on the lengths and the orientation angles α of the PSMs. Therefore, the fraction of the total surface area of the bands G_j having the orientation angle θ_j equal to jΔ degrees is given as follows.

$$G_j = S_j / S_V \tag{3.19}$$

Where, j = 1, 2,……, 8. Using the experimental data B_i, the coefficients a [i, j] given in Table 3.2, and Equations 3.16 to 3.19 the discretized 3D angular orientation distribution function G_j of the bands can be calculated.

3.2 Measurement of the average 3-D distance between the PSBs

Experimentally determining the distance between PSBs in the bulk can be a very difficult task, even at a localized level. To be able to predict an average 3-D distance across a large volume would involve carrying out extremely difficult measurements across a large enough sample space. Instead, using stereology, one can predict the average 3-D distance of PSBs by measuring simple stereological parameters. Again, the use of stereology to predict the average 3-D distance of PSBs has been missing. Thus, this work attempts to provide a rather simple but novel method to achieve this goal.

Consider the image shown in Figure 3.3. As can be seen, if V is the total volume of the PSB colony, ΔS_i is the surface area of the i^{th} PSB and d_i is the distance (center to center) between the i^{th} and the $(i+1)^{th}$ PSB, then the total volume of the PSB colony may be given by

$$V_{col} = (d_1\Delta S_1 + d_2\Delta S_2 + d_3\Delta S_3 + \ldots\ldots + d_n\Delta S_n)/2 \quad (3.20)$$

Where n = total number of PSBs in the colony. The factor of 2 is because each PSB consists of two surfaces. Now if <d> is the average distance between the PSB's in the colony, then the individual d_i's in equation (29) may be replaced by the distance d such that

$$V_{col} = \langle d\rangle(\Delta S_1 + \Delta S_2 + \Delta S_3 + \ldots\ldots + \Delta S_n)/2 \quad (3.21)$$

$$\text{Or} \qquad V_{col} = \langle d\rangle S_{PSB}/2 \quad (3.22)$$

Where S_{PSB} is the total surface area of the PSBs in the colony. If both sides of Equation 3.22 are divided the total volume of the sample, then we get

$$V_{V,col} = \langle d\rangle\, S_{V,\,PSB}/2 \quad (3.23)$$

Where $V_{V,col}$ is the volume fraction of the PSB "colonies" while $S_{V,\,PSB}$ is the total surface area of the "individual PSBs". Therefore, the average distance between PSBs can be given by

$$\langle d \rangle = 2V_{V,col} / S_{V,\,PSB} \tag{3.24}$$

Thus, Equation 3.24 can be used for calculating the evolution of the average 3-D distance between the PSBs as a function of the number of cycles as well as strain amplitude by using two parameters, the volume fraction of the colonies, $V_{V,\,col}$ and the total surface area per unit volume of the PSBs, $S_{V,\,PSB}$ both of which can be calculated from simple measurements on 2-D planes.

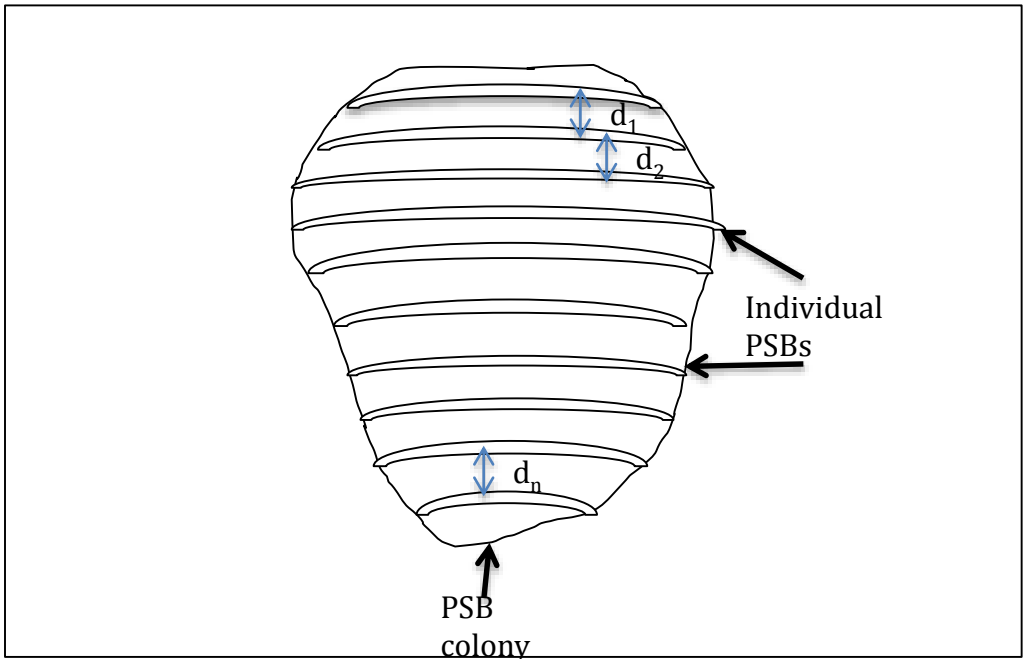

Figure 3.3: A schematic of a PSB colony showing individual PSBs and the distances between them.

The parameters introduced in this section can be used to get a unique insight into the evolution of fatigue damage and compare it across a) different microstructures or b) strain amplitudes or number of fatigue cycles within the same microstructure. Practical applications of these are given in the next section. To the best of author's knowledge, this

is the first time that these parameters are being used in the characterization of PSBs. Using these with some other well-established stereological parameters on the AHSS steels used in this study, it is proposed that the nature of fatigue damage evolution can be discussed in a novel and quantitative manner.

Chapter 4

Experimental work

4.1 Introduction

The central objective of this research is to understand the microstructural effects on the fatigue damage evolution in AHSS steels of interest through unbiased quantitative characterization of *global* microstructural fatigue damage evolution due to the formation and growth of persistent slip bands (PSBs). For this purpose, experimental work has been performed on two commercial cold-rolled dual phase steels (DP 590 and DP 980) containing different amounts of ferrite and tempered martensite constituents, and a ferritic hot-rolled high-strength-low-alloy steel, HR 590. Fatigue specimens of these commercial steels have been provided by ArecelorMittal Global R&D, East Chicago. The experimental work involved metallographic preparation of the fatigue samples, strain controlled fatigue tests, microstructural damage observations using atomic force microscopy and scanning electron microscopy, and quantitative characterization of PSB damage evolution using stereology and digital image analysis. The experimental work is described in detail in this Chapter. The chemistry of the commercial steels used in the present work and their processing are presented in the next section and that is followed by the details of the fatigue tests and the microstructural damage characterization. Numerous three-dimensional global geometric attributes of the PSBs have been estimated as a function of the number of fatigue cycles at two strain amplitudes in the steels of interest. These experimental observations and quantitative microstructural data are

presented and analyzed in the next Chapter to understand the effects of microstructure on the PSB damage evolution in the three AHSS steels of interest.

4.2 Materials and processing

The present study included three grades of steels:

a) HR 590[1] sheet steel (3.2 mm thickness), which is a hot rolled High Strength Low Alloy product.

b) DP 590[1] sheet steel (2 mm thickness), which is a dual-phase steel produced by cold rolling and water-quenched continuous anneal process.

c) DP 980[2] (2 mm thickness), which is also a dual-phase steel produced by cold rolling and water-quenched continuous anneal process.

Nominal chemical compositions of the three steels used in the present research are given in Table 4.1. Nominal quasi-static uniaxial tensile properties of these steels determined on standard JIS Transverse specimens are reported in Table 4.2.

Table 4.1: Chemical composition by weight%

Steel Grade	C	Mn	Si	Al	Mo	Trace
HR 590	0.085	1.373	0.12	0.017	-	amounts of
DP 590	0.086	0.961	0.304	0.049	-	P, N, V, Ti,
DP 980	0.092	2.081	0.691	0.039	0.075	Nb etc.

[1] 590 is the minimum tensile strength value (in MPa) for the commercial HR 590 and DP 590 steels

[2] 980 is the minimum tensile strength value (in MPa) for the commercial DP 980 steel

Table 4.2: Tensile properties

Steel Grade	Yield Stress (MPa)	Ultimate Tensile Strength (MPa)	Uniform Elongation (%)	Total Elongation (%)
HR 590	568	655	10.7	23.34
DP 590	337	612	16.88	27.93
DP 980	716	1016	7.19	14.66

4.3 Sample machining

The steel specimen-blanks have been drawn from the as-produced coils and samples with "dog-bone" geometry (Figure 4.1) have been machined at ArcelorMittal Global R&D. As shown in the figure, the width of these specimens is along the rolling direction whereas the length (loading direction) is transverse to the loading direction. The final specimen dimensions deviate from those found in ASTM E606-04 *Standard Practice for Strain Controlled Fatigue Testing [149]* by using a square gage dimension to minimize chances of buckling during fatigue testing.

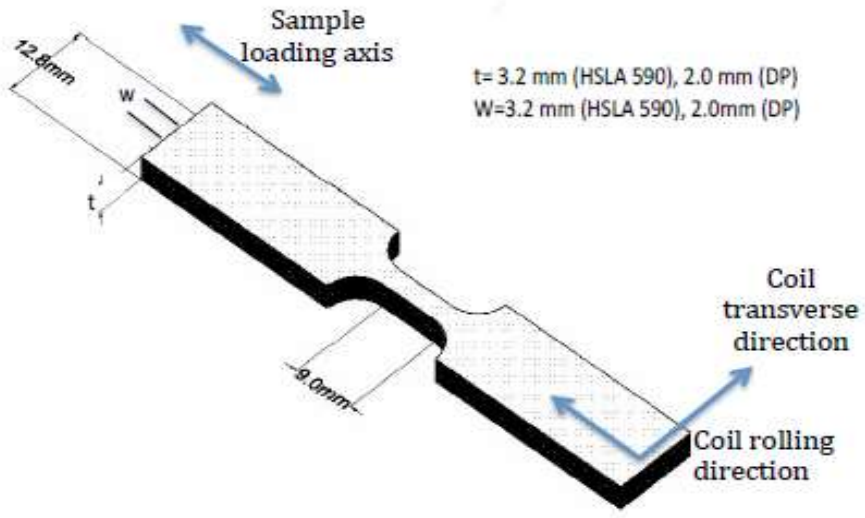

Figure 4.1: Fatigue specimen geometry.

4.4 Metallography and specimen surface preparation

The specimens were polished on all four sides of the gage section using the standard metallographic techniques. This is done in order to a) facilitate microscopy, b) remove any effect of surface conditions or machining and c) bring all specimens to the same standardized specimen surface state. Care was taken to de-burr the edges in order to ensure that there were no regions of stress localization and to remove metal shavings. The surfaces containing the rolling and the transverse directions (planar surfaces) were polished using a polishing wheel and the other two planes were polished manually. The polishing steps included coarse grinding (till 600 Grit carbide paper) followed by polishing steps using progressively finer diamond suspensions. After 1-micron diamond polish, the final polishing was done using 0.05-micron suspended colloidal silica to give a mirror-like high quality finish (Figure 4.2). A silicone film was applied on the polished sides after polishing of the first planar surface is completed. This was done in order to protect the surface during the polishing of the second planar surface. This film was peeled off once the polishing of the second planar surface was completed. After the surface preparation and prior to further testing, the gage dimensions were measured using an Optical Measuring Profile Projector accurate to +/- 0.01 mm. These measurements have then been used to calculate the stresses from the loading data.

4.5 Fatigue testing

In order to carry out the fatigue testing, a silicone caulk was applied on one of the sides of the specimens. Grooves were made on the caulk and an extensometer was affixed to the specimens by sliding its blades into these grooves and using small rubber bands. The

extensometer used has an 8 mm gage length. Strain controlled fatigue tests were then carried out on the specimens using the MTS Servo-hydraulic test system (rated capacity of 50 kip) at

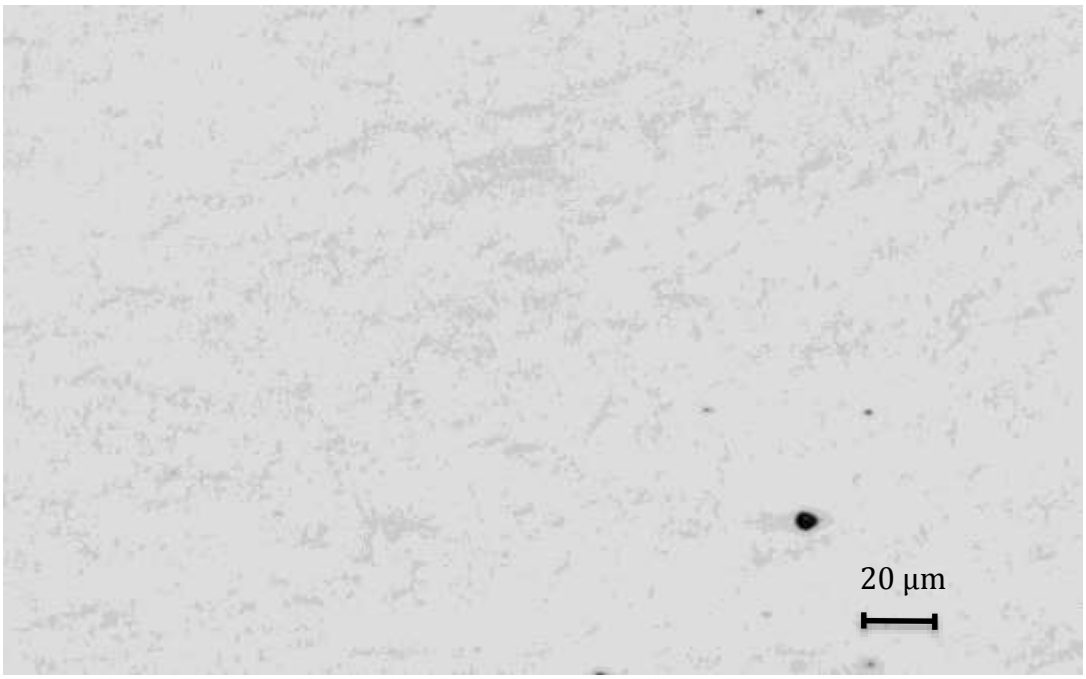

Figure 4.2: A representative micrograph for the as-polished surface finish for HR 590 steel.

a strain rate of 0.001 mm/mm per second. All fatigue experiments were performed in accordance with ASTM E606-04 [149]. A drop in load of greater than 50% of the maximum load at the end of the first cycle was considered to be a failure and the fatigue testing was stopped. The fatigue testing was always done in fully reversed mode (R = -1) and using a triangular waveform. The first set of tests (Set I) was carried out at several strain amplitudes to failure in order to determine the strain life curves for all three steel grades.

In order to determine the evolution of fatigue related damage, interrupted fatigue tests have been conducted (Set II). These tests were conducted at two strain amplitudes. Interrupted tests on all three steels were conducted at the higher strain amplitude while

the lower strain amplitude tests were conducted only on DP 590 steel. The strain amplitudes were determined such that plastic deformation was the dominant mode of deformation at the higher strain amplitude (Low Cycle Fatigue) while elastic deformation was the dominant deformation mode at the lower strain amplitude (High Cycle Fatigue). Ensuring a reasonable testing time, and ensuring the absence of buckling during cyclic loading were the other criteria used for this determination. Based on these factors, total strain amplitude $\Delta\varepsilon_T/2 = 1.0\%$ was selected as the higher strain amplitude while $\Delta\varepsilon_T/2 = 0.2\%$ was selected as the lower strain amplitude. Such tests, when conducted at the same strain amplitude (1.0%) on the three AHSS steels have been used to study the effect of *microstructure* on the damage. Similarly, the data obtained from tests at 1.0% ($N_f \approx 500$ cycles) and 0.2% ($N_f \approx 10^5$ cycles) total strain amplitudes for DP 590 steel have been used to study the effect of *strain amplitude* on fatigue damage evolution.

Damage accumulation curves (average absolute cyclic stress v/s cumulative plastic strain) for the samples fatigued at $\Delta\varepsilon_T/2 = 1.0\%$ from Set I of tests were obtained for each of the three AHSS steels. One such curve for DP 590 specimen is shown in Figure 4.3. The mean absolute cyclic stress for a particular cycle, *N* is the average of the magnitude of the peak stresses in the tension and compression half cycles for cycle number *N*. The cumulative plastic strain, $\varepsilon_{pl,\,cum}$ was calculated using Equation 4.1. In the equation, $\Delta\varepsilon_p/2$ corresponds to the plastic strain amplitude at half life. These damage accumulation curves were used to determine the cycles after which the tests from Set II were interrupted. Several other works have shown that the central plateau region (represented approximately by a cumulative plastic strain between 0.2 and 2 in Figure 4.3) is often the region where most of the PSB formation and growth occurs [16, 70, 150,

151]. Thus the tests for Set II were interrupted at several cycle numbers corresponding to the plateau region.

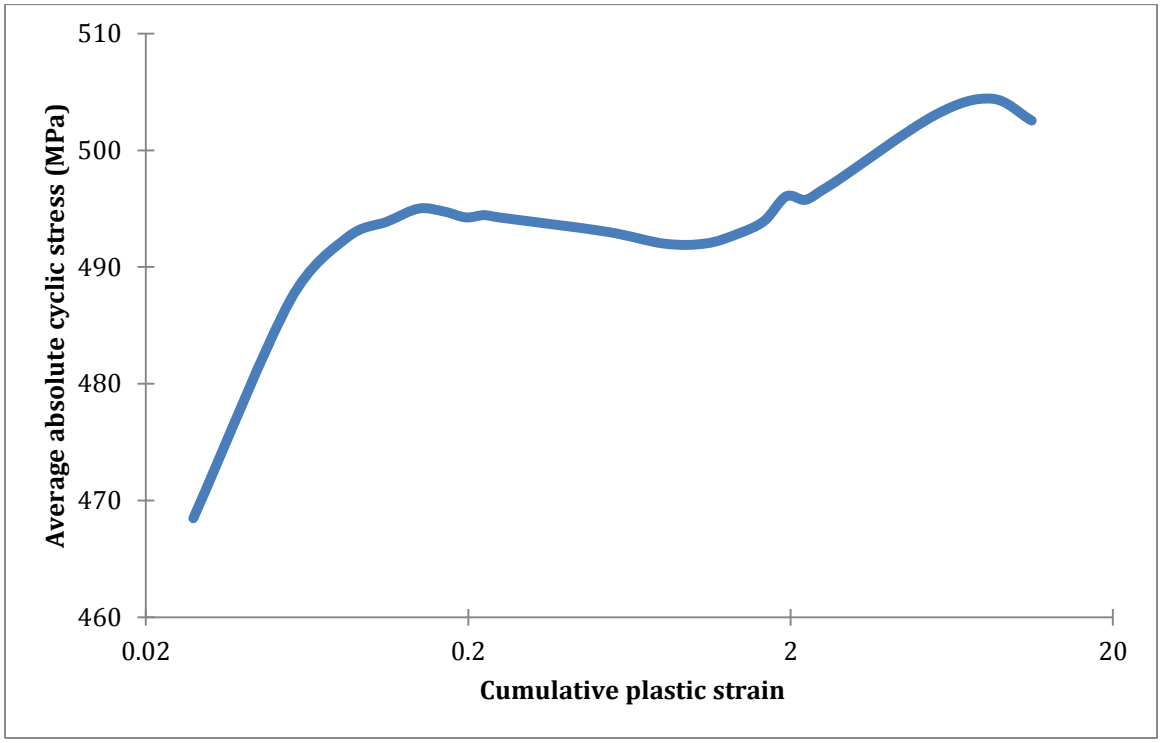

Figure 4.3: Damage accumulation curve for DP 590 steel fatigued at ε_T = 1.0%.

$$\varepsilon_{cum,\,N} = 4 \text{ x } N \text{ x } \Delta\varepsilon_p/2 \qquad (4.1)$$

Following each interruption in the Set II of the tests, the sample was retrieved and images of the gauge section were captured as described in the next section. This imaging enabled the study of the evolution of microstructure as a function of number of cycles. The sample was then put back in the MTS servo hydraulic machine and testing resumed. This process was repeated until the sample failed. The criterion of failure and all other testing conditions were the same as for Set I.

4.6 Microstructural and PSB damage characterization

After the fatigue testing, samples were etched using 2% nital in order to reveal the microstructure (Figure 4.4). In order to make quantitative measurements, the sample surface was characterized using SEM (Hitachi SU8030). All the images were taken from the central one-third region of the gage section. This was done to minimize any edge effects. The orientation of the sample was kept constant while grabbing the images such that the horizontal direction always represented the loading direction. Within this region, the images were grabbed using uniform random sampling (ref. section 2.3.1.2). Thus all image positions were located on a uniform grid with the location of the first grid point chosen at random within the central one-third region of the gage section with an area of approximately 2 mm^2. This methodology has been schematically shown in Figure 4.5. The sampling error for this method is a strong function of the number of locations at which the images are grabbed. It has been shown that for most microstructures, $n \geq 50$ is sufficient [131, 133, 152]. Therefore for the purpose of this study, 80-100 images each at 4000X or 5000X were grabbed from the central one-third region in order to make sure that the quantitative data obtained had a low sampling error, while at the same time, the calculations were not unreasonably tedious. The total area of such images was about 0.05 mm^2. One such sample image for DP 590 steel is shown in Figure 4.6. Quantitative measurements on the SEM images were made using the image analysis software called "ImajeJ" provided by the National Institutes of Health (NIH) [153]. Some of the advantages of using this software were:

1. The software is compatible with both Mac OS X and Windows operating systems.

2. Both the software and its Java source code are freely available.
3. Measurements can be easily calibrated in the desired units.
4. The software is compatible with most commonly used image file formats.
5. Easy to work with a collection of images of different magnifications.
6. Availability of convenient analysis and measurement tools such as for measuring area, lengths, and angles of randomly shaped features within the image.

4.6.1 *Bulk microstructure characterization*

4.6.1.1 Volume fraction estimation of ferrite/martensite

Systematic uniform random point counting technique (ref. section 2.3.1.2) was used to estimate the volume fraction of the ferrite and martensite phases in DP steels. For this purpose a uniform grid of $P_T = 20$ points was placed randomly on each of the images obtained from the SEM and the number of points falling on the martensite phase (N_M) was counted manually. Thus the point fraction for the i^{th} image ($P_{P,i}$) is given by:

$$P_{P,i} = \frac{P_{M,i}}{P_T} \tag{4.2}$$

In this calculation, points that fall on the ferrite/martensite interface are counted as 0.5 [152]. Let the total number of images recorded from the SEM be sufficiently large and denoted by n (n>50 and varies with each measurement set). Then estimated value of the population average point fraction $<P_P>$ with the associated confidence interval is calculated using Equation 4.3 given below:

$$< P_P > = \frac{\sum_{i=1}^{n} P_{P,i}}{n} \pm 2 \left[\sum \left(< P_P > - P_{M,i} \right)^2 \Big/ \{ n(n-1)(P_T)^2 \} \right] \tag{4.3}$$

Using Equation 2.2 and Equation 4.3, the volume fraction of martensite can be estimated as:

$$V_V = < P_P > = \frac{\sum_{i=1}^{n} P_{P,i}}{n} \tag{4.4}$$

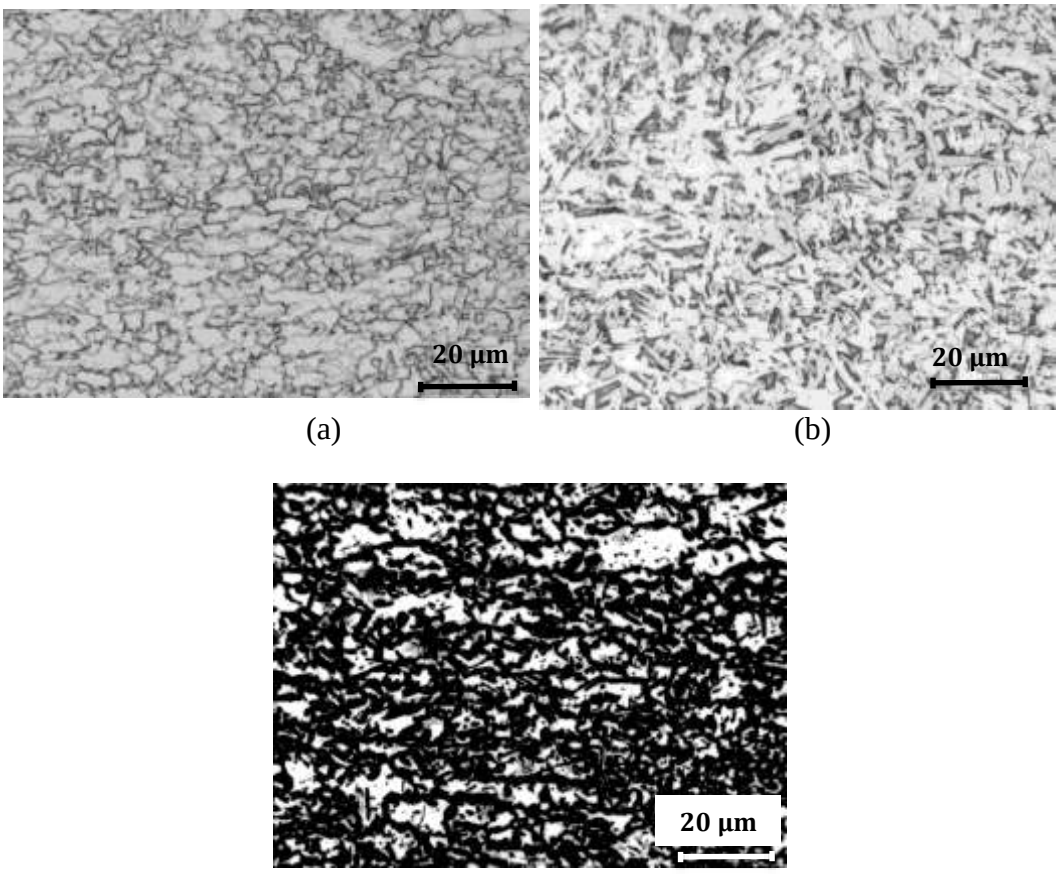

(a) (b)

(c)

Figure 4.4: Optical micrographs of a) HR 590; b) DP 590 and c) DP 980 steels. All 3 steels have been nital etched. The DP 980 steel has been etched additionally with 10% sodium metabisulphite for 10 seconds.

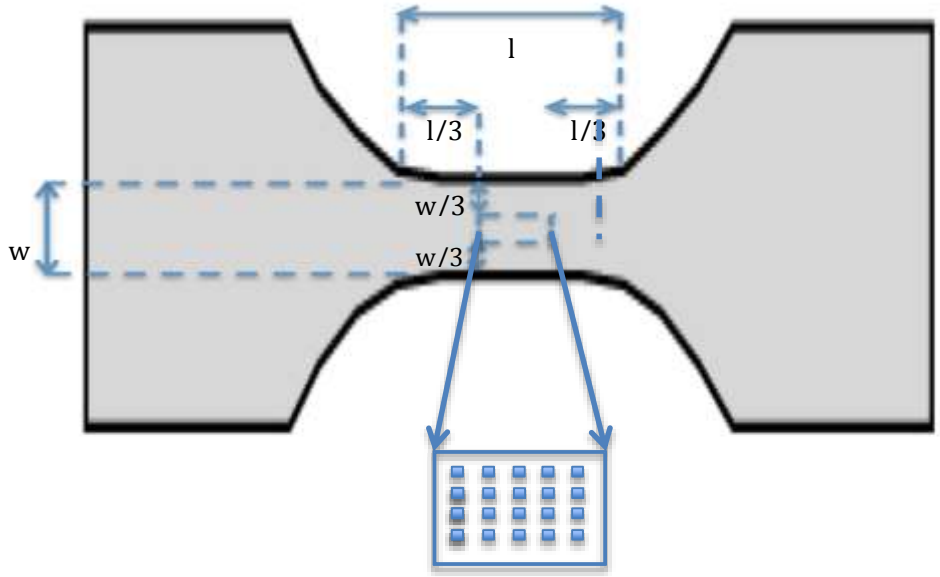

Figure 4.5: Schematic of the central 1/3rd region of the gage section used for grabbing the SEM images. The region has been blown up to show a representative grid of images.

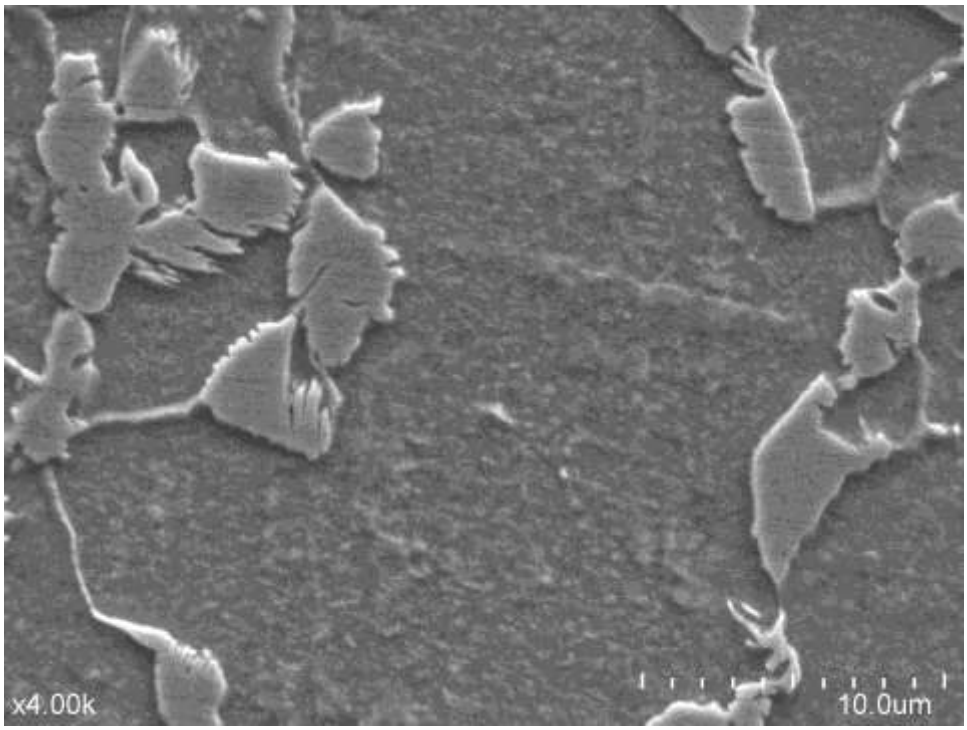

Figure 4.6: A sample SEM image for DP 590 used for making quantitative measurements.

4.6.1.2 Estimation of length scale of ferrite islands in DP 980 steels

The DP 980 microstructure consists of ferritic islands interspersed in a martensitic matrix (Figure 4.7). There are no grain boundaries visible in the ferrite islands, indicating

that on an average, the length scale of the islands is lower than the ferrite grains. To estimate the length scale of these islands, the mean intercept length of ferrite has been utilized. First, using straight line probes, the number of intersections with the ferrite-martensite interfaces per unit test line length have been counted. Assuming the microstructure to be isotropic, measurements made on only one metallographic plane (the planar surface of the specimen in this case) were sufficient (ref. Section 2.3.2). Thus a grid was placed on each of the images containing four lines each parallel and perpendicular to the loading axis. The average value the number of intersections, $<P_L>$ was obtained. It should be noted here that the tangent points were counted as ½. Similarly, if the test line ended on the interface boundary, it was also counted at ½. Now using Equation 2.8, surface area of the ferrite-martensite interfaces per unit sample volume ($S_{V,F/M}$) is estimated. Using the volume fraction of ferrite ($V_{V,F}$) obtained from Section 4.6.1.1, this interface area can now be used to estimate the mean intercept length of ferrite. The ferrite mean intercept length can be used as an estimate of the length scale of the ferrite islands using Equation 4.5.

$$< d > = \frac{4(1-V_{V,F})}{S_{V,F/M}} \tag{4.5}$$

4.6.1.3 Estimation of ferrite grain size in HR 590 and DP 590 steels

Planimetric grain counting procedure [154] has been used to estimate the ferrite grain size in HR 590 and DP 590 samples. The images recorded using uniform random sampling (ref. section 2.3.1.2) were used for this purpose. In this method, the total area of the microstructural image, A is obtained using "ImageJ". Then the number of ferrite grains within the area of the image is counted. The sum of all the grains included completely within the known area A (N_{inside}) plus one half the number of grains

intersected by the circumference of the area ($N_{\text{intercepted}}$) gives the number of equivalent whole grains within the area A as shown in Equation 4.6.

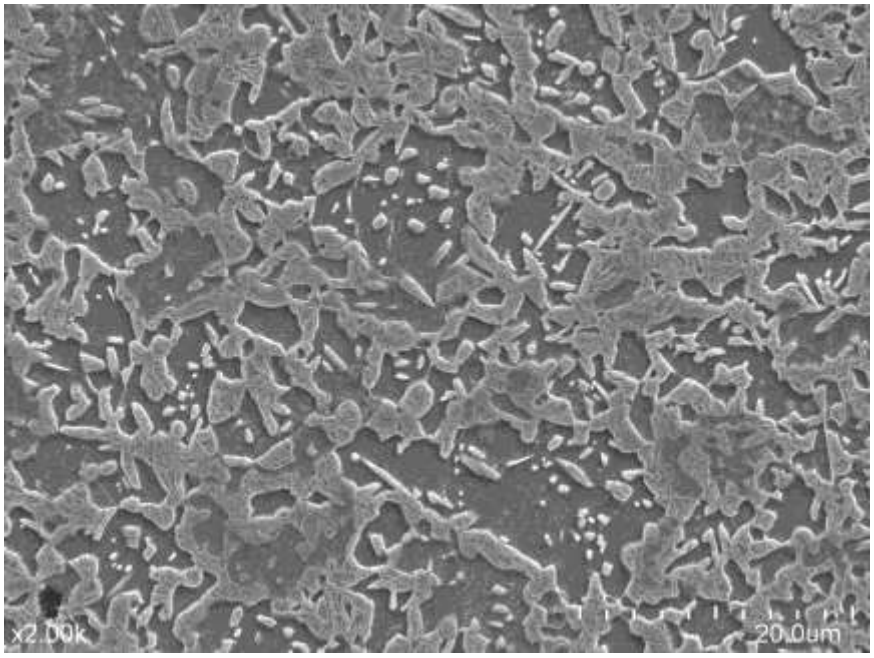

Figure 4.7: SEM image of DP 980 microstructure.

$$N_A = \left(\frac{N_{inside} + \frac{N_{intercepted}}{2}}{A_T} \right) \tag{4.6}$$

Here A_T is the total area of each field of view as measured in the software. Thus the average ferrite grain area, A_F is the reciprocal of N_A. Additionally, the mean ferrite grain diameter, d is the square root of A_F. This grain size assumes that the average grain cross section is a square. Nonetheless, this size does provide an estimate of the *scale* of the mean ferrite grain size.

4.6.2 *PSB characterization*

As described in Section 2.2.3, the PSBs manifest themselves on the surface in the form of parallel features called extrusions and intrusions. Together they are known as the Persistent Slip Markings (PSMs). A collection of at least three of these PSMs within a

grain has been defined as a PSB "colony". The PSMs within a colony are of the same angular orientation with respect to the loading direction. One such colony within a ferrite grain of DP 590 microstructure has been marked in Figure 4.8. Several aspects of these colonies have been characterized by making two-dimensional measurements using the image analyzing software on both the colonies as well as the individual PSMs.

The area of individual PSB colonies, A_C has been measured by using the software to trace the individual colonies manually within each microstructural image and using the in-built area calculator. One such trace is shown in Figure 4.8. The total area of all the colonies across all images is added and the sum is divided by the total area of all fields of view, A_T. Thus the average two-dimensional area fraction of the colonies, $<A_{A,C}>$ is obtained. Since the fields of view have been chosen randomly, they sometimes may cut across some colonies. In such cases, only the area of the colony within the field of view is counted. An illustration of such a case is shown in Figure 4.9 with the area of the colony to be counted has been marked as region A. Grains with visible slip activity in terms of formation of distinct PSB colonies have been termed as "*active grains".* A similar trace is made manually on all active ferrite grains and their average area fraction, $<A_{A,F\_act}>$ with respect to A_T is also calculated. Just like in the case of colonies, if an active ferrite grain is cut across by the boundaries of the field of view, only the area within the field of view (Region B in Figure 4.9) is to be counted. Now applying equation 2.5 to these area fractions, we get:

$$< A_{A,C} > = V_{V,C} \tag{4.7}$$

$$< A_{A,F\_act} > = V_{V,F\_act} \tag{4.8}$$

The same traces used for measuring colony areas can also be used for measuring the two dimensional perimeter of the colonies (L_C) using the built-in perimeter measuring tool of the ImageJ software. The sum of perimeters of all the colonies divided by total area, A_T results in obtaining the average colony perimeter per unit area ($<L_{A,C}>$). It should be noted that if the colony is cut across by a fields of view, any portion of the boundary of the field of view is not to be counted in the perimeter measurement. In other words, only the double-lined portion of region A in Figure 4.9 should be counted in the measurement of perimeter of the colony. Now using equation 2.8, the three-dimensional surface area per unit volume of the PSB colonies, $S_{V,C}$ can be estimated as:

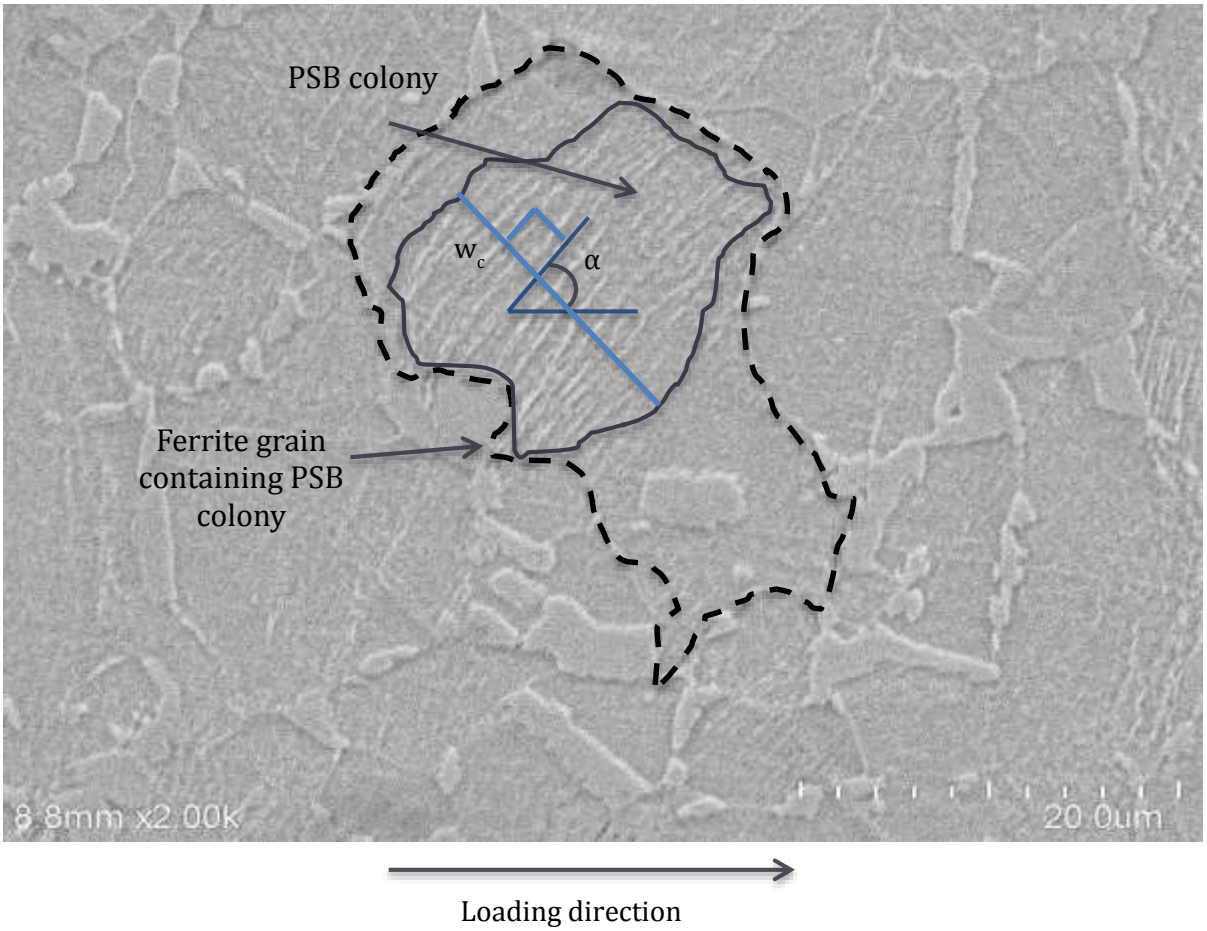

Figure 4.8: Image showing PSB colony within a DP 590 microstructure. α is the two-dimensional orientation of the PSBs with the loading axis.

$$S_{V,C} = \frac{4}{\pi} < L_{A,C} > \quad (4.9)$$

The two-dimensional angular orientation of the PSBs has also been measured. For this, all PSBs within a colony have been assumed to be parallel. Then, the angle α of any one of the PSMs with respect to the loading axis (horizontal direction of the images) is recorded using the in-built angular measurement tool within ImageJ software. This angle α is more clearly shown in Figure 4.10. In the initial measurements, it was determined that α varied between 10^o and 90^o. Thus all values of α were grouped in 8 bins such that the 1st bin corresponded to $10^o \leq \alpha < 20^o$, 2nd bin corresponded to $20^o \leq \alpha < 30^o, \ldots.$, and 8th bin corresponded to $80^o \leq \alpha < 90^o$.

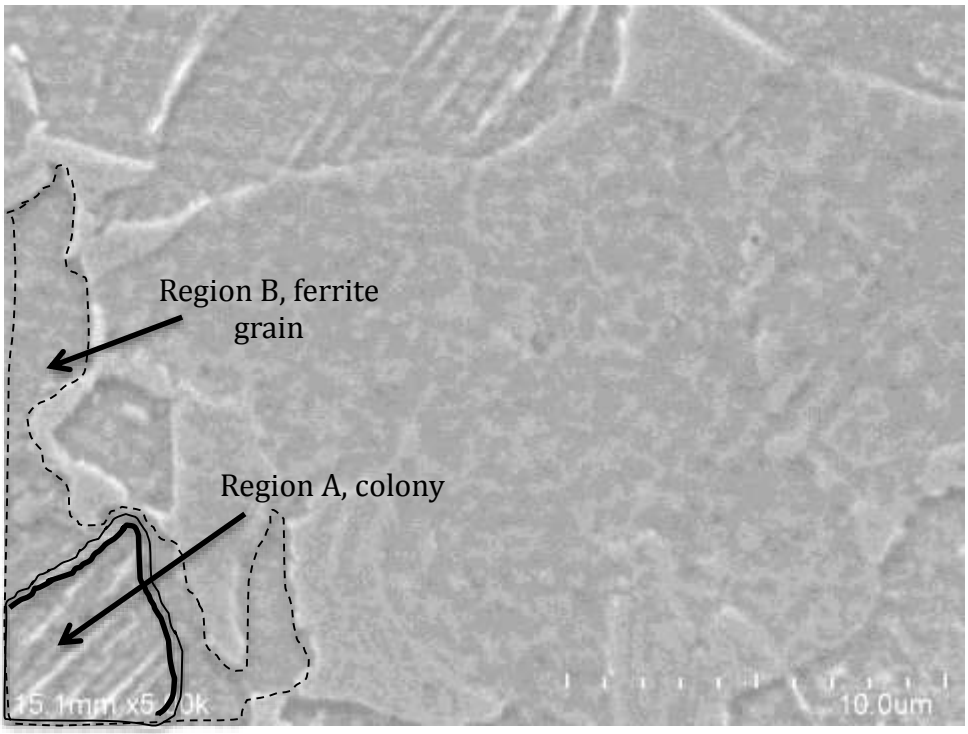

Figure 4.9: SEM image showing an example of a PSB colony and an active ferrite grain being intersected by the boundaries of a field of view in DP 590 steel.

Next, the width of the colony, w_c is measured by drawing a line across the colony and perpendicular to the orientation of the extrusions as shown in Figure 4.8. The number

of PSMs, N_{PSM} are counted manually. Then, the average two-dimensional distance between successive PSMs within the colony, $d_{PSM,\ 2\text{-}D\ avg}$ can be obtained by:

$$d_{PSM,2-D\ avg} = \frac{w_c}{N_{ext}-1} \tag{4.10}$$

Thus, the total length of PSMs within a colony (all oriented at angle α with respect to the loading axis) denoted by $l_{PSM,\ c,}$ can be obtained by the Equation 4.11 below.

$$l_{PSM,\ c} = \frac{A_C}{d_{PSM,2-D\ avg}} = {A_C}\Big/{\frac{w_c}{N_{PSM}-1}} \tag{4.11}$$

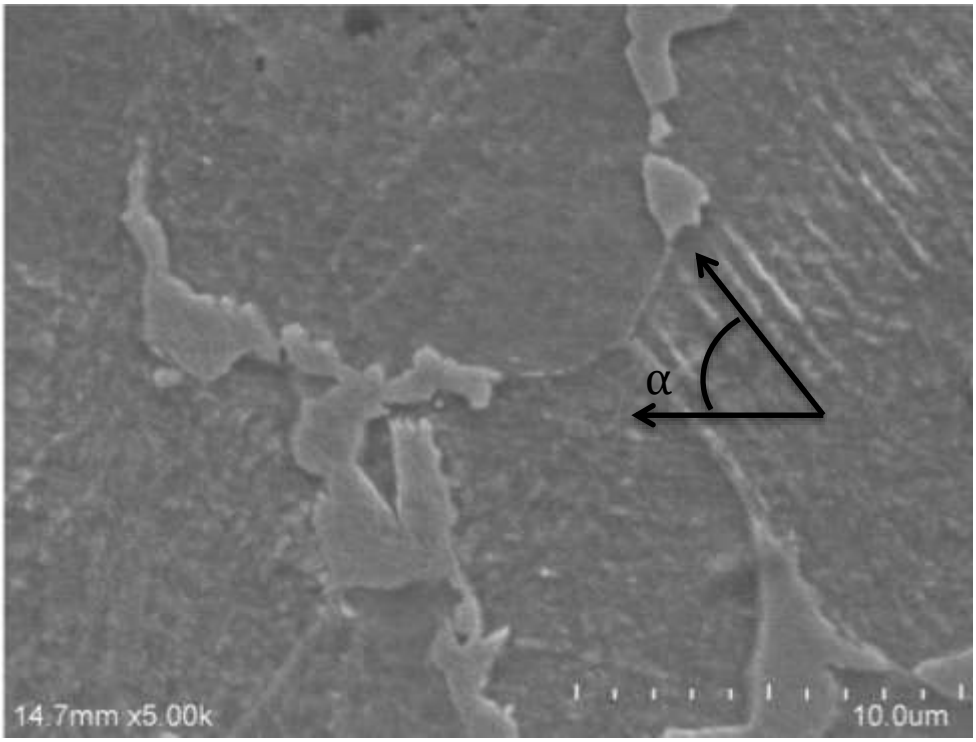

Figure 4.10: Image showing the measurement of angle α. Horizontal direction represents the loading axis.

This way, the total lengths of all PSMs within a colony are estimated using Equation 4.11. The lengths of all PSMs within a bin of range $\theta \leq \alpha < (\theta + 10^o)$ are added. Dividing with total area, $A_{T,}$ the total PSM length per unit area of the observation plane having measured two dimensional orientation angles in the range $\theta \leq \alpha < (\theta + 10^o)$ originating from all possible three dimensional orientations of the colonies is obtained.

This is the same as B_i from section 3.1. One such example of normalized length weighted two-dimensional angular distribution for DP 590 after 80 cycles and from 100 images is given in Figure 4.11.

Using the development described in Section 3.1, this distribution can be used to obtain the discretized three-dimensional angular distribution of PSMs. One such normalized distribution is shown in Figure 4.12 for DP 590 steel after 80 cycles at 1.0% strain amplitude. The fractions of discretized 3-D angles 20^o and 30^o have been combined for ease of analysis. Similarly, the fractions of discretized 3-D angles 40^o and 50^o have been also been combined. No 3-D angles greater than 60 have been observed.

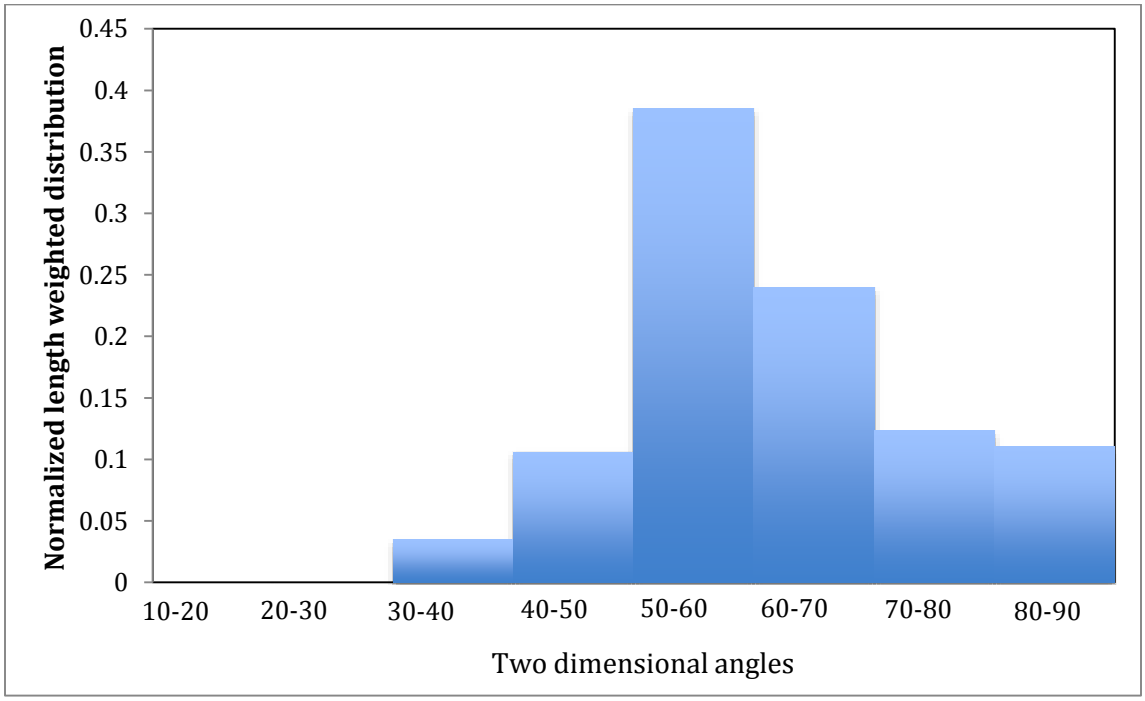

Figure 4.11: Normalized length weighted two–dimensional angular distribution of PSMs after 80 cycles of fatigue at 1.0% strain amplitude for DP 590 steel. Y-axis denotes the fraction of total PSM length oriented at an angle α within the corresponding angular range.

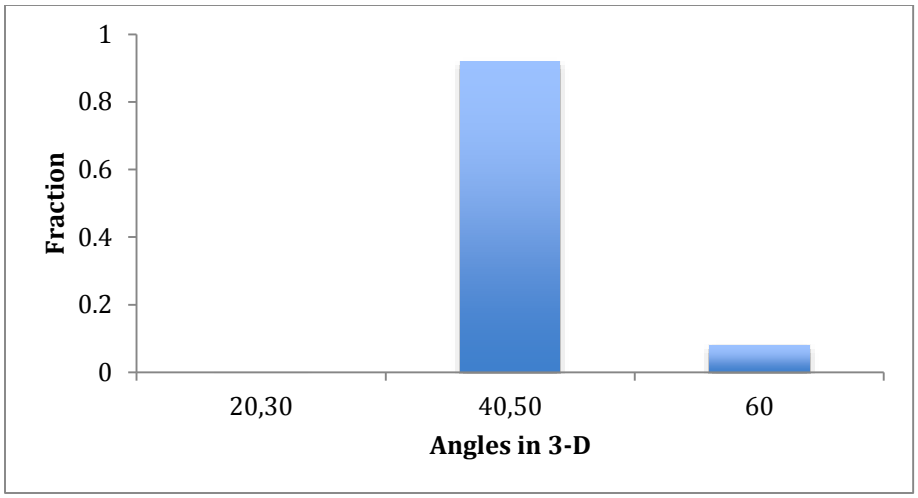

Figure 4.12: Estimated normalized three dimensional angular distribution of PSMs for DP 590 steel fatigued at 1.0% strain amplitude for 80 cycles.

Further qualitative analysis on the DP 590 microstructure was done using AFM. AFM analysis enabled the characterization of height of surface PSMs thus helping the study of the PSM topography. The experiments were done in the tapping mode and using suitable probes. The equipment used for this part of the study was the "Dimension 3100 Scanning Probe Microscope (SPM)". The software used for generating and processing data was Nanoscope 7.3 by "Digital Instruments". Tap 300 Al-G probes (rotated, monolithic silicon AFM probes for high frequency applications) supplied by NanoAndMore USA Inc. were used. An applied voltage caused the cantilevers on the probes to vibrate at controlled frequencies. The amplitudes of these vibrations provided a measure of the local surface topography. The typical applied voltage was 1500 mV. The start and end frequencies used were 2 KHz and 500 KHz respectively. The cantilever resonant frequencies were typically within this range. The scan sizes were typically around between 5 μm and 100 μm in both x and y directions. The tip velocities varied between 10 μm/sec and 50 μm/sec. A sample AFM image is shown in Figure 4.13.

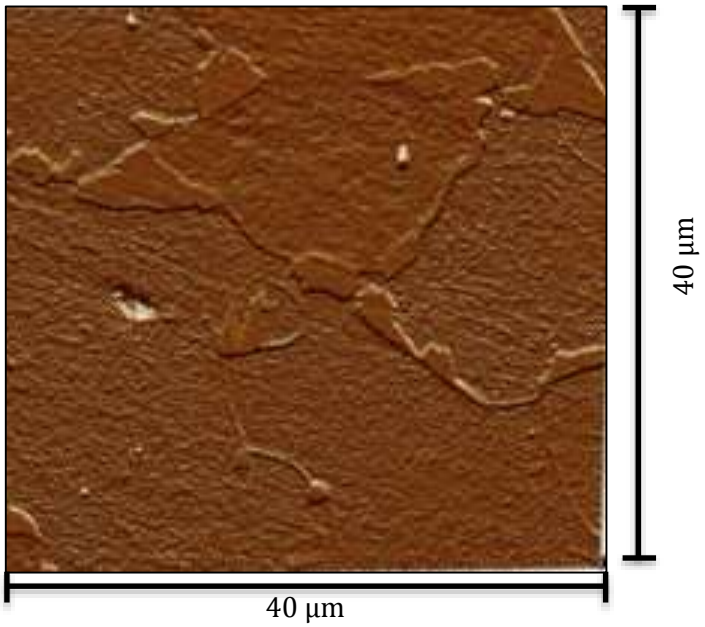

Figure 4.13: Sample AFM image of a DP 590 microstructure.

Chapter 5

Results and Discussions

5.1 Introduction

In this research, a series of strain controlled fatigue tests have been performed on two cold-rolled commercial dual phase steels (DP 590 and DP 980) having different relative amounts of ferrite and tempered martensite constituents, and a ferritic hot-rolled HSLA steel (HR 590). The PSB damage in these three AHSS steels has been quantitatively characterized as a function of number of fatigue cycles at two strain amplitudes using global stereological attributes. These experimental details have been reported in the previous chapter. In this Chapter, the experimental data are critically analyzed to develop an in-depth understanding of the effects of microstructural parameters such as ferrite volume fraction and grain size on the global PSB damage evolution. The next section of this chapter reports the mechanical response of the steels during monotonic loading and during strain-controlled fatigue as well as strain-life data, which is followed by analysis of bulk microstructures. The quantitative data on PSB damage and their analysis are presented in the subsequent sections of the Chapter. The analysis of these quantitative data leads to a simple model for the global microstructural evolution of the PSB colonies and how the microstructural parameters such as ferrite volume fraction and grain size affect the path of PSB damage evolution, which leads to important conclusions of the research. These conclusions are reported in the next Chapter.

5.2 Mechanical properties

5.2.1 *Monotonic mechanical properties*

The monotonic tensile response of DP 590, DP 980 and HR 590 steels is shown in Figure 5.1. The monotonic response can be modeled using a Holloman power law relationship of the kind shown in Equation 5.1 [155]. Here σ is the stress response, K is the strength coefficient that represents the theoretical stress when plastic strain is equal to one, ε_p is the plastic strain and n is the strain-hardening exponent that describes the decrease in the slope of stress-strain curve with an increase in the plastic deformation.

$$\sigma = K{\varepsilon_p}^n \tag{5.1}$$

It is observed that the HR 590 curve shows yield point elongation, which is an increase in the strain without a corresponding change in stress at the onset of yielding. It is characterized by a plateau in the stress-strain curve and results from a critical strain energy that allows the unpinning of dislocations [156]. While the dislocation mobility in HR 590 provides discontinuous stress-strain response, the stress-strain response in DP 590 and DP 980 (which are nearly free of dislocation pinning precipitates) is more continuous as can be seen in Figure 5.1.

Comparing the two microstructures at the same strength level (DP 590 and HR 590), one can observe that the dual phase steel provides a greater rate of work hardening, which can be quantified by a higher work hardening exponent or *n*-value (0.1723 for DP 590 as compared to 0.1007 for HR 590) and the higher strength coefficients or *K*-value (987 MPa for DP 590 as compared to 912 MPa for HR 590). Differences in work hardening have been partially attributed to movement of dislocations by precipitates [157]. The mobility of dislocations within the grains is of particular importance to the

work hardening of the two steels. HSLA steels, such as HR590, show an increase in dislocation density at the grain boundaries [157]. In dual phase steels, such as DP 590, the dislocation density is greater at those grain boundaries where there is a martensite-ferrite interface [58, 128, 158]. Thus, more strain localization is expected to occur in the ferrite grains of dual phase 590, especially around the ferrite-martensite interface as compared with the HR 590 ferrite. Therefore, HR 590 steel may allow strain to be accommodated over a larger volume and requires a larger stress to unpin dislocations, which is made more difficult by the presence of precipitates. The concentrated stress along with the lack of precipitates in DP 590 can cause the deformation to be accommodated by the creation of fresh mobile dislocations in ferrite to accommodate strain at the interface. The generation of mobile dislocations and the subsequent pinning can explain work hardening in the ferrite, which is evident by the higher work hardening exponent [45].

Comparing the two dual phase microstructures, the higher *K*-value of DP 980 is easily explained by the presence of higher martensite volume fraction. The higher *n*-value in DP 590 steel indicated higher work hardening. Similar observations were made by Farabi et al. [159] and Kim and Thomas [160] and the cause was attributed to the presence of a larger amount of easily deformable ferrite in DP 590 steels.

5.2.2 *Mechanical properties under cyclic loading*

This section presents results from low cycle strain controlled fatigue experiments performed on HR 590, DP 590 and DP 980 steels and analyzes the response to cyclic loading as function of strain amplitude and microstructure.

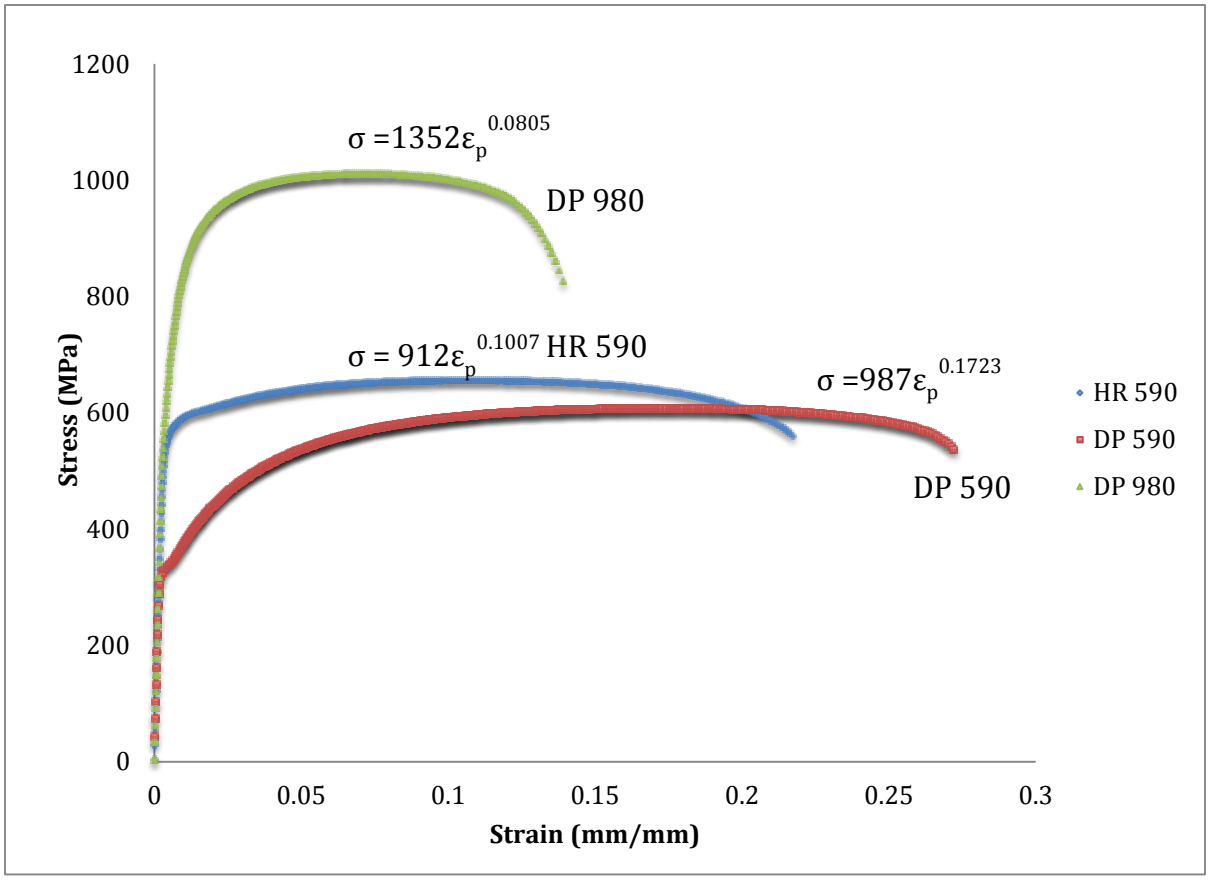

Figure 5.1: Monotonic stress-strain response for HR 590, DP 590 and DP 980 with corresponding parameters for a power law relationship of the type $\sigma = K{\varepsilon_p}^n$.

5.2.2.1 Stable hysteresis loops

Steels subjected to cyclic loading in the plastic deformation regime have a non-linear stress-strain response in the form of a hysteresis loop. In order to look at the differences in the nature of damage accumulation for the three steels, the stress-strain response in the form of hysteresis loops for the steels at 1.0% total strain amplitude at half-life has been analyzed. It was observed that the flow stress changed to account for variations in plastic deformation but the hysteresis loops for all three steels stabilized around 0.25 N_f and remained stable till around 0.75 N_f. Thus, the hysteresis loops at 0.5 N_f (half-life) have been compared (Figure 5.2).

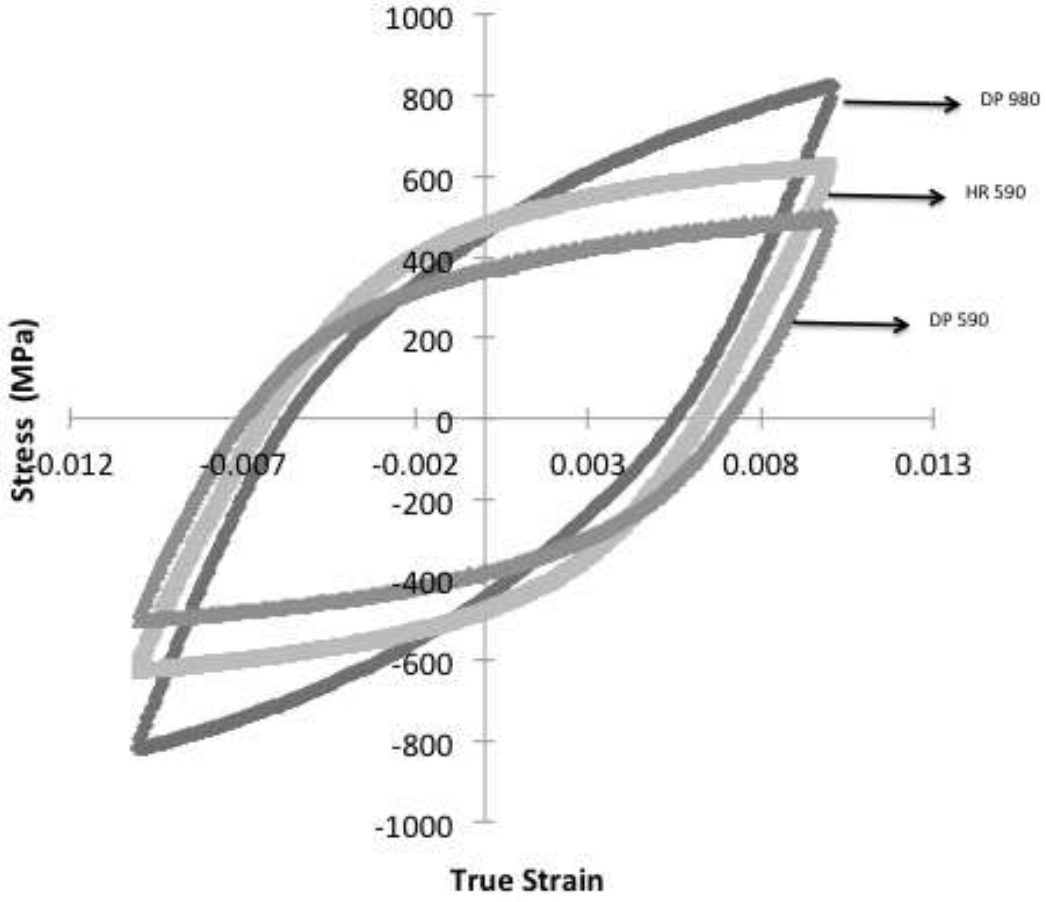

Figure 5.2: Stable hysteresis loops at 1.0% total strain amplitude for DP 590, HR 590 and DP 980 steels at half-life.

The stable hysteresis loops were used for calculating the relative contributions of the elastic and plastic deformation within each of the steels. The total strain within a quarter cycle is a sum of the elastic and plastic strains as shown in Equation 5.2.

$$\frac{\Delta\varepsilon_T}{2} = \frac{\Delta\varepsilon_{el}}{2} + \frac{\Delta\varepsilon_{pl}}{2} \tag{5.2}$$

While the elastic contribution is recovered completely after each cycle, the plastic strain component, $\frac{\Delta\varepsilon_{pl}}{2}$ is not recoverable and gets accumulated constantly as the cycling continues. It is this plastic component that causes strain localization to occur within the material, first leading to the formation of PSBs and ultimately to cracks. The plastic strain

range every half cycle, $\Delta\varepsilon_{pl}$ is given by the width of the hysteresis loop at zero stress. Assuming the plastic strain range, $\Delta\varepsilon_{pl}$ calculated for the hysteresis loop at half-life remains the same across all cycles, the total cumulative plastic strain after *N* cycles can be given by Equation 5.3 as:

$$\varepsilon_{pl,cum} = 2 \cdot N \cdot \Delta\varepsilon_{pl} \tag{5.3}$$

At half-life, the plastic strain amplitude for a quarter cycle can be approximated by $\Delta\varepsilon_{pl}/2$. Then using Equation 5.2, the elastic component of strain amplitude every quarter cycle is given by:

$$\Delta\varepsilon_{el}/2 = \Delta\varepsilon_{T}/2 - \Delta\varepsilon_{pl}/2 \tag{5.4}$$

Using this methodology, the elastic and plastic strain components at half-life for the three steels at different strain amplitudes is given in Tables 5.1, 5.2 and 5.3.

In order to study the effect of strain amplitude on fatigue damage evolution, strain-controlled fatigue tests have been carried out in DP 590 steels at two strain amplitudes. The strain amplitudes were chosen such that plastic deformation was dominant at the higher strain amplitude for all three steels while elastic deformation was dominant at the lower strain amplitude. Evaluating the data shown in Table 5.1, these strain amplitudes were determined to be 1.0% and 0.2%.

5.2.2.2 Damage accumulation curve

The total cumulative plastic strain, $\varepsilon_{pl,cum}$ can be used to describe the evolution of fatigue related damage in a material. This can be done using a *damage accumulation curve*. Such curves have been described in detail in section 4.5. The damage accumulation curves for all three steels fatigued at several strain amplitudes are shown in

Figure 5.3(a)-(c). Near the end of fatigue life a crack initiates and propagates leading to a rapid decrease in the load bearing capacity of the steel. However, for the purpose of this study, the data of interest is prior to the sharp decrease in load.

Table 5.1: Elastic and plastic strain components and cyclic stress amplitude at half life for HR 590

Sample Designation	Total strain amplitude, $\frac{\Delta\varepsilon_T}{2}$ (%)	Half-life Data			First quarter cycle peak stress (MPa)	Cycles to failure (N_f)
		Plastic strain amplitude, $\frac{\Delta\varepsilon_{pl}}{2}$ (%)	Elastic strain amplitude, $\frac{\Delta\varepsilon_{el}}{2}$ (%)	Cyclic stress amplitude, $\frac{\Delta\sigma}{2}$ (MPa)		
R-1	2.0	1.62	0.38	606	631	94
R-2	1.7	1.34	0.36	620	646	148
R-14	1.4	1.07	0.33	672	638	188
R-17	1.0	0.63	0.37	622	637	527
R-9	0.8	0.51	0.29	637	590	457
R-10	0.5	0.23	0.27	570	612	2207
R-11	0.35	0.11	0.24	522	574	5176
R-12	0.2	0.005	0.195	440	403	53521

Table 5.2: Elastic and plastic strain components and cyclic stress amplitude at half-life for DP 590

Sample Designation	Total strain amplitude, $\frac{\Delta\varepsilon_T}{2}$ (%)	Half-life data			First quarter cycle peak stress (MPa)	Cycles to failure (N_f)
		Plastic strain at half life, $\frac{\Delta\varepsilon_{pl}}{2}$ (%)	Elastic strain at half life, $\frac{\Delta\varepsilon_{el}}{2}$ (%)	Cyclic stress amplitude, $\frac{\Delta\sigma}{2}$ (MPa)		
P-1	1.0	0.7	0.30	502	393	474
P-4	0.5	0.27	0.23	406	324	4917
P-5	0.35	0.16	0.19	373	298	9235
P-2	0.2	0.04	0.16	304	279	84178
P-3	0.175	0.02	0.155	324	261	123000

Table 5.3: Elastic and plastic strain components and cyclic stress amplitude at half life for DP 980

Sample Designation	Total strain amplitude, $\frac{\Delta\varepsilon_T}{2}$ (%)	Half-life data			First quarter cycle peak stress (MPa)	Cycles to failure (N_f)
		Plastic strain at half life, $\frac{\Delta\varepsilon_{pl}}{2}$ (%)	Elastic strain at half life, $\frac{\Delta\varepsilon_{el}}{2}$ (%)	Cyclic stress amplitude, $\frac{\Delta\sigma}{2}$ (MPa)		
Q-2	1.0	0.56	0.44	822	879	558
Q-3	0.8	0.37	0.43	786	888	1906
Q-5	0.5	0.18	0.32	620	733	2410
Q-4	0.35	0.1	0.25	493	605	61624

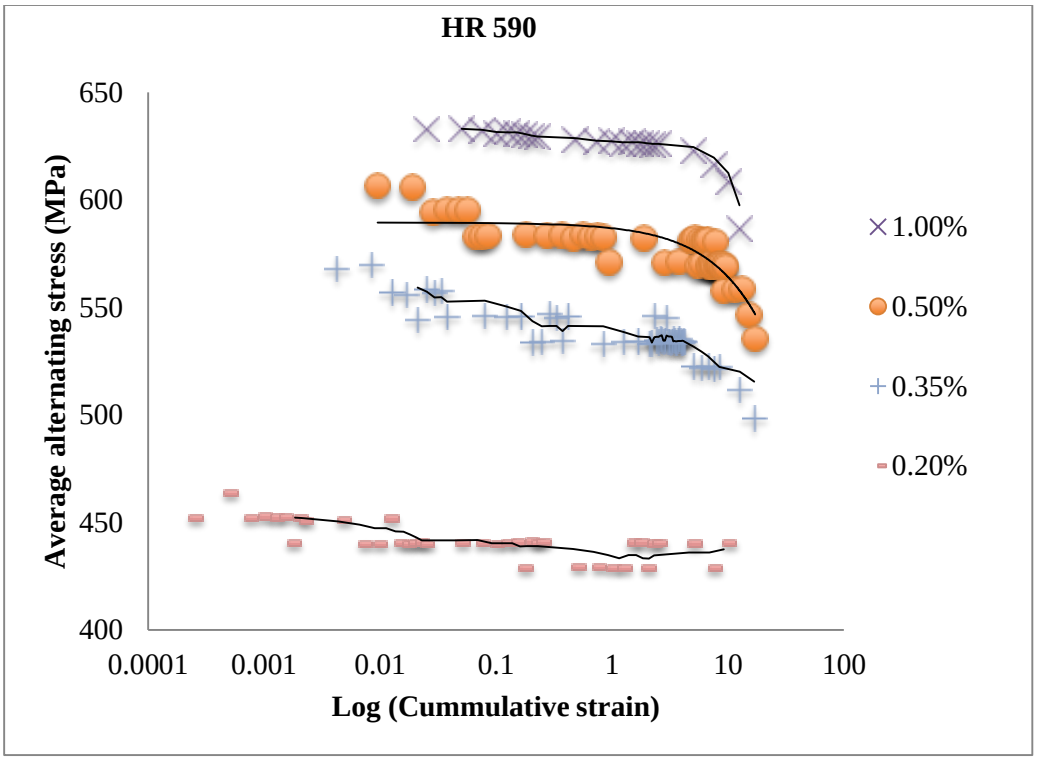
HR 590
650
600
550
500
450
400
Average alternating stress (MPa)
0.0001
0.001
0.01
0.1
1
10
100
Log (Cummulative strain)
1.00%
0.50%
0.35%
0.20%

(a)

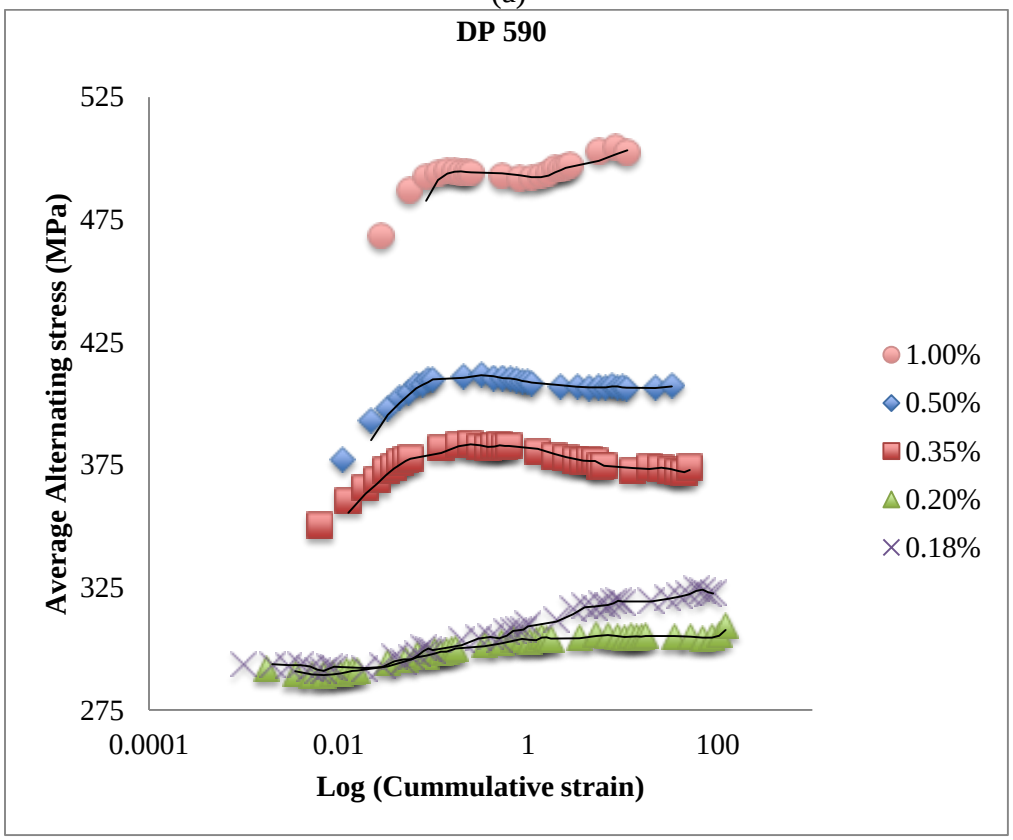
DP 590
525
475
425
375
325
275
Average Alternating stress (MPa)
0.0001
0.01
1
100
Log (Cummulative strain)
1.00%
0.50%
0.35%
0.20%
0.18%

(b)

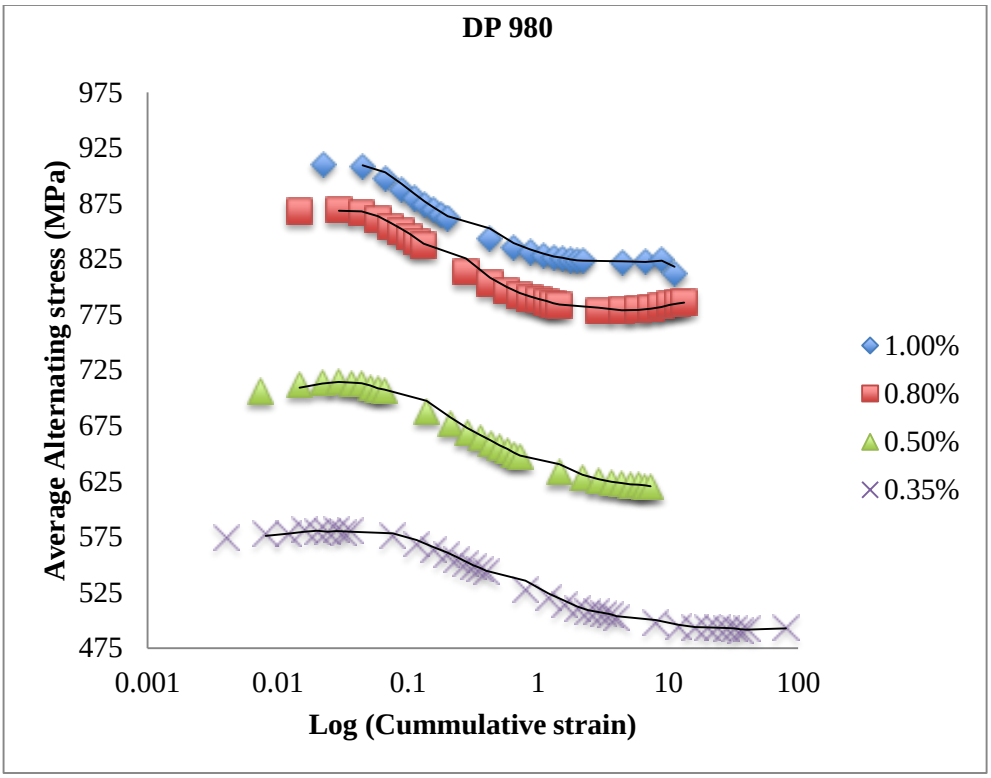

(c)

Figure 5.3: Damage accumulation curves as a function of total accumulated strain amplitude for a) HR 590; b) DP 590; and c) DP 980 steels.

HR 590 specimens showed softening at all strain amplitudes. This rate of softening was gradual at high strain-amplitude (1.0%) and increased in the mid-level strain amplitudes (0.35% and 0.5%) before becoming gradual again at the low strain amplitude (0.2%). This trend has been reported in other studies as well [157]. At the lowest strain amplitudes tested, the average cyclic stress is below the reported yield stress for the steel. (σ_y = 568 MPa for HR 590); however microyielding may still occur locally in a few ferrite grains. This plastic activity in a few grains is expected to be balanced to some extent by the mainly elastic strain displacements in the other grains, leading to a gradual decrease in the average alternating stresses as a function of number of cycles. For comparatively higher strain amplitudes $\frac{\Delta\varepsilon_T}{2} > 0.35\%$, there is a spread of dislocation sources in more and more grains [91]. Additionally, the applied stress amplitude is near

the yield strength of the material, causing dislocations to get unpinned from the precipitates. These two factors together result in an increased rate of softening of the steel as a function of the number of cycles. As the strain amplitude is increased further, some grains may show formation of dislocation substructures leading to formation of PSBs. Other grains show no visible dislocation substructure formation. With increased cycling, the dislocation substructure is expected to accommodate the higher strains while the spread of dislocation sources to newer locations over larger volumes and the unpinning of dislocations from precipitates may continue leading to gradual overall softening [161].

The DP 590 steel specimens showed varying degrees of initial work hardening followed by a plateau–like region. The work hardening could be a result of an increase in the dislocation density resulting from plastic deformation. For DP 590 steels, the plastic deformation in the ferrite phase is expected to occur at a different rate than the surrounding martensite phase leading to strain incompatibility at the interface boundary. This plastic deformation may result in the development of dense dislocation substructures within the ferrite grains and close to the interface boundaries leading to the initial work hardening [45]. These substructures often tend to accommodate further plastic strains caused due to continued cycling, thereby leading to a plateau in the damage accumulation curves (Figure 5.3 (b)) [161]. The low strain amplitudes exhibit almost continuous hardening over the entire life, possibly due to continuous development of dislocation substructures throughout life. Similar observations have also been made by Zhongguang et al. [56].

In response to cyclic loading, DP 980 steels followed similar trends at all strain amplitudes. This comprised of an initial plateau region, followed by softening until

another plateau region is reached leading to final failure as shown in Figure 5.3(c). On application of loading, dislocation rearrangement of the existing dislocations into lower energy configurations can lead to softening. At high strain amplitudes this phenomenon can balance out any hardening caused due to the formation of new dislocations leading to a plateau in the damage accumulation curves. Towards the end of the plateau, dislocation rearrangement may start to dominate causing softening. This mechanism also explains the delay in the onset of the softening region for low strain amplitudes.

Unlike DP 590, the initial hardening is generally absent in the damage accumulation curve for DP 980. This can be because of the larger residual stresses present in DP 980 due to a relatively higher amount of martensite. Zhongguang et al [56, 101] have also reported that fatigue response in dual phase steels can also vary with the martensite content of the steels. According to the authors, the softening observed at all strain amplitudes in DP 980 (as opposed to initial work hardening and gradual softening in DP 590) can be due to the increased strain-compatibility of the lower carbon martensite with the neighboring ferrite grains.

In order to compare the behavior of all three steels, normalized damage accumulation curves at 1.0% total strain amplitude for the three steels have been plotted in Figure 5.4. These curves represent the mechanical response to fatigue loading for the three steels as a function of the number of fatigue cycles. It can be observed that the three steels vary significantly in their mechanical response to fatigue loading and that the cyclic stress response is a complex phenomenon depending both on the underlying microstructure as well as applied strain amplitude. The DP 590 steel showed initial hardening till about 5 cycles followed by the saturation of the average absolute cyclic

stress up to about 200 cycles. This was followed by further hardening leading to final failure. The initial hardening can be attributed to increased dislocation density, particularly in the ferrite grains as well as the presence of hard martensite acting as obstacle against the free movement of dislocations. Additionally, these steels have negligible presence of precipitates; therefore dislocation mobility in ferrite is expected to be restricted only by the orientation of the slip planes with the loading direction. This leads to formation of dislocation substructures at the ferrite-martensite interface that become less dense away from the ferrite-martensite interface [101]. These substructures result in the hardening of the ferrite during cyclic loading, especially in the first few cycles. The saturation of the curve within the plateau region can be explained by the formation of PSBs and localization of accumulated strain within the PSBs. This can lead to no further hardening of the material as all the strains are accommodated both by the formation of new PSB colonies and by the increased dislocation activity within the existing PSBs. Towards the end of the plateau region, the PSB wall structure cannot further accommodate all the strain as explained earlier in Chapter 4. This can lead to the formation of dislocation cells that lead to further hardening of the material till failure. It is interesting that this behavior is very similar to the behavior of the FCC single crystals as shown by Mughrabi et al [16, 25, 150]. These phenomena have been discussed in more detail in section 2.2.2(B).

As opposed to the behavior of DP 590, both HR 590 as well as DP 980 steels showed varying degrees of softening. In the case of HR 590, the softening was gradual and can be attributed to the formation and spreading of dislocation sources along the gage length along with the strain localization within the PSBs. The dislocation motion,

however, is restricted because of the precipitates that pin the dislocations until enough strain energy is provided by the applied load to move the dislocation past the precipitate. This unpinning of dislocations from the precipitates also contributes to the softening. The rapid softening towards the end can be attributed to a change in the cross-sectional area as well as the reduction in the load bearing capacity of the steel primarily due to the formation of microcracks (ref. section 2.2.2 (A)).

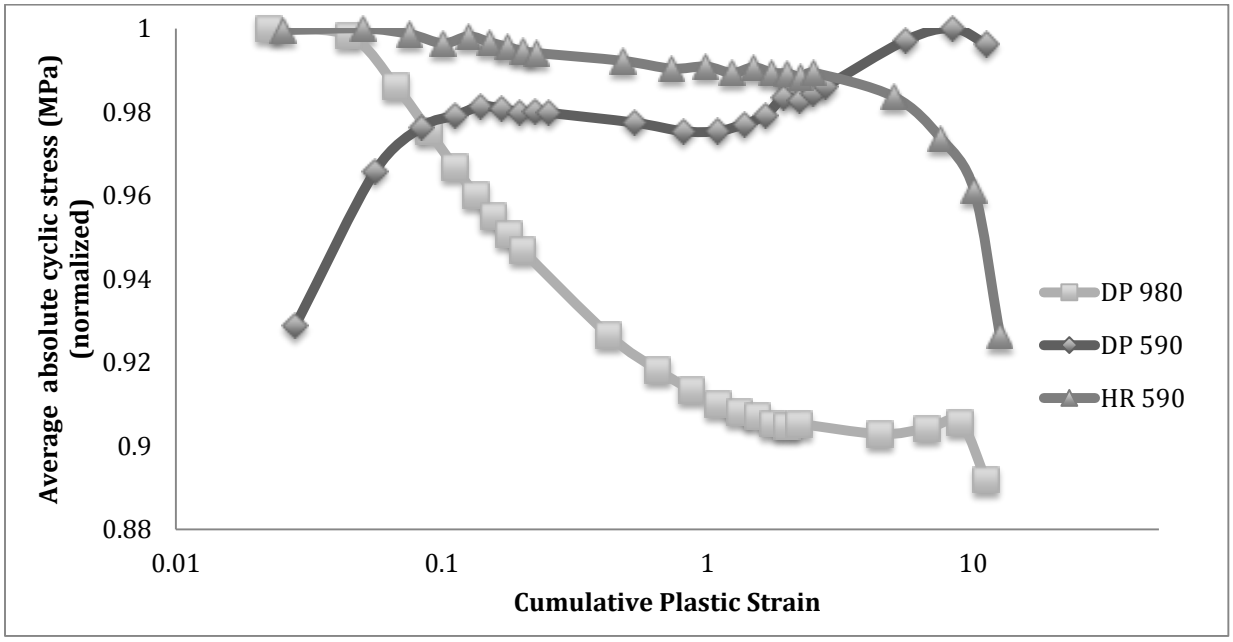

Figure 5.4: Damage accumulation curves (normalized) for DP 590, HR 590 and DP 980 steels fatigued at 1.0% total strain amplitude.

In the case of DP 980 steels, the rapid initial softening can be due to a combination of the formation and spread of new dislocation sources as well as the presence of relatively softer martensite (as compared to the martensite in DP 590 steel) that can also undergo plastic deformation and/or dislocation rearrangements of the statistically stored dislocations formed during the steel processing. The higher strain compatibility between the two phases in DP steels containing higher amount of martensite has already been discussed in detail in section 2.2.2. (B). This strain compatibility can also result in

softening of the DP 980 steel during cyclic loading. This softening continues till about 80 cycles after which a plateau region is observed within which most of the dislocation activity is restricted within the PSBs.

5.2.2.3 Cyclic stress-strain response

The monotonic and cyclic stress v/s plastic strain response for the three steels of interest are shown in Figure 5.5 (a) – (c). The cyclic data have been taken at half-life on polished samples with geometry described in Chapter 4. The monotonic data have been obtained on unpolished standard JIS samples with the inherent assumption that the polishing of samples does not have any substantial effect on the monotonic properties of the steels. The values for the stresses are the maximum (tension) stress values observed at half-life and the values for strain correspond to those maximum stress values. The plastic strains for the monotonic curve are calculated using the modulus of elasticity, E (i.e. $\varepsilon_p = \varepsilon_T - \sigma/E$).

The cyclic response of HR 590 shows cyclic hardening at all strain amplitudes as shown in Figure 5.5 (a). Keeping in mind that at half-life, the ferrite microstructure has already accumulated some damage, this hardening in the cyclic stress- plastic strain curve can be attributed to the dislocation interactions due to accumulated damage that result in hardening of the ferrite. Comparison with the data available in literature, it is observed that the stress-strain response for HSLA steels can vary significantly depending on microstructural parameters. For example Lester [45], Mitchell [162] and Kim and Fine [7] have reported mixed behavior with cyclic softening at the low strain amplitudes and cyclic hardening at the high strain amplitudes.

The cyclic stress-plastic strain behavior of the DP steels is quite different. The microstructural morphology has been shown to impact the stress response of dual phase steels [163]. Martensite in DP 980 is a contiguous phase and this allows the martensite to accommodate more strain resulting in larger extent of softening in these steels. Similar observations of softening when martensite is the connected phase have also been reported

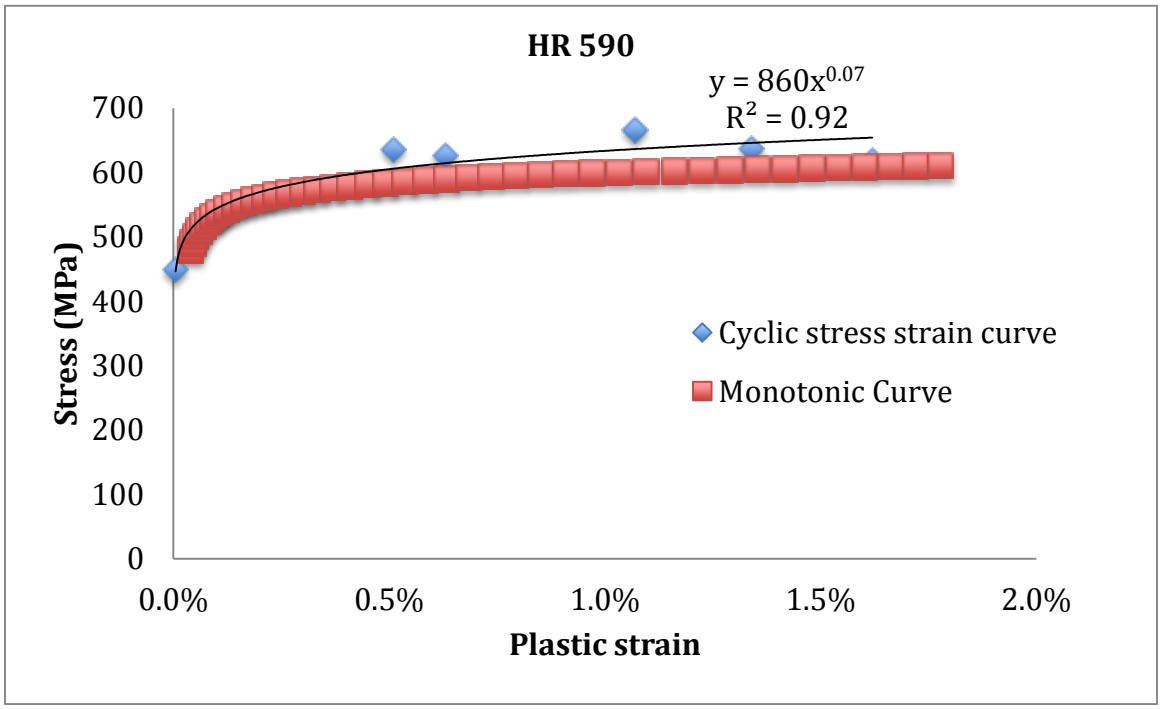

(a)

Figure 5.5: Cyclic and monotonic stress-plastic strain data for a) HR 590 steel; b) DP 590 steel; and c) DP 980 steel at half-life.

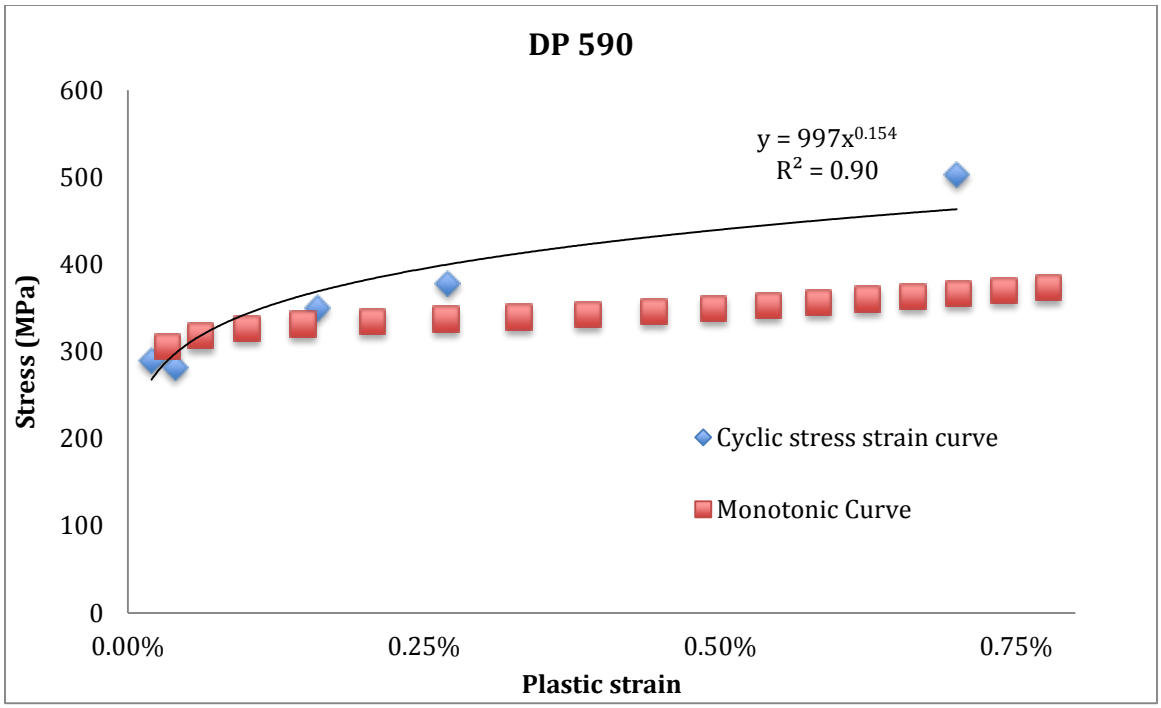

(b)

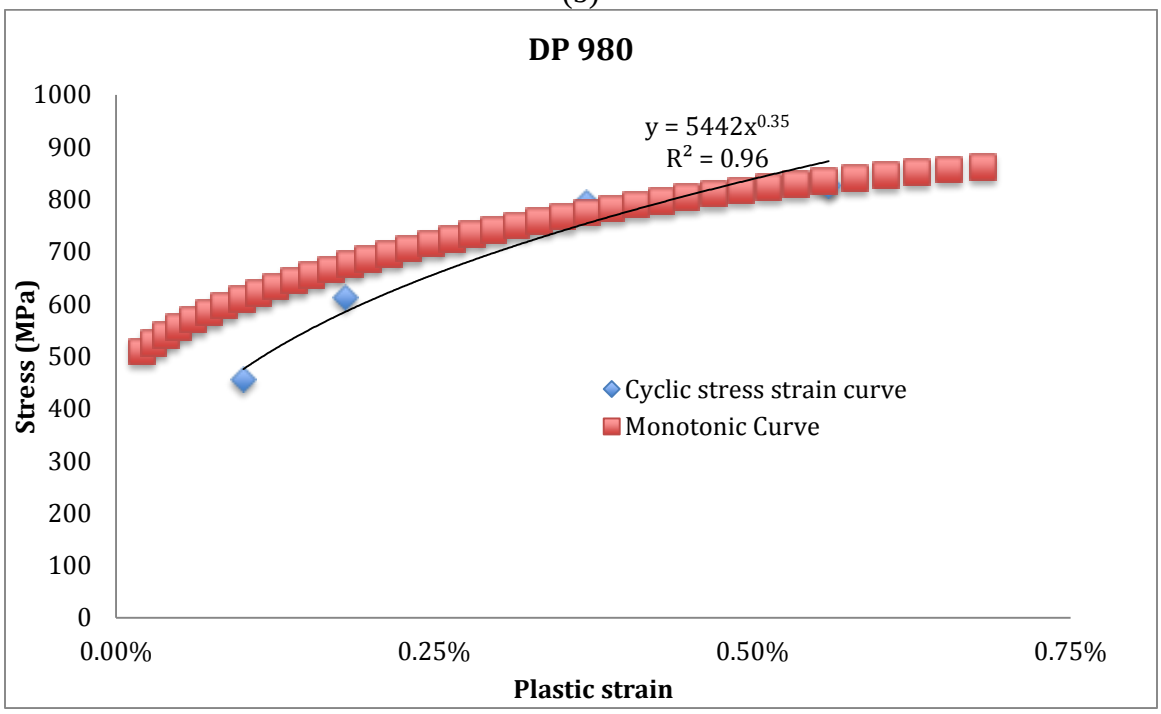

(c)

(Figure 5.5 continued)

elsewhere [163], [4]. DP 590 steel shows a substantial amount of cyclic hardening at all strain amplitudes. Similar observations have been made by Wilson [73]. However, due to the relatively low concentration of carbon in the martensite of DP 980, this phenomenon is more subdued. Instead, in DP 980, the cyclic softening may occur due to a more uniform distribution of dislocations and rearrangement of dislocation substructure in cells leading to cyclic softening [160]. It should be noted that the trends shown in Figure 5.5 are only indicative and it is recognized that more data points would be needed in order to draw any firm conclusions.

5.2.3 *Strain-life behavior*

The strain-life curves for polished specimens of cold rolled dual phase 590 steel, cold rolled dual phase 980 steel and hot rolled HR 590 steel are plotted in Fig. 5.6 (a). This figure shows that the total life of all 3 steels was very similar at all strain levels such that their strain life curves were almost overlapping. This indicated the total life of these steels at any strain amplitude level was independent of the microstructure. However, it should be noted that total fatigue life of a material can be divided into two components; a) life spent prior to crack initiation and b) life spent during crack propagation up to final failure. Even though different materials can show similar total-life behavior, the relative contributions of these two components of life can vary significantly. The variation in the plastic strain contribution for the three steels is shown in Figure 5.6 (b). Thus the strain-life data alone does not give an accurate description of the role played by microstructure in determining the damage evolution prior to crack initiation. It should be noted that in spite of the similarity in the strain-life behavior, the mechanical response of the three steels to cyclic loading varies significantly as discussed in section 5.2.2.2 and 5.2.2.3.

This variation caused difference in the distribution and accumulation of plastic strain in the three steels and can cause significant variations in the evolution of fatigue damage (especially PSB formation and development).

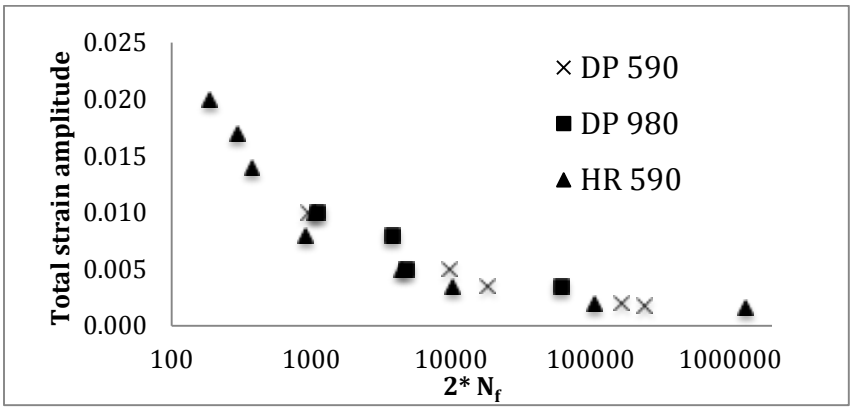

(a)

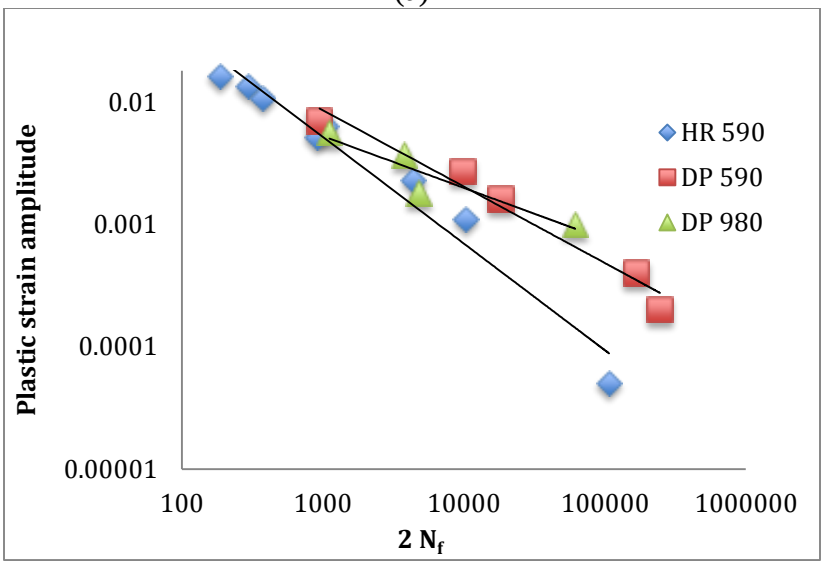

(b)

Figure 5.6: a) Strain life curve (2*N_f = Number of cyclic reversals) and b) $\frac{\Delta\varepsilon_p}{2}$ v/s $2N_f$

5.3 Microstructure characterization

Representative SEM micrographs of etched bulk microstructures of the three steels observed in metallographic planes containing rolling and transverse directions are given in Figure 5.7. As expected, the microstructure of HR 590 steel (Figure 5.7 (a)) consists of ferrite grains with finely dispersed carbides on the grain boundaries as well as

in the grain interiors. Microstructures of DP 590 and DP 980 steels contain ferrite as well as tempered martensite constituents. However, the relative amount of tempered martensite is substantially higher in the DP 980 steel (Figure 5.7 (c)) as compared to DP 590 steel (Figure 5.7(b)). Ferrite is the topologically connected microstructural constituent in the DP 590 steel and tempered martensite is present as islands dispersed in the ferrite matrix. Observe that most of the tempered martensite islands are not completely in the interior of the ferrite grains; they appear to be situated on the ferrite grain boundaries. Further, some boundaries between tempered martensite and ferrite have rough (jagged) morphology.

Microstructure of DP 980 steel consists of topologically contiguous tempered martensite constituent containing dispersed islands of ferrite. In contrast to the microstructure of DP 590, the ferrite grain boundaries are not observed in the microstructure of DP 980 steel indicating that, on the average, these ferrite islands are of smaller size than the average grain size of the prior austenite grain structure from which the dual phase structure is formed. Further, the tempered martensite regions in the DP 980 steel exhibit an internal structure, whereas the tempered martensite islands in the DP 590 steel are completely featureless. In addition, in the DP 980 steel microstructure, all the boundaries between tempered martensite and ferrite are smooth as opposed to some rough boundaries observed in the microstructure of DP 590 steel. Clearly, there are substantial differences in the microstructural geometry of the three steels that arise to the differences in the processing conditions and composition. These differences in the microstructural geometry in turn affect the PSB damage evolution in these steels.

Three-dimensional microstructures of the steels have been quantitatively characterized via stereological measurements on systematic uniform random statistical samples of 80-100 SEM microstructural windows/fields at 4000X or 5000X magnification. The details of these sampling and measurement techniques have been given in Chapter 4. Table 5.4 reports volume fraction of ferrite in the three steels. The average ferrite grain size is 4.0 μm in HR 590 steel and it is 13 μm in DP 590 steel. Therefore, on the average, the ferrite grains in the DP 590 steel are about three times coarser than those in the HR 590 steel.

Table 5.4: Volume fraction of ferrite in the three steels

Steel	Ferrite volume fraction (%) within 95% confidence interval
HR 590	~100
DP 980	30 ± 3
DP 590	76 ± 3

In the DP 980 steel, the dominant microstructural constituent is tempered martensite, which contains islands of ferrite. No ferrite grain boundaries are observed in the majority of these ferrite islands. Consequently, average ferrite grain size has not been measured in the DP 980 steel. The length scale of the ferrite islands in the DP 980 steel can be specified by the mean linear intercept through the ferrite islands, which can be stereologically estimated from metallographic plane sections as described in Chapter 4. For the present DP 980 steel, the experimentally estimated ferrite mean linear intercept is equal to 4.0 μm. Therefore, the length scale of ferrite islands in the DP 980 steel is

comparable to the average ferrite grain size in HR 590 steel, and it is much smaller than the ferrite grain size in the DP 590 steel.

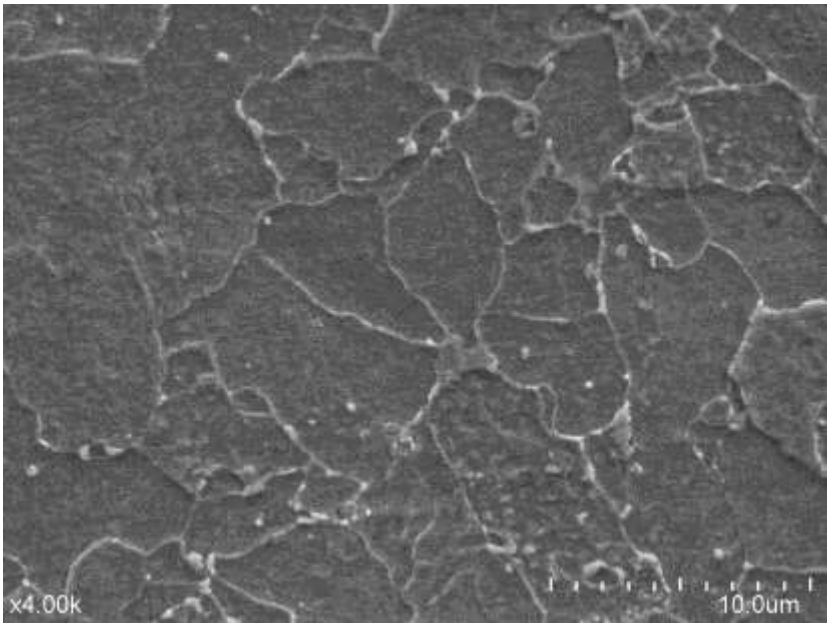

(a)

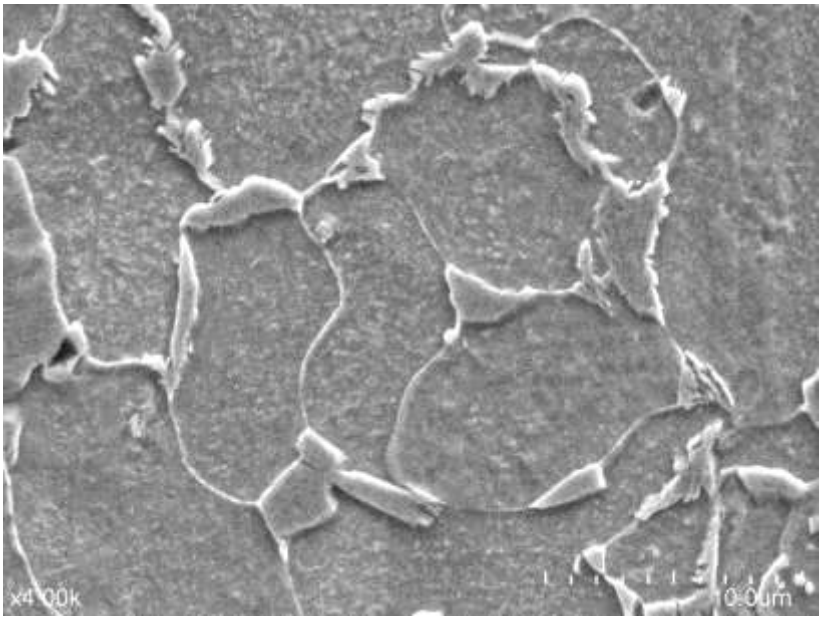

(b)

Figure 5.7: Bulk microstructures for (a) HR 590; (b) DP 590; and (c) DP 980 steels.

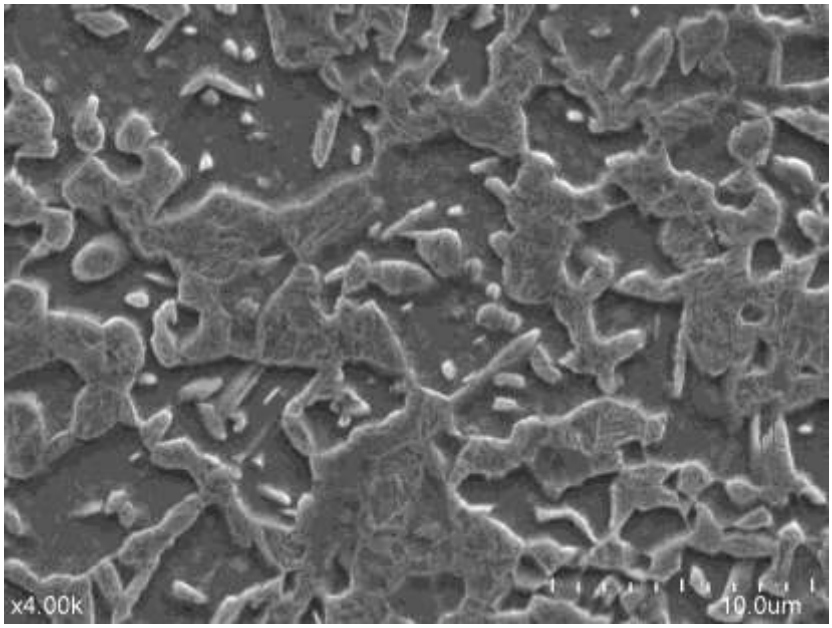

(c)
(Figure 5.7 continued)

5.4 PSB damage evolution

Evolution of PSBs in the three steels of interest has been quantitatively characterized at 1% and 0.2% strain amplitudes as a function of the number of fatigue cycles using *interrupted* fatigue test specimens. To avoid effects of specimen to specimen variations, the PSB evolution as a function of number fatigue cycles has been characterized in the *same specimen* at a given strain amplitude. Early stages of the PSB formation have been studied using atomic force microscopy (AFM), whereas scanning electron microscopy (SEM), digital image processing, and stereology have been utilized for quantitative characterization of evolution of PSBs over the entire fatigue life. AFM observations and data are presented below; the SEM based microstructural data are presented in the subsequent sub-section.

5.4.1 *Atomic Force Microscopy*

Atomic force microscopy has been performed on DP-590 steel specimen fatigued at 1% strain amplitude to determine how early the PSBs begin to form during the fatigue process. Figure 5.8 (a) depicts an AFM image field of view (left) of the fatigue specimen surface at 5 cycles (i.e. ~ 1% of fatigue life at 1% strain amplitude) showing an extrusion indicative of persistent slip marking. Topographic map across the extrusion is shown in Figure 5.8 (b). The height of this particular extrusion calculated from the topographic data in Figure 5.8 (b) is 90 nm. This AFM observation demonstrates that the extrusions at the fatigue specimen surface begin to form in very early stages (in this case, 5 cycles) of the damage evolution process.

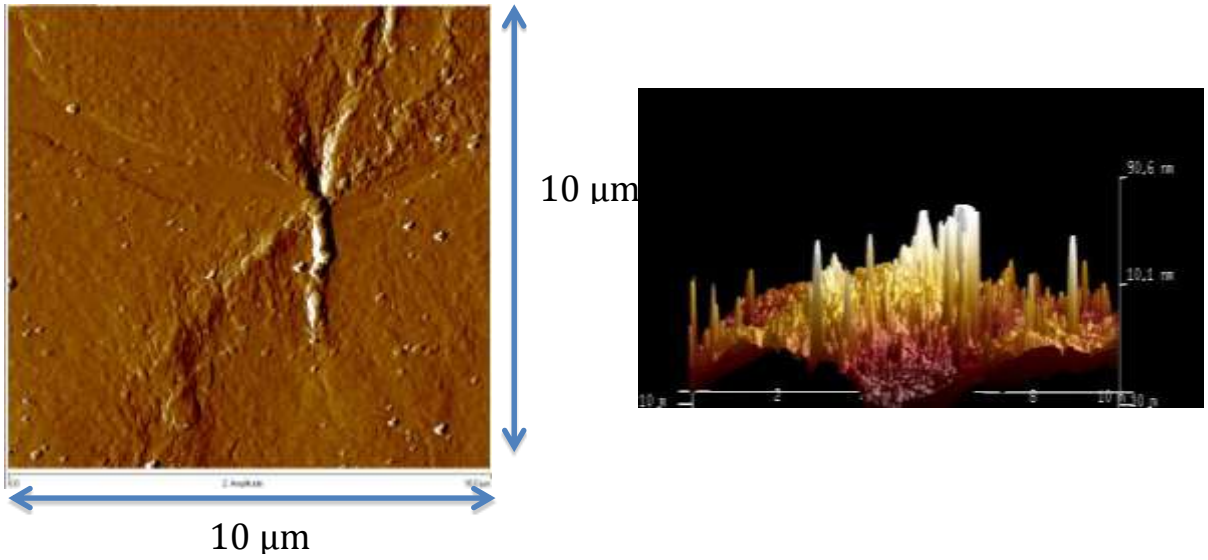

Figure 5.8: (a) AFM image of an individual extrusion formed at 5 cycles of fatigue in Cold Rolled DP 590 steel fatigued at 1% strain amplitude and (b) topographic map across the extrusion.

Nonetheless, as will be shown later, the first fully developed PSB colonies present in the tempered martensite islands dispersed in ferrite. This observation has been confirmed

through subsequent SEM observations reported in the next section. Figure 5.9 (b) shows high resolution view of some persistent slip markings/extrusions from a PSB colony in

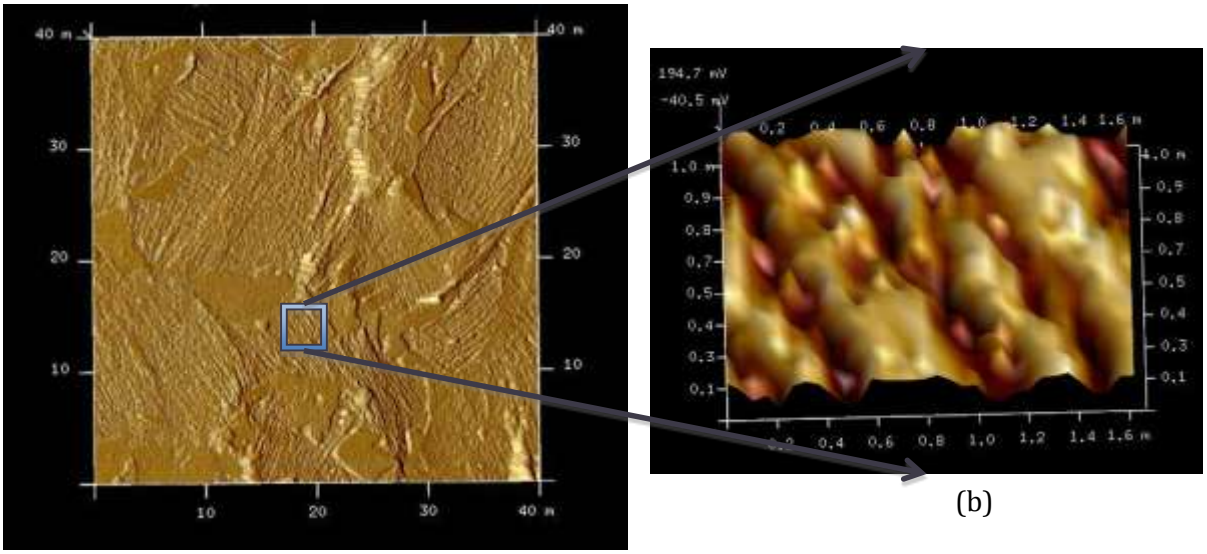

(a) (b)

Figure 5.9: (a) AFM image of a field of view in a DP 590 specimen fatigued at ε_T = 1.0% for 30 cycles depicting colonies of PSBs and (b) higher resolution view illustrating the topography of the extrusions.

Figure 5.9 (a) generated using the topographic information on the XYZ coordinates across the persistent slip marking/extrusion. The height of these particular extrusions shown in the figure is approximately 40 nm, which is different from the one characterized in Figure 5.5 (b). It should be pointed out that the extrusion heights reported here are based on extremely localized measurements of *individual* extrusions and are not statistically averaged values across the sample. At any given point in life, a distribution of extrusion heights is expected to exist. This kind of distribution has been reported by Sestak et al [124] where the authors have reported that the extrusion heights can vary with grain size with extrusions in larger grains generally having more height. Similar observations have also been made by Man et al [31] who have reported the variation of extrusion heights from 200 nm to 300 nm for ferrite grain sizes of ~ 38 µm.

Although AFM is an excellent tool for detection of the initiation of PSB formation in the early cycles of the fatigue life, the image acquisition process in the AFM is extremely slow and it is highly time consuming to acquire images of multiple fields of view (~ 50 to 100) needed for statistically significant quantitative characterization of the PSB damage. Therefore, quantitative characterization of the PSB damage evolution has been performed using scanning electron microscopy of the fatigued specimen surfaces, which is reported in the next section.

5.4.2 *Scanning Electron Microscopy*

SEM-based observations and measurements were performed on at least 80 systematic uniform random fields of view in the central one-third region of the fatigue specimen gauge length. Qualitative microstructural observations, and similarities and differences in the PSB damage evolution in the three AHSS steels are given below; quantitative PSB damage evolution data and analysis are presented in the next section.

5.4.2.1 DP 590 steel

Figures 5.10 (a) – (e) show the growth in the PSB colonies for DP 590 steel as a function of strain amplitude. As expected, the area fraction of PSB colonies tends to increase with an increase in the accumulated plastic strain due to continued cycling. Figures 5.11 (a) – (d) gives representative SEM micrographs of DP 590 steel specimen fatigued at 1% strain amplitude to illustrate important features of the PSB damage evolution. Figure 5.11 (a) illustrates that fully developed PSB colonies are present at 15 cycles (~ 3% of fatigue life at 1% strain amplitude), and Figures 5.11 (b) and (c) illustrate PSB colonies in the failed fatigue specimen (526 cycles at 1% strain amplitude). Figure 5.11 (d) represents the failed DP 590 specimen at 0.2% strain amplitude. Figure 5.11 (e)

shows a crack next to a PSB the sample fatigued at 0.2% total strain amplitude after 80,000 cycles. Lastly Figure 5.11(f) shows a macroscopic crack in the same sample at failure passing through a PSB-dense region.

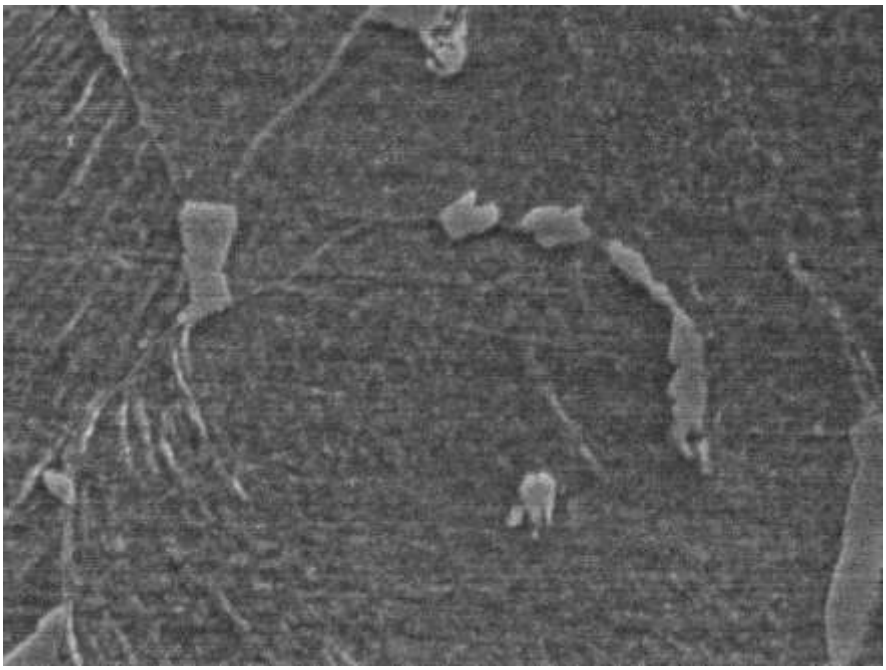

(a)

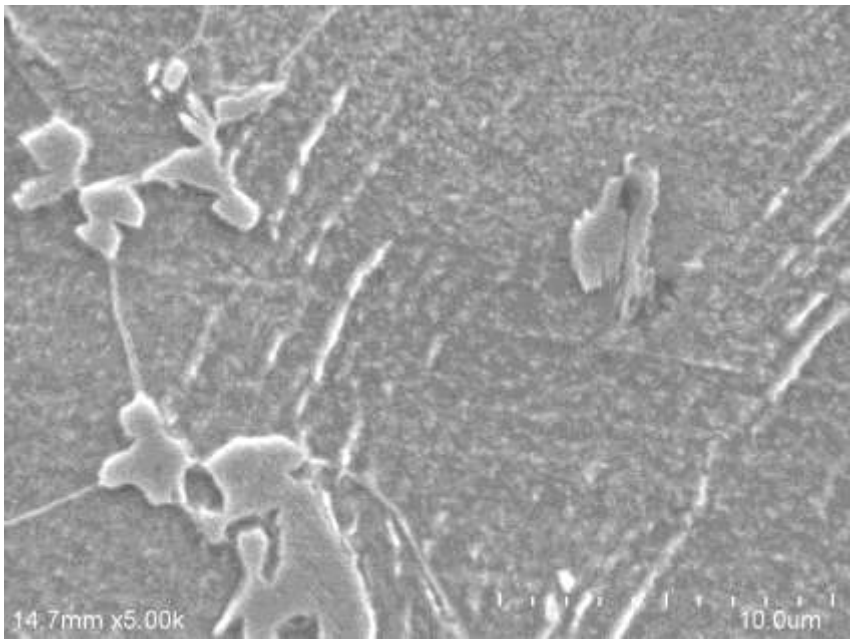

(b)

Figure 5.10: SEM images showing the growth of PSB colonies as a function of cycles for the interrupted test specimen for DP 590 steel at 1.0% strain amplitude. The images taken at a) 15 cycles, b) 20 cycles, c) 50 cycles, d) 200 cyles and e) 526 cycles (failure).

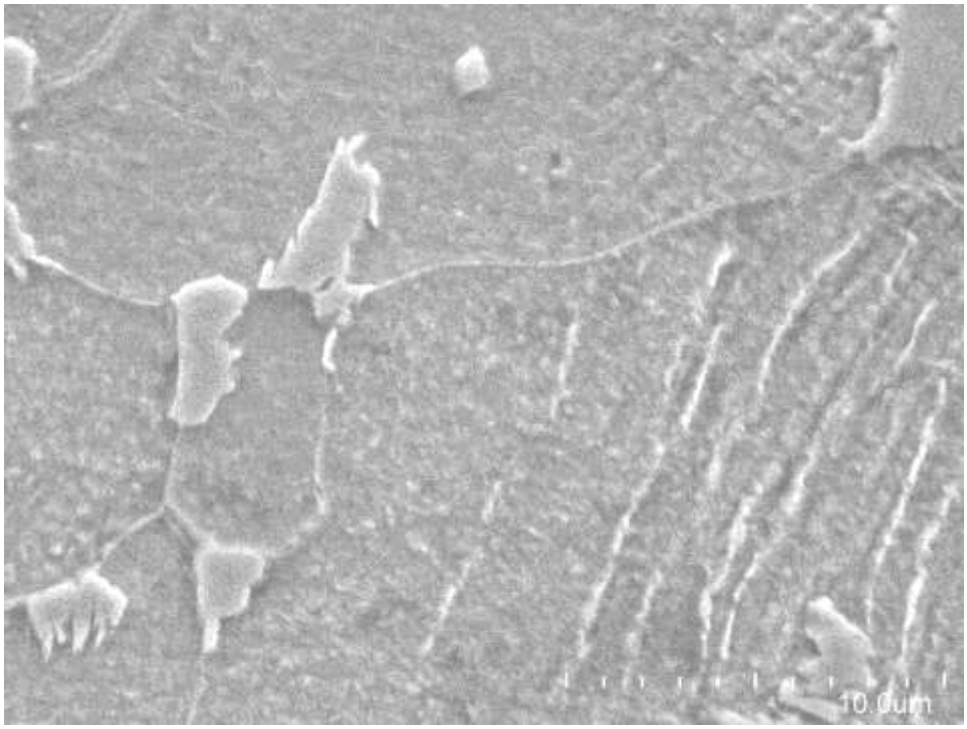

(c)

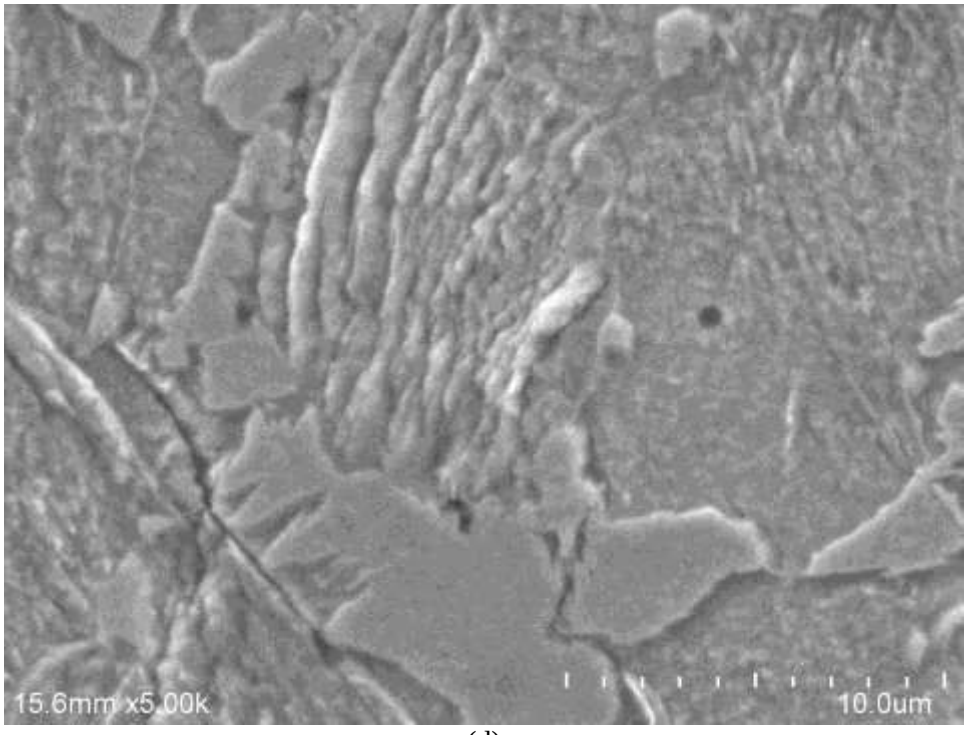

(d)

(Figure 5.10 continued)

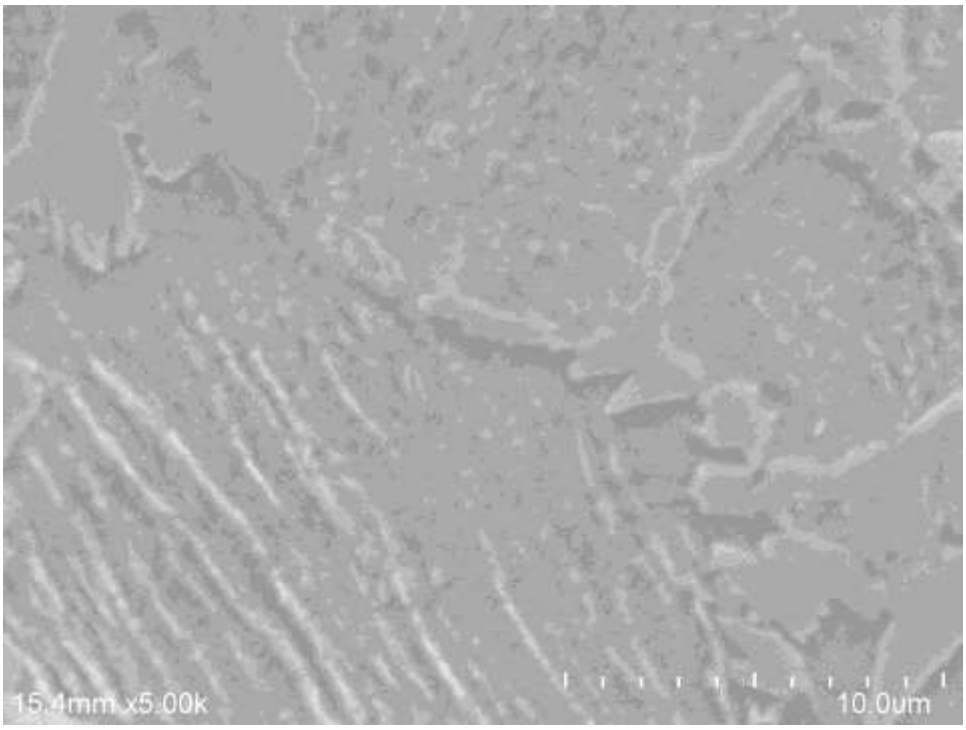

(e)

(Figure 5.10 continued)

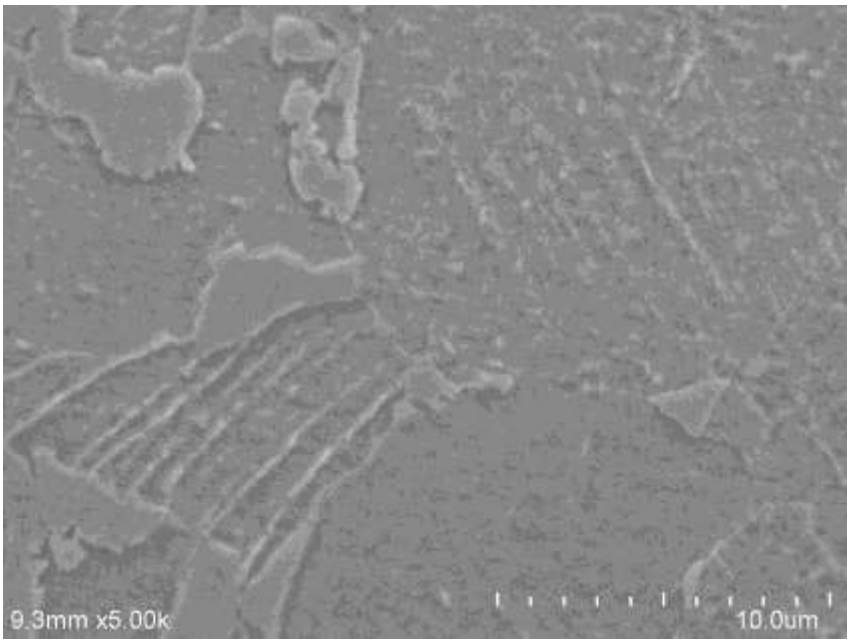

(a)

Figure 5.11: Reperesentative SEM fields of view of the DP-590 steel specimen fatigued at 1% strain amplitude, (a) 15 cycles, (b) 526 cycles (failure), (c) failed specimen at lower magnification, (d) failed sample at lower strain amplitude (0.2%), (e) crack nucleation along a PSB at 80,000 cycles (0.2%), and (f) crack propagation along PSB rich region in failed sample at 0.2% (~120,000 cycles).

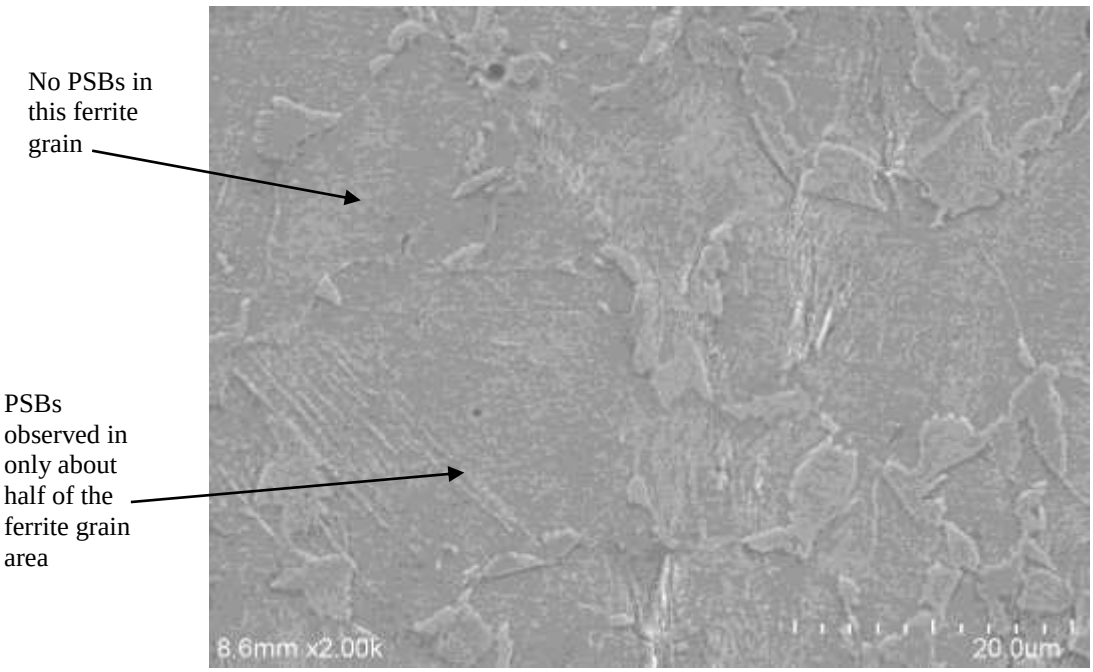

(b)

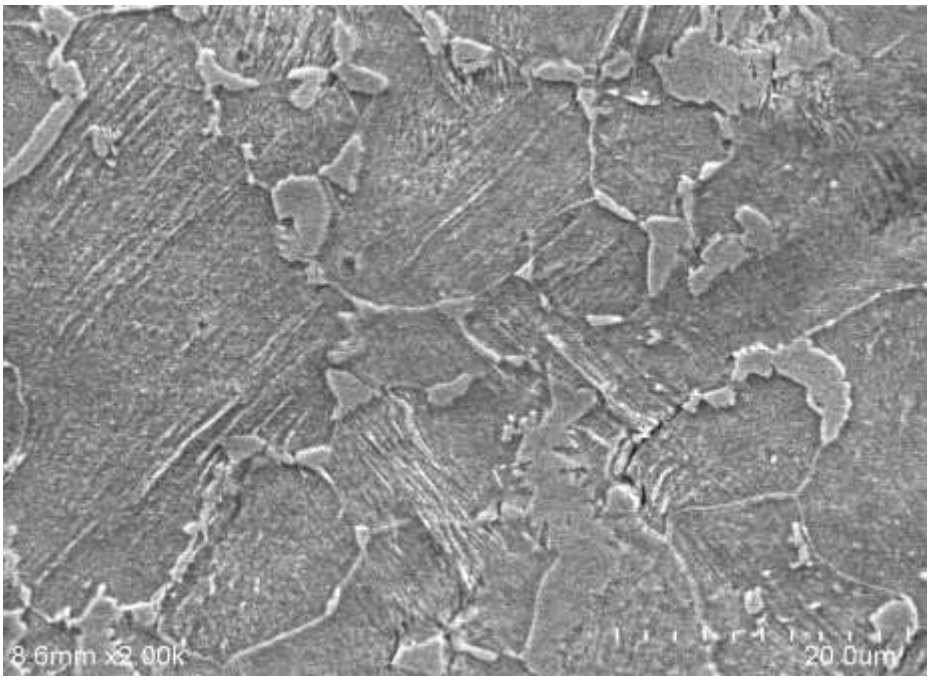

(c)

(Figure 5.11 continued)

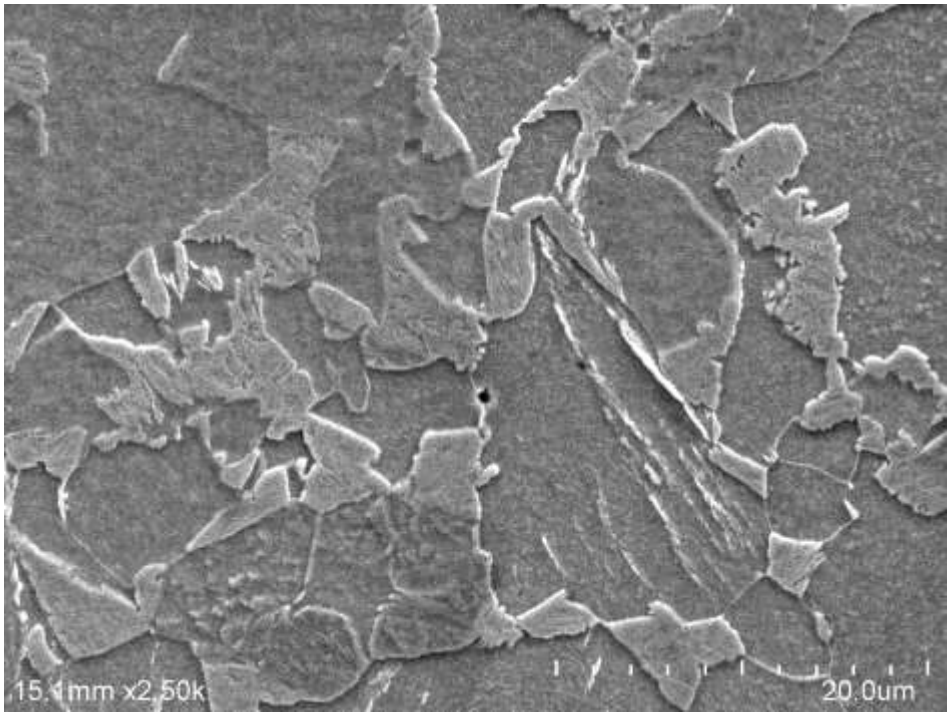

(d)

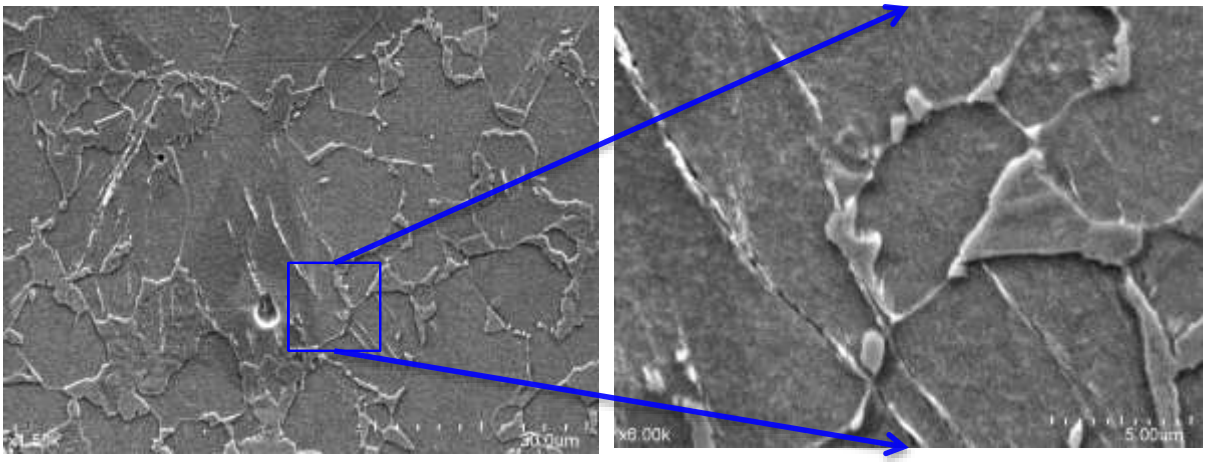

(e)

(Figure 5.11 continued)

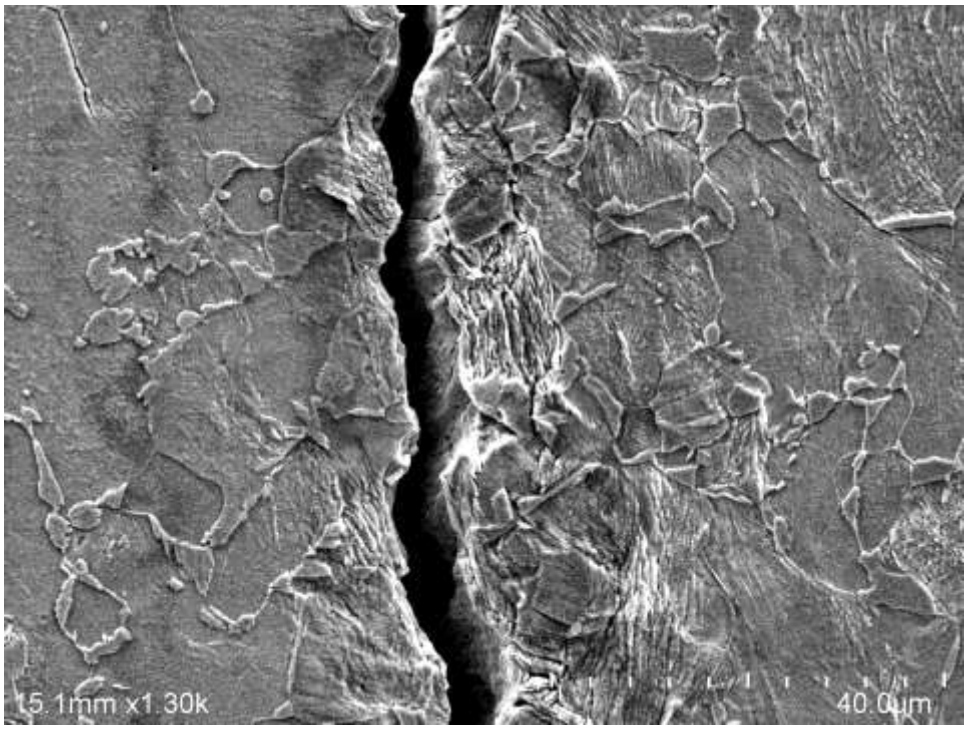

(f)

(Figure 5.11 continued)

1. PSB colonies are observed in some ferrite grains but not in any tempered martensite regions in the DP 590 steel even in the failed specimen.
2. Even at failure, PSB colonies are not present in every ferrite grain, and when a PSB colony is present in a ferrite grain, it may or may not completely cover that ferrite grain (ref. Figure 5.11 (b)). Further, some ferrite grains contain more than one PSB colony. This is also observed in HR 590 and DP 980 steels.
3. In general, a PSB colony does not cross the grain boundaries of the ferrite grain in which it is formed. Consequently, the maximum possible size of a PSB colony is limited by the size of the ferrite grain in which it is formed. This is observed in all three AHSS steels studied.
4. Majority of the PSBs appear to be oriented at 45 degrees with the loading direction (X-direction) in the two-dimensional section, but PSB colonies at other

angular orientations are also present. Therefore, there is a distribution of angular orientations of the PSBs. This is also observed in HR 590 and DP 980 steels.

5. Number density and area fraction of the PSB colonies increases with the increase in number of fatigue cycles and strain amplitude. This is observed in all three steels studied.
6. Compared to the sample fatigued at 1.0% strain amplitude, the PSB related activity is much lower in the DP 590 specimen fatigued at 0.2% strain amplitude as represented by a comparison of Figures 5.11 (b) and (c).
7. PSBs are often a site for nucleation of a fatigue crack. Figure 5.11(e) shows a microcrack formed along a PSB within a ferrite grain for DP 590 specimen fatigued at 0.2% strain amplitude for 80,000 cycles.
8. The crack propagation is also favored along a PSB rich region as shown in Figure 5.11 (f) depicting the path taken by a macrocrack in the failed sample at 0.2% strain amplitude. It can be observed that the crack follows a path along a region having high density of PSB colonies.

5.4.2.2 HR 590 steel

Figure 5.12 gives representative SEM micrographs of HR 590 steel specimen fatigued at 1% strain amplitude to illustrate important features of the damage evolution. Unlike DP 590 steel, where the PSB colony formation is observed at 15 cycles (~ 3% of fatigue life at 1% strain amplitude), in the HR 590 steel, the fully developed PSB colonies are observed only from 100 fatigue cycles and onwards (Figure 5.12 (a)), i.e., at about 20% of the fatigue life or higher at 1% strain amplitude. Thus, nucleation of PSB starts much later in the largely ferritic HR 590 steel as compared to that in the dual phase

DP 590 steel, although the total fatigue life of the two steels is comparable at 1% strain amplitude. This is an important effect of microstructure on the initiation of the PSB damage. The dual phase microstructure of DP 590 steel contains 25% tempered martensite and 75% ferrite, whereas microstructure of HR 590 does not contain any tempered martensite. The tempered martensite constituent in the DP 590 steel has substantially high C content (~ 0.4 wt.%) as ferrite contains almost zero C, although overall C content of DP-590 steel is comparable to that of HR-590 steel (~ 0.1%). Consequently, the tempered martensite in DP-590 steel has a high yield stress ~2 GPa [164] and thus higher resistance to plastic deformation. As a result, the accumulated plastic fatigue strain in DP-590 steel mostly resides in the ferrite constituent.

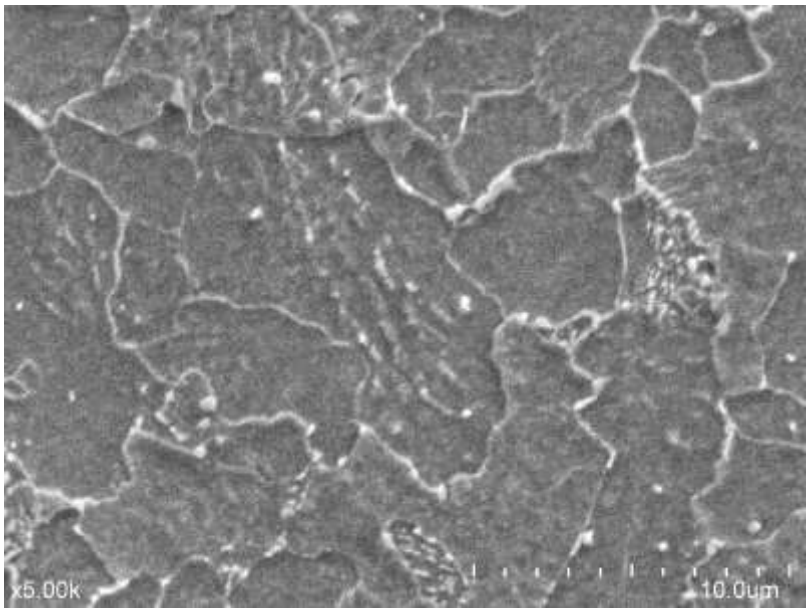

(a)

Figure 5.12: Reperesentative SEM fields of view of the HR-590 steel specimen fatigues at 1% straim amplitude, (a) 100 cycles, (b) 518 cycles (at failure).

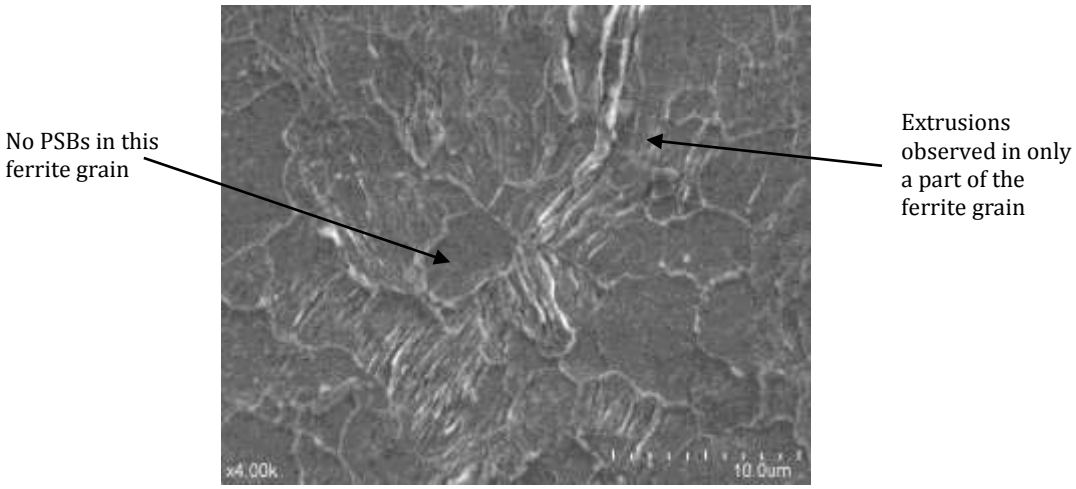

(b)

(Figure 5.12 continued)

The higher extent of the plastic strain in the ferrite constituent in DP-590 steel facilitates initiation of the PSB formation at very early stages.

5.4.2.3 DP 980 steel

Figure 5.13 gives representative SEM micrographs of DP 980 steel specimen fatigued at 1% strain amplitude to illustrate important features of the damage evolution. In the DP-980 steel fatigued at 1% strain amplitude, the PSB colonies have been observed in the specimen only when fatigued for 50 cycles (Figure 5.13 (a)) or more (i.e. more than 10% of fatigue life at 1% strain amplitude). This is in contrast to DP 590 steel, where the PSB colonies have been observed at 15 cycles (~ 3% of fatigue life at 1% strain amplitude), although both

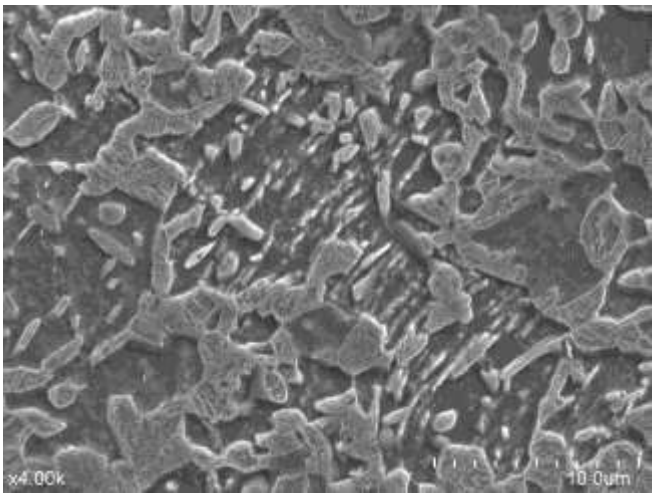

(a)

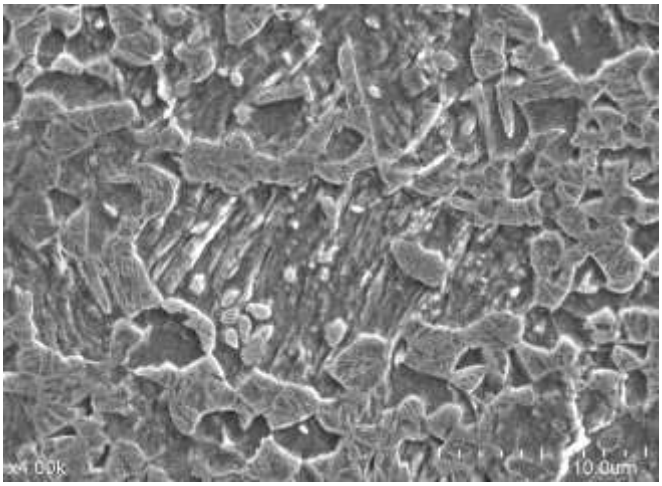

(b)

Figure 5.13: Reperesentative SEM fields of view of the DP 980 steel specimen fatigues at 1% straim amplitude, (a) 50 cycles, (b) 385 cycles (failure).

DP 590 and DP 980 are dual phase steels, i.e., they contain ferrite and tempered martensite. These differences are likely to be due to different carbon contents of martensite in the two dual phase steels. DP 980 and DP 590 steels have comparable total carbon contents (~ 0.1 wt%) but volume fraction of martensite in DP 980 steel is 70%, which is substantially higher than that (25%) in the DP 590 steel. In both steels, ferrite contains almost zero carbon. Therefore, carbon content of martensite in DP 980 steel is

substantially lower (~ 0.14 wt.%) than that of DP 590 steel (~ 0.4 wt.%). Brooks has reported the yield strength of martensite at this carbon composition to be approximately 850 MPa [164]. The compressive flow stress for martensite in a similar dual phase steel has been reported to be between 1 and 1.3 GPa by Chen et al. [165]. Consequently, the tempered martensite in DP 980 steel is significantly softer that in DP 590 steel. It can be said that in DP 980 steel, accumulated plastic fatigue strain resides both in tempered martensite and ferrite in a comparable amounts, especially as the peak global stress levels reached at 1.0% strain amplitude are ~900 MPa. This lack of concentration of plastic strain in ferrite in DP 980 steel (compared to ferrite in DP 590 steel) delays the onset of formation of PSBs in DP 980 steel. It is likely that in the DP 980 steel the PSBs form in ferrite as well as in tempered martensite. However, due to the presence of a sub-structure in the tempered martensite in *undeformed* DP 980 steel (see Figure 5.7 (c)) it is difficult to unambiguously detect and characterize PSBs in the tempered martensite in DP 980 steel using the SEM. Consequently, in the present work, only the PSBs in ferrite are characterized quantitatively.

5.4.3 *Quantitative analysis of PSB damage evolution*

The following geometric parameters have been estimated in the interrupted fatigue test specimens using statistical sampling, image processing, and stereological techniques described in detail in Chapter 4.

1. Volume fraction of PSB colonies in ferrite
2. Total surface area of PSB colonies per unit volume
3. Total surface area of PSB surfaces per unit volume
4. Two- and three-dimensional average size of the PSB colonies

5. Two-dimensional average size of the ferrite grains in which PSB colonies are formed
6. Two- and three-dimensional angular orientation distribution of PSBs in ferrite

These experimental data are presented and analyzed below. The data trends are explained using a simple geometric model for global evolution of PSBs in the three AHSS steels. The model successfully captures the observed microstructural effects on the PSB damage evolution.

5.4.3.1 PSB colony volume fraction

The focus of the present work is on global PSB damage evolution in the ferrite constituent of three AHSS steels, HR 590, DP 590, and DP 980. Relative amount (volume fraction/percentage) of ferrite is significantly different in the microstructures of these three steels: HR 590 steel is almost completely ferritic, DP 590 steel contains 76% ferrite, and DP 980 steel contains 30% ferrite. As a result, global PSB damage evolution is described in terms of normalized parameters corresponding to the experimentally estimated metric global properties of PSBs. *Ferrite normalized* volume fraction of PSB colonies V_f and *ferrite normalized* total surface area of the PSB colonies S_f are defined as follows.

$$V_f = \frac{Volume\ fraction\ of\ PSB\ colonies}{Ferrite\ volume\ fraction} \tag{5.5}$$

$$S_f = \frac{Total\ surface\ area\ of\ PSB\ colonies\ per\ unit\ volume}{Ferrite\ volume\ fraction} \tag{5.6}$$

V_f and S_f are calculated from the experimental data on volume fraction of PSB colonies, total PSB colony surface area per unit volume, and ferrite volume fraction.

Figure 5.14 depicts the plot of ferrite normalized volume fraction of PSB colonies V_f vs. fraction of fatigue life at 1% strain amplitude for the three AHSS steels studied.

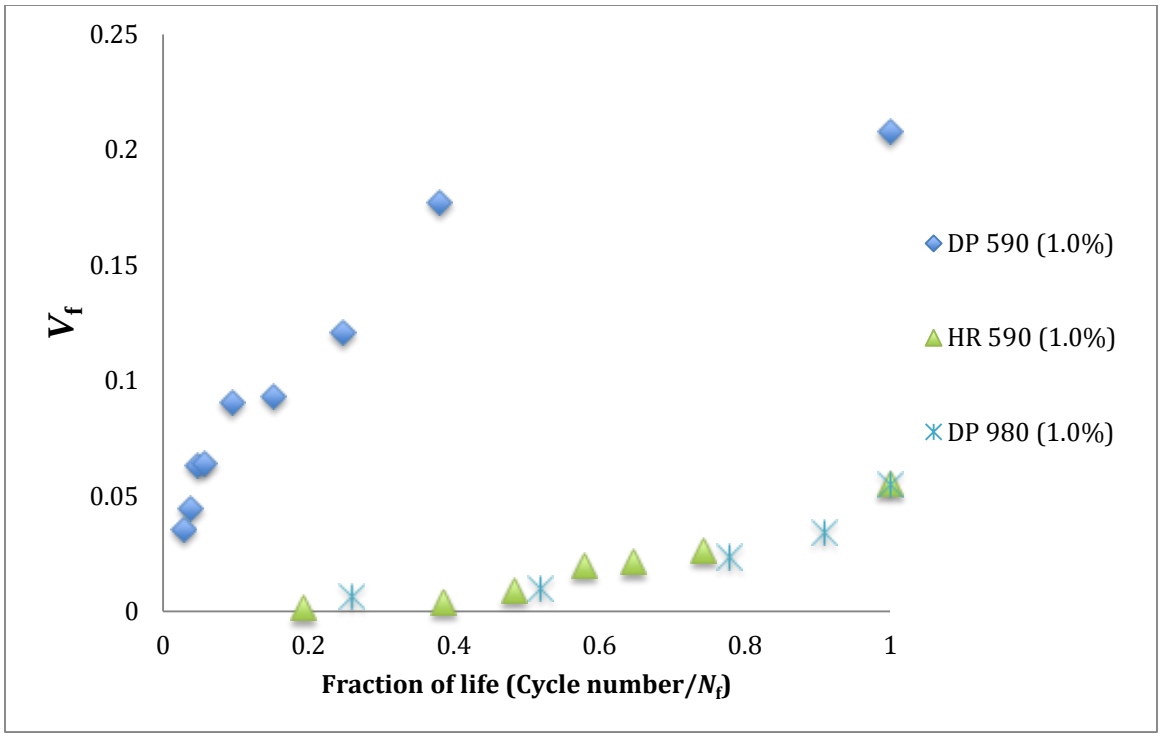

Figure 5.14: Plot of ferrite normalized volume fraction of PSB colonies vs. fraction of fatigue life.

Inspection of the data trends in Figure 5.14 lead to following observation.

1. At any given fraction of fatigue life, the ferrite normalized volume fraction of PSB colonies is substantially higher in DP 590 steel compared to HR 590 and DP 980 steels.

2. Ferrite normalized volume fractions of PSB colonies in HR 590 and DP 980 steels have comparable values at any given fraction of fatigue life, and the data points for these two steels fall on the same trend, whereas the data trend of DP 590 is distinctly different.

3. The rate of change of ferrite normalized volume fraction of PSB colonies with the number of fatigue cycles *decreases* with the increasing number of cycles in DP 590 steel, whereas it *increases* in DP 980 and HR 590 steels.

Figure 5.15 shows a plot of ferrite normalized volume fraction of PSB colonies versus fraction of fatigue life for DP 590 steel at 1% and 0.2% strain amplitudes to

illustrate the effect of strain amplitude on PSB damage evolution. At any given fraction of fatigue life, the ferrite normalized volume fraction of PSB colonies is almost an order of magnitude higher at 1% strain amplitude as compared to 0.2% strain amplitude. In DP 590 steel, at 1% strain amplitude, 63% of accumulated fatigue strain is plastic at half-life, whereas at 0.2% strain amplitude, only about 2.5% of total accumulated fatigue strain is plastic at half-life. Therefore, at 1% strain amplitude the majority of fatigue strain is plastic, whereas at 0.2% strain amplitude it is mostly elastic. Thus, the observed low level of PSB activity at 0.2% strain amplitude is most likely due to the low cyclic plastic strain.

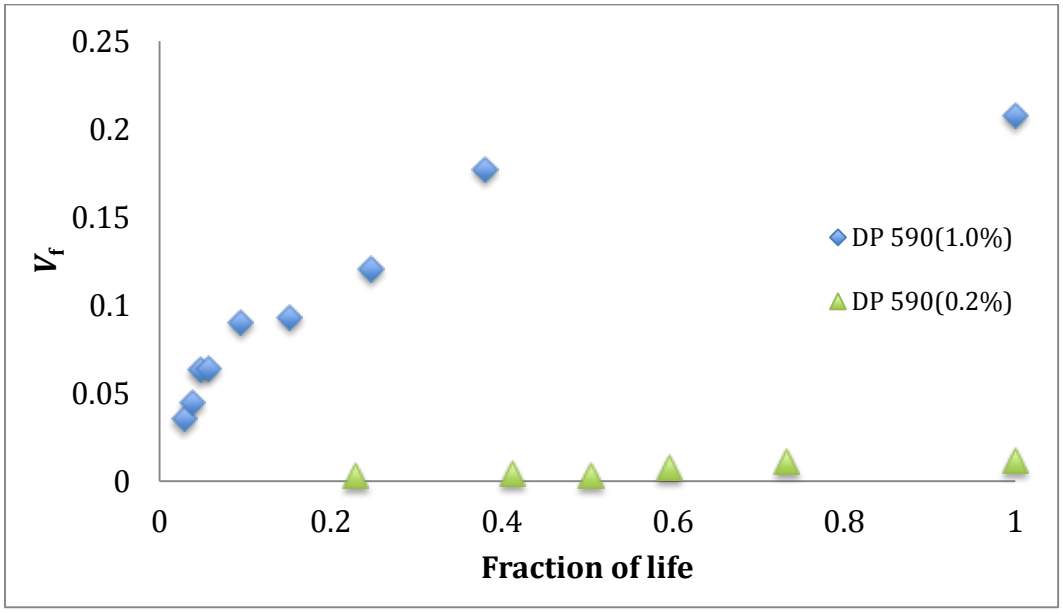

Figure 5.15: Plot of ferrite normalized volume fraction of PSB colonies vs. fraction of fatigue life in DP 590 steel at two different strain amplitudes.

The data trends in Figure 5.14 and 5.15 are nonlinear. In general, an equation with a minimum of three parameters is required to mathematically represent nonlinear trends. Although such nonlinear data trends can be represented by a number of different empirical equations, it is proposed to use a simple three-parameter (minimum required) empirical power-law equation to describe the relationship between ferrite normalized

volume fraction of PSB colonies V_f and number of fatigue cycles n at a fixed strain amplitude given as follows.

$$V_f = A(n - n_0)^{\alpha} \tag{5.7}$$

In equation (5.7), the empirical constant n_0 represents number of fatigue cycles at which the PSB colonies begin to form, and A and α are empirical constants that capture dependence of PSB damage evolution on steel microstructure and strain amplitude. The exact value of n_0 is not known from experimental observations; one can only discern that n_0 is less than or equal to the lowest number of cycles at which the PSB colonies were experimentally observed. Therefore, for each data set, $\ln V_f$ vs. $\ln(n - n_0)$ was plotted for different assumed values of n_0 consistent with the experimental observations till a best-fit straight line was obtained. Table 5.5 gives the values of A, n_0, and α for different data sets obtained in this manner and the plots are given in Figures 5.16 to 5.18.

Table 5.5: Values of parameters A, n_0, and α in Equation 5.7

Parameter	DP 590	HR 590	DP 980
n_0	14	90	90
α	0.3	1.9	1.64
A	3.0 X 10^{-2}	6.0 X 10^{-7}	4.24 X 10^{-7}

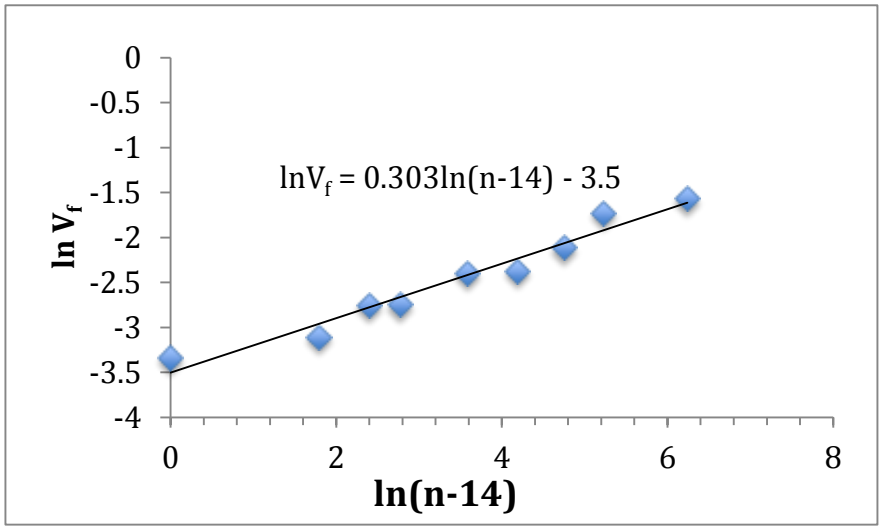

Figure 5.16: Plot of $\ln V_f$ vs. $\ln (n - n_0)$ for DP 590 steel at 1% strain amplitude

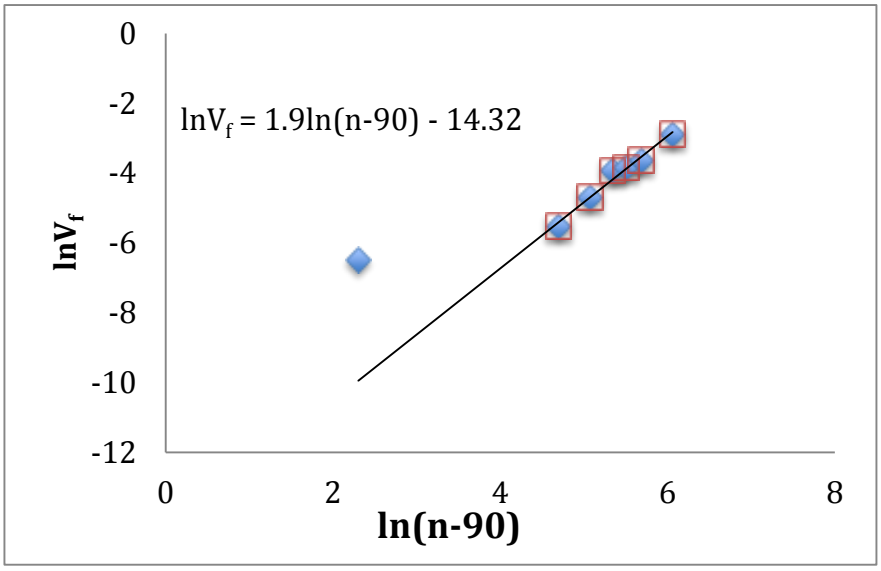

Figure 5.17: Plot of $\ln V_f$ vs. ln $(n - n_0)$ for HR 590 steel at 1% strain amplitude

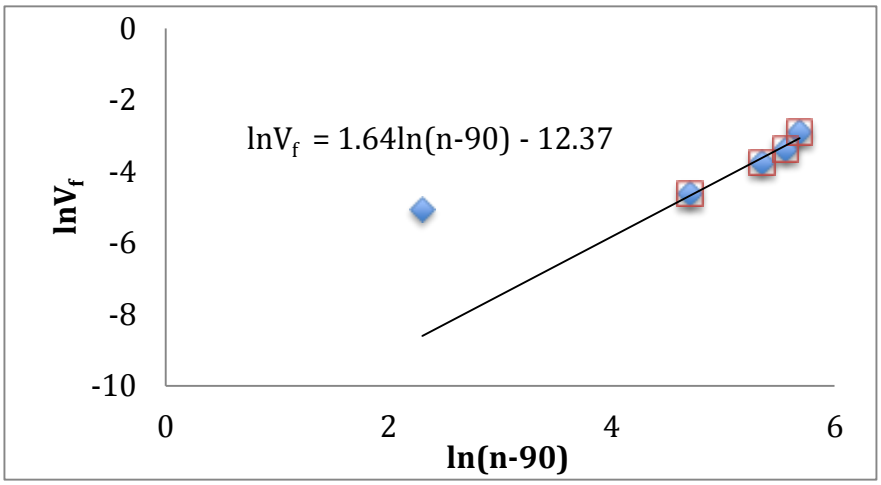

Figure 5.18: Plot of $\ln V_f$ vs. ln $(n - n_0)$ for DP 980 steel at 1% strain amplitude

As shown in Table 5.5, the value of exponent α for DP 590 steel is less than one and it is significantly lower than the α value for HR-590 steel, which is higher than one. Therefore, the rate of change of ferrite normalized volume fraction of PSB colonies decreases with the number of fatigue cycles in DP 590 steel (i.e., the process decelerates), whereas the process accelerates with the number of fatigue cycles in HR 590 steel. This is likely to be due to the presence of martensite of relatively high C content (~ 0.4 wt. %) in the DP 590 steel. Martensite in DP 590 steel has high yield stress (~ 2 GPa), and

therefore, it is unlikely to plastically deform at the cyclic stresses (~ 500 MPa) present at 1% strain amplitude in the DP 590 steel. As a result, plastic fatigue strain in DP 590 steel mostly resides in the ferrite constituent. As mentioned earlier, such concentration of plastic strain facilitates formation of PSB colonies in the very early stages of the process. However, PSBs do not cross the grain boundaries of ferrite or contiguous ferrite/martensite interfaces. Therefore, a PSB colony cannot grow to size larger than the corresponding ferrite grain. Consequently, continuous formation of new PSB colonies is essential to continue the PSB damage evolution process. The probability of formation of new PSB colonies is higher in the ferrite grains completely surrounded (or mostly surrounded) by martensite[1], because such ferrite grains are expected to have high concentration of local plastic strain as compared to the ferrite grains that have zero or low local contiguity with martensite. The concentration of such "heterogeneous" sites for formation of new PSB colonies decreases with the increasing number of fatigue cycles, which leads to decrease in the rate of formation of new PSB colonies (nucleation rate), and therefore, continuous decrease in the rate of change of ferrite normalized PSB colony volume fraction with the number of fatigue cycles.

HR 590 steel does not contain martensite. Therefore, the spatial distribution of local fatigue strain is expected to be uniform as compared to that in the DP 590 steel. Consequently, there are no preferred "heterogeneous" sites for formation of new PSB colonies in HR 590 steel as opposed to numerous such sites in DP 590 steel. Formation of PSBs in a ferrite grain can take place only when a certain accumulated local plastic

[1] This is directly related to global and local topological connectivity of martensite, which can be characterized only via reconstruction and visualization of three-dimensional microstructure. The present study did not involve reconstruction of three-dimensional microstructure. Therefore, there is no experimental evidence to support this hypothesis.

strain level is reached in that grain as Mughrabi [16] has shown in the case of single crystals. In HR 590 steel, as the fatigue plastic strain is distributed more uniformly, it takes a higher number of fatigue cycles to reach the required accumulated local plastic strain to initiate the strain localization resulting in PSB formation. Thus, initiation of PSB formation occurs at substantially higher number of fatigue cycles in HR 590 steel as compared to that in DP 590 steel. As more and more plastic fatigue strain accumulates with the increasing number of fatigue cycles, increasing number of ferrite grains are likely to reach the required local accumulated plastic strain to form PSB. Consequently, rate of formation of new PSB colonies can then increase with the number of fatigue cycles, which then accounts for observed increase in the rate of changes of ferrite normalized PSB colony volume fraction with the increase in the number of fatigue cycles leading to a value of exponent α larger than one.

The behavior of DP 980 steel that contains large amount of martensite (~ 70%) is closer to ferritic HR 590 steel rather than DP 590 steel containing 25% martensite. This is likely to be due to lower carbon content (~ 0.14 wt.%) of martensite in DP 980 steel compared to that in DP 590 steel (~0.4 wt.%). The calculated yield stress of martensite in the DP 980 steel is approximately 850 MPa (compare with ~ 2 GPa yield stress of martensite in DP 590 steel that contains ~ 0.4 wt.% C [166]), which is in the same range as the global cyclic stresses in DP 980 steel at 1% strain amplitude. Therefore, it may be said that depending on the local environment, some martensite islands in DP 980 steel are likely to plastically deform, and consequently, a portion of accumulated plastic strain resides in martensite. Consequence of this would be (1) lower overall accumulated plastic strain in ferrite, and (2) lower local concentration of plastic strain in ferrite grains.

Similar “strain-partitioning” has been observed for uniaxial tensile loading in DP steels by Chen et al [165]. This can lead to substantial decrease in the “heterogeneous” sites for initiation of formation of PSBs, and consequently, delayed initiation of formation of PSB colonies as compared to that in DP 590 steel, which is experimentally observed. Nonetheless, the reasons for increase in the rate of change of normalized ferrite volume fraction of PSB colonies with the number of fatigue cycles are not clear and need further investigation.

5.4.3.2 Path of PSB colony damage evolution

The path of PSB damage evolution is described by variation of ferrite normalized PSB colony total surface area S_f with the ferrite normalized PSB colony volume fraction V_f, rather than how these attributes individually vary with the number of fatigue cycles. Figure 5.19 to 5.21 depict the plots of S_f versus V_f for the three AHSS steels fatigued at 1% strain amplitude. For all three steels, the path of PSB damage evolution shows a strong linear trend. It is possible to collapse all data sets into a single linear trend. This is illustrated in Figure 5.22, which depicts variation of the product $[S_f\ (\lambda)^{2/3}]$ versus V_f, where λ is the ferrite grain size for DP 590 and HR 590 steel and mean intercept through ferrite in DP 980. The exponent, 2/3 results from an empirical fit. The factor $(\lambda)^{2/3}$ accounts for differences in grain size/mean intercept of ferrite in the three steels, which is expected to affect the growth rate and size of PSB colonies.

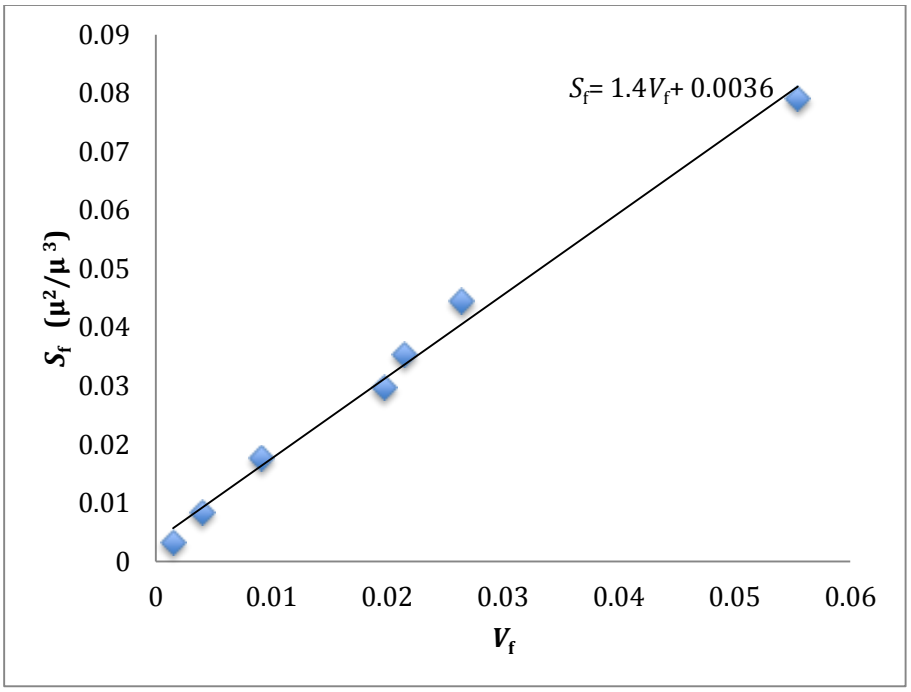

Figure 5.19: Plot of ferrite normalized total surface area of PSB colonies S_f vs. ferrite normalized volume fraction of the PSB colonies V_f for HR 590 steel fatigued at 1% strain amplitude.

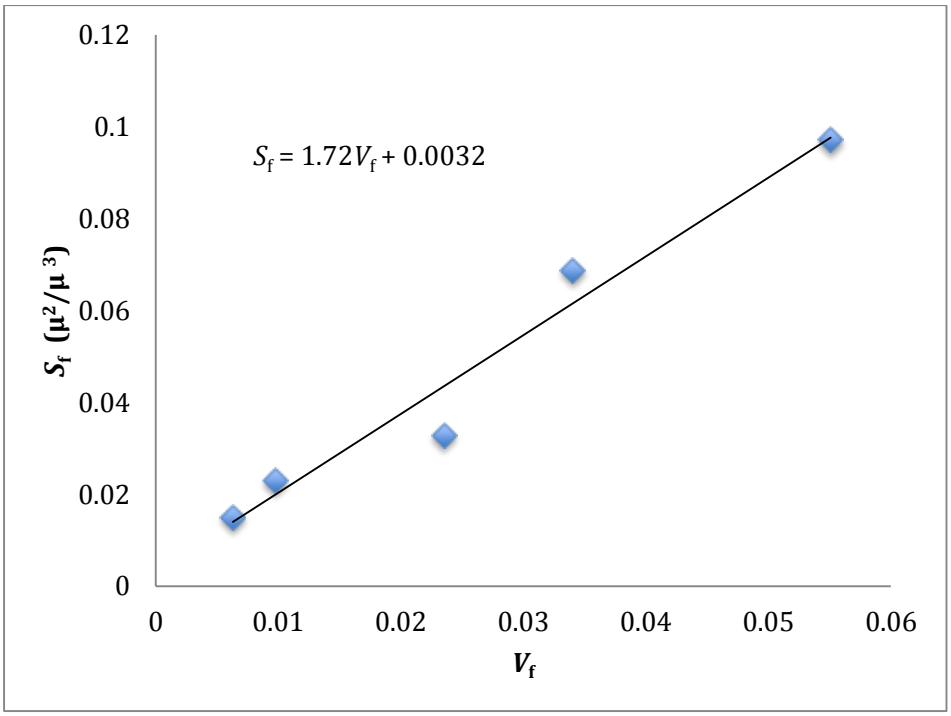

Figure 5.20: Plot of ferrite normalized total surface area of PSB colonies S_f vs. ferrite normalized volume fraction of the PSB colonies V_f for DP 980 steel fatigued at 1% strain amplitude.

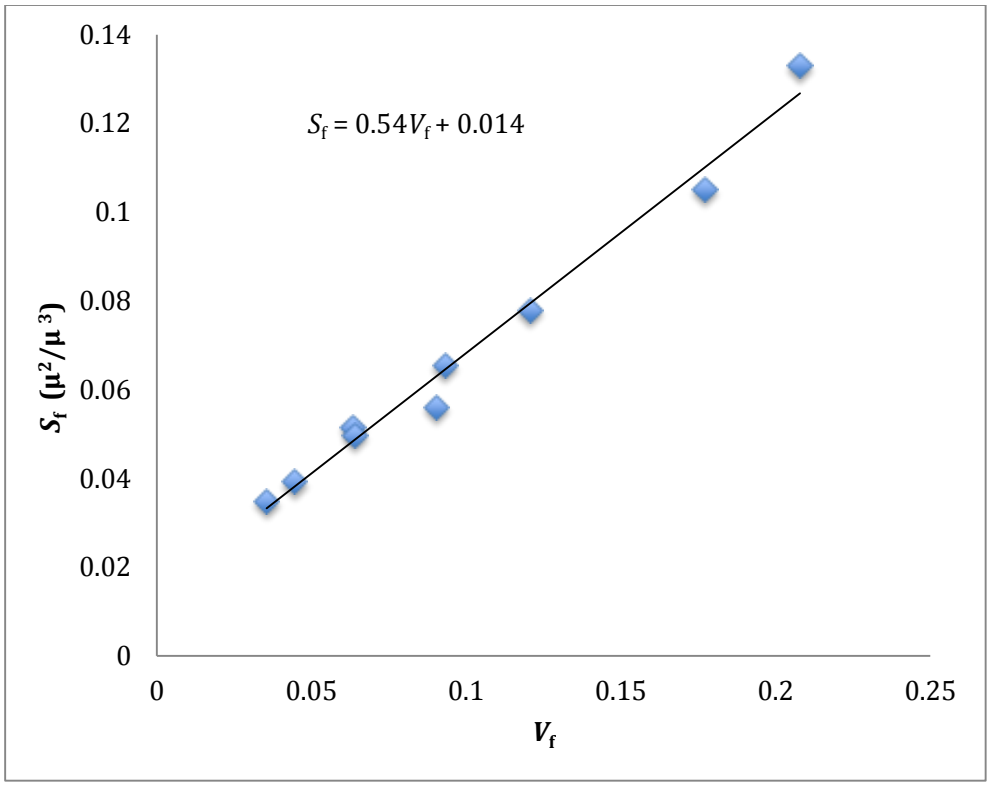

Figure 5.21: Plot of ferrite normalized total surface area of PSB colonies S_f vs. ferrite normalized volume fraction of the PSB colonies V_f for DP 590 steel fatigued at 1% strain amplitude.

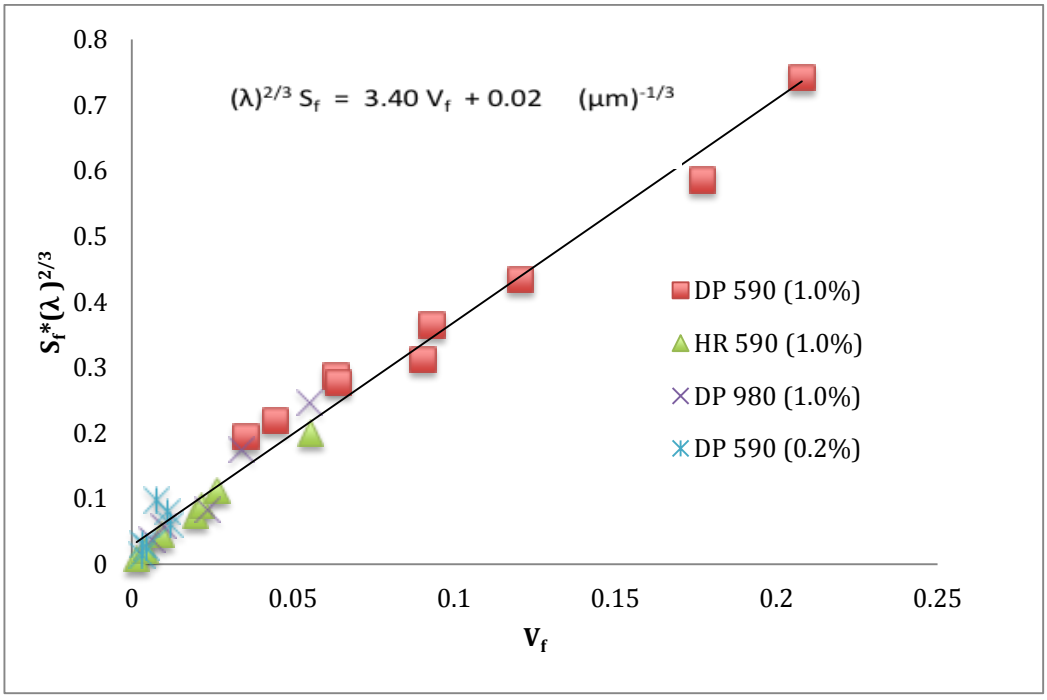

Figure 5.22: A plot of $[S_f (\lambda)^{2/3}]$ vs. V_f for DP 590 (1.0% and 0.2%), DP 980, and HR 590 steels.

The observed linear relationship between S_f and V_f is counter-intuitive because surface area is proportional to the *square* of the size, whereas volume is proportional to the *cube* of the size. Therefore, in general, surface area is not expected to vary linearly with volume. Consequently, the observed experimental linear relationship is a consequence of specific microstructural geometry and physics of PSB damage evolution in these steels. A simple geometric model is developed in the next sub-section that predicts a linear relationship between S_f and V_f .

5.4.3.3 Geometric model for path of PSB related damage evolution

It has been reported that in polycrystalline 6061-T6 Al of 20 μm grain size, growth rate of individual PSBs *decreases* with increase in the number of fatigue cycles [123]. Experimental observations on a polycrystalline ferritic stainless steel of 38 μm also showed that PSB growth is initially high; it decreases with the number of cycles; and approaches zero [124]. These data on Al and ferritic stainless steel suggest that in other polycrystalline alloys as well, growth rate of individual PSBs may decrease with the number of cycles and PSBs (and therefore, PSB colonies) may reach a saturation size and not grow thereafter. On this basis, it is assumed that the PSB colonies in the present AHSS steels reach a saturation size soon after they are formed (nucleated) and do not grow thereafter. Number of fatigue cycles, Δ needed to reach the saturation size is expected to depend on numerous parameters including the grain size. The AHSS steels of interest in the present work have very fine microstructures: the ferrite grain size in HR 590 steel and mean intercept in DP 980 steel are 4.0 μm, and ferrite grain size in DP 590 steel is 13 μm. On this basis, it is assumed that in the present AHSS steels, once a PSB colony is formed, it quickly reaches a saturation size that is determined by the size of the

ferrite grain in which the colony is formed, i.e., Δ is small and independent of number of fatigue cycles *n*. It is further assumed that the formation of new PSB colonies is a continuous process that begins at number of fatigue cycles n_0 when the first colony is formed. For the sake of simplicity, also assume that all ferrite grains/islands are of the same size (equal to average size in the real microstructures), and consequently, all *saturated* PSB colonies are also of the same size (equal to or smaller than ferrite grain size) that is independent of number of fatigue cycles *n*. Let V^* and S^* be volume and surface area of individual *saturated* PSB colony, respectively. Let N_V be the number of *saturated* PSB colonies at n fatigue cycles. Therefore, the contributions of *saturated* PSB colonies to volume fraction V_V and total surface area per unit volume S_V are $[V^* \cdot N_V]$ and $[S^* \cdot N_V]$, respectively. In addition, there is a contribution to V_V and S_V from recently formed PSB colonies that are still growing and have not reached saturation size at n fatigue cycles. A colony nucleated at (n-Δ) fatigue cycles saturates in size at *n* fatigue cycles. Thus, all colonies nucleated from (n-Δ) to *n* cycles have yet to reach the saturation size at *n* cycles. Let N_{us} be the number of unsaturated PSB colonies per unit volume at n fatigue cycles, i.e., this is the number of new colonies formed from (n-Δ) to *n* cycles. As it is assumed that Δ is small, it follows that during most of the fatigue process, $N_{us} << N_V$. Let V_{us} , S_{us} be the volume fraction and total surface area per unit volume of the these *unsaturated* PSB colonies. The volume of individual unsaturated colonies ranges from 0 to V^* and surface area ranges from 0 to S^* and $N_{us} << N_V$, consequently, for most of the fatigue process, $V_{us} << [V^* N_V]$ and $S_{us} << [S^* N_V]$. Under the present assumptions, following equations can be written for volume fraction V_V and total surface area per unit volume S_V of the PSB colonies.

$$V_V = [V^* N_V] + V_{us} \quad (5.8)$$

$$S_V = [S^* N_V] + S_{us} \quad (5.9)$$

Equations (5.8) and (5.9) lead to the following.

$$S_V = [S^*/ V^*] V_V + \{S_{us} - [S^* V_{us}/ V^*]\} \quad (5.10)$$

Dividing equation (5.10) by ferrite volume fraction f yields the following result.

$$S_f = K_1 V_f + K_2 \quad (5.11)$$

where, $K_1 = S^*/ V^*$ and $K_2 = \{S_{us}-[S^* V_{us}/ V^*]\}/f$

As S^* and V^* are surface area and volume of saturated PSB colonies and K_1 is equal to the ratio S^*/ V^*, for the present model, K_1 is independent of number fatigue cycles n. The second parameter in equation (5.10), K_2 is expected to be quite small because during most of the fatigue process (except in very initial stages), $N_{us} << N_V$ and average surface area and volume of unsaturated colonies have to be less than S^* and V^*, respectively. Thus, equation (5.11) predicts that at a given strain amplitude, the plot of S_f versus V_f should be linear except in the very initial stages of the PSB damage evolution process, which is experimentally observed (see Figures 5.19 to 5.21). The slope of such linear plot is equal to K_1 (i.e., ratio S^*/ V^*). If it is assumed that PSB colonies have a convex shape (which is reasonable), one measure of average size [167] of the PSB colonies D_C is equal to [6 V^*/ S^*]. Thus, slope, K_1 is equal to [6/D_C]. Since the size of saturated PSB colonies is related to grain size/mean intercept of ferrite, the model predicts that the slope K_1 must increase as the ferrite grain size decreases. Interestingly, the slope of S_f vs. V_f plot for HR 590 steel (ferrite grain size of 4.0 μm) 1.4 $(\mu m)^{-1}$ is substantially higher than the value 0.54 $(\mu m)^{-1}$ for DP 590 steel (ferrite grain size of 13.0 μm), but it is comparable to the

value of 1.72 $(\mu m)^{-1}$ for DP 980 steel (ferrite mean intercept of 4.0 μm). Therefore, experimental data are in very good agreement with the predictions of the model.

Equation (5.11) can be written in the following alternate form.

$$[V^*/ S^*]S_f = V_f + K_2 [V^*/ S^*] \quad (5.12)$$

As mentioned earlier, average size of PSB colonies $D_C = 6 [V^*/S^*]$. Therefore, equation (5.12) can be also written as follows.

$$[D_C]S_f = 6V_f + 6K_2 [V^*/ S^*] \quad (5.13)$$

The average size of saturated PSB colonies D_C is a function of the grain size/mean intercept of ferrite λ, i.e., $D_C = g(\lambda)$. The exact functional form g (λ) is not known, but one can write;

$$g(\lambda) S_f = 6V_f + K_3 \quad (5.14)$$

where, $K_3 = 6K_2 [V^*/ S^*]$

Again, K_3 is expected to be very small as compared to the first term $6V_f$ in the right hand side of equation (5.14) for the reasons given earlier. The average size of saturated PSB colonies D_C must be in the range of 0 to λ, because PSB colonies do not cross boundaries of the ferrite grains in which they are formed. Further, it is experimentally observed that some PSB colonies do not completely occupy the corresponding ferrite grain, implying that the average PSB colony size D_C must be less than λ. A simple and flexible functional form g (λ) that satisfies these requirements is two-parameter power law relationship given below.

$$g(\lambda) = a \lambda^m \quad (5.15)$$

In equation (5.12), m and a are constants. Equations (5.14) and (5.15) lead to the following result.

$$\lambda^m S_f = C_1 V_f + C_2 \quad (5.16)$$

where, $C_1 = 6/a$ and $C_2 = K_3/a$

If equation (5.16) is applicable, a plot of $[\lambda^m S_f]$ vs. V_f should be linear and the data sets corresponding to all ferrite grain sizes and strain amplitudes must fall on the same linear trend. Figure 5.22 shows that the present data sets for the three AHSS steels and two strain amplitudes follow the behavior predicted by equation (5.16) with m = 2/3, which further validates the geometric model represented by equation (5.11). Qualitative microstructural observations, quantitative microstructural data, data analysis and validated geometric model reveal the following picture of the evolution of PSBs in the three AHSS steels.

PSBs are present in the form of colonies in the ferrite grains. Once a PSB colony is formed it grows quickly to the saturation size and does not grow thereafter. The evolution of PSB colonies is then only due to formation of new colonies with the increase in the number of fatigue cycles. The saturation size of PSB colonies is governed by the ferrite grain size. Therefore, in a given microstructure, the kinematics of PSB evolution is primarily governed by the rate at which new PSB colonies form (i.e., "nucleation" rate). Such PSB evolution is primarily due to fine ferrite grain size in these steels; PSBs in steels having significantly coarser ferrite grain size (say 50 μm) are not likely to exhibit similar behavior.

5.4.3.4 Evolution of Total Surface Area of PSBs per unit volume

A PSB colony contains several PSBs that are oriented parallel to one another. The total surface area of the PSB surfaces (which is different from total surface area of PSB colonies) per unit volume has been experimentally measured as a function of

number of fatigue cycles using stereological techniques reported in Chapter 4. Figures 5.23 (a) to (c) depict variation of ferrite normalized total surface area of the PSB interfaces per unit volume S_{PSB} with the number of fatigue cycles. In all three steels, S_{PSB} increases monotonically with the increase in the number of fatigue cycles. S_{PSB} can increase due to formation of new PSBs in the existing colonies and/or due to formation of new colonies. Further, PSB surface area for a colony can increase due to increase in the size of the colony and/or by addition of new PSBs in the existing PSB colonies without change in the overall colony size. Variation of S_{PSB} with the ferrite normalized PSB volume fraction of PSB colonies can provide information on which of these mechanism(s) are operative. Figures 5.24 (a), (b) and (c) show plots of S_{PSB} versus ferrite normalized PSB colony volume fraction V_f for the three AHSS steels at 1% strain amplitude. All three steels exhibit strong linear trend, which implies that an increase in the total surface area of the PSBs is primarily due to the formation of new PSB colonies and not due to creation of new PSBs in the existing colonies. Similar to the case of S_f, it is possible to collapse all data sets into a single linear trend. This is illustrated in Figure 5.25, which depicts variation of the product $[S_f (\lambda)^{0.2}]$ v/s V_f , where λ is the ferrite grain size for DP 590 and HR 590 steel and mean intercept through ferrite in DP 980. The factor $(\lambda)^{0.2}$ accounts for differences in grain size/mean intercept of ferrite in the three steels, which is expected to affect the growth rate and size of PSB colonies.

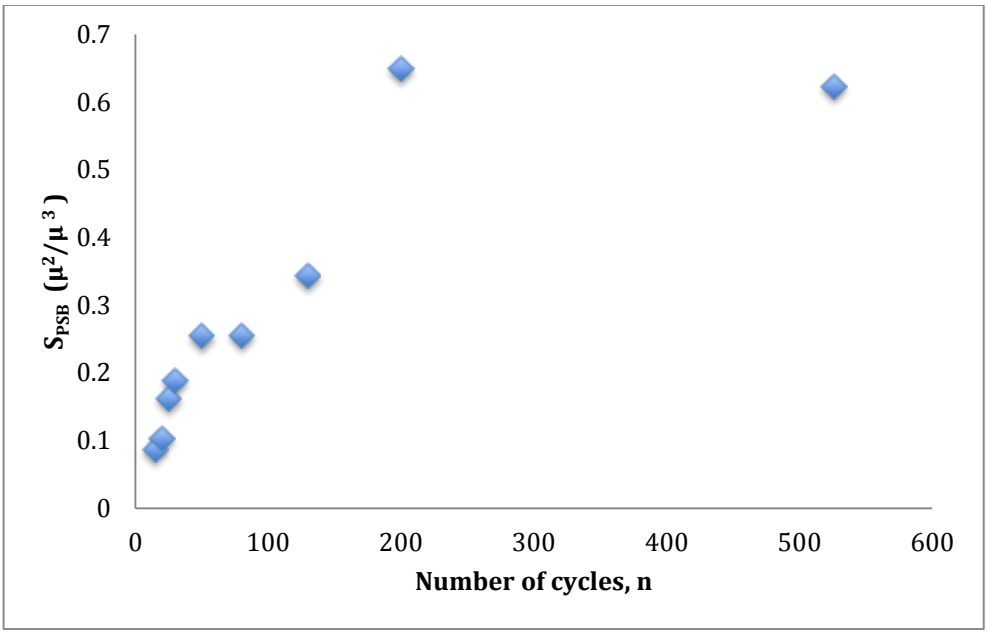

(a)

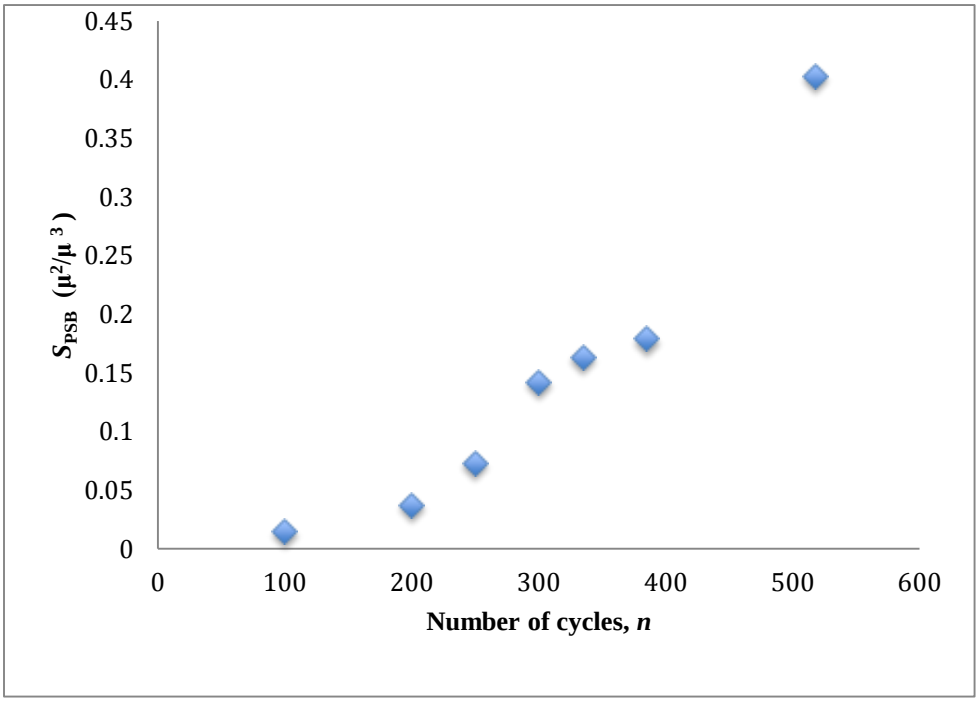

(b)

Figure 5.23: Variation of estimated total surface area per unit volume of the PSBs with number of fatigue cycles at 1.0% total strain amplitude for (a) DP 590, (b) HR 590 and (c) DP 980 steels.

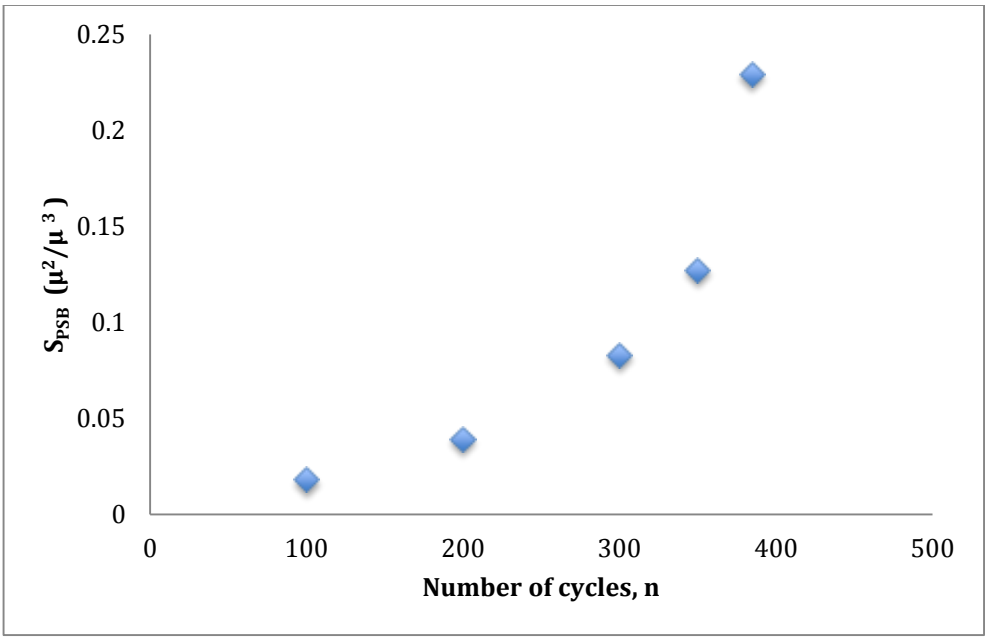

(c)

(Figure 5.23 continued)

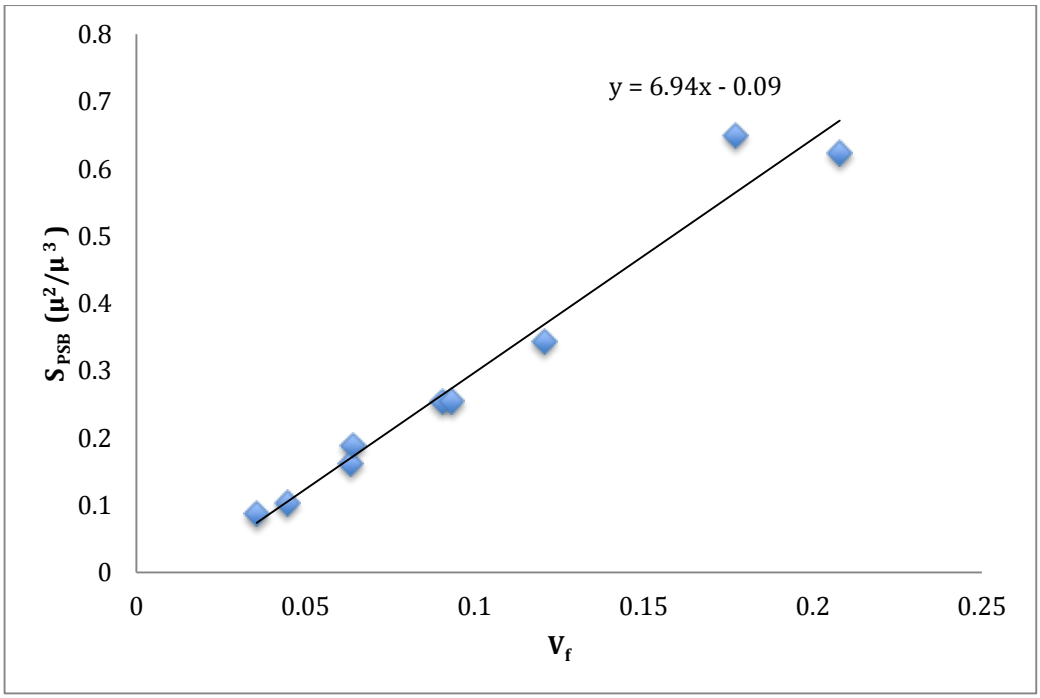

(a)

Figure 5.24: Plots of total surface area per unit volume of PSBs v/s the volume fraction of the colonies for a) DP 590, b) HR 590, c) DP 980 steels fatigued at 1.0% total strain amplitude.

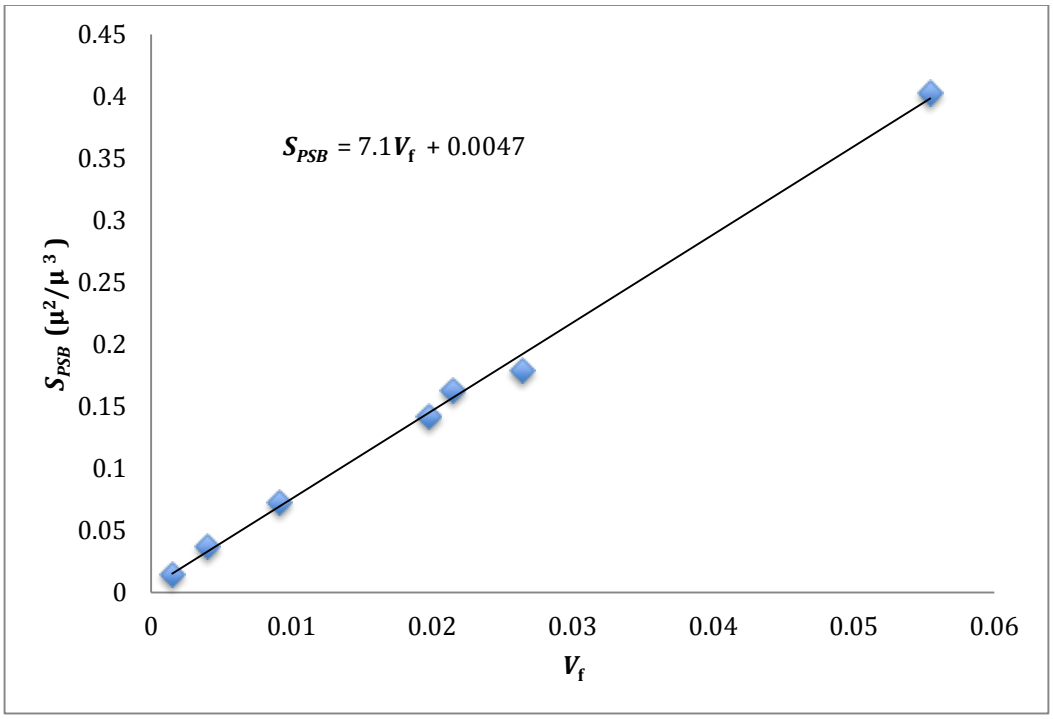

(b)

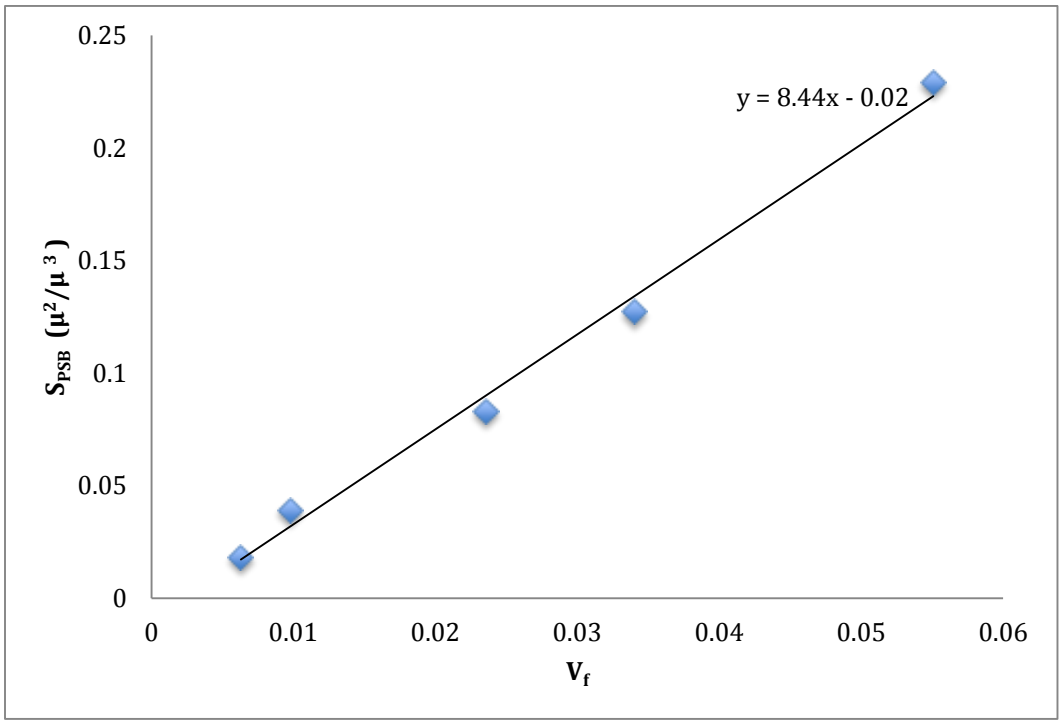

(c)

(Figure 5.24 continued)

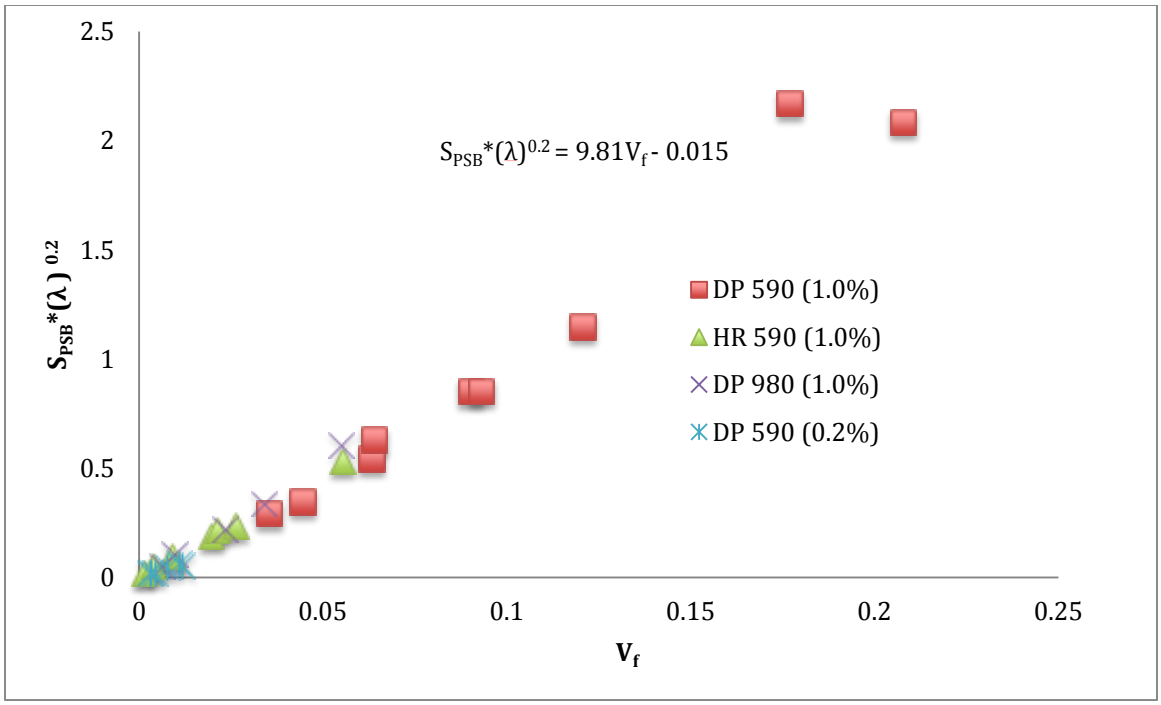

Figure 5.25: A plot of [S_{PSB} $(\lambda)^{0.2}$] v/s V_f for DP 590 (1.0% and 0.2%), DP 980, and HR 590 steels.

Therefore, from the data shown in this section, it can be concluded that ferrite grain size is a critical microstructural parameter that affects the evolution of the PSB colonies as well as individual PSBs. Section 2.2.3-A and section 2.2.5 have discussed several works that have studied the importance of grain size in PSB related deformation. The limiting effect of grain boundaries due to associated back stresses that prevent the free growth of PSBs and PSB colonies has been mentioned. Similarly, studies by Man et al [31] have looked at the evolution of the PSBs in materials with varying grain sizes and determined that the nature of PSB growth changes with grain size. However most of these studies have been highly localized in nature. Also, they often restrict any quantitative discussion about the effect of grain size to observations in the two-dimensional regime. In contrast, the present work has used unbiased sampling over a large area to make two-dimensional

measurements and using stereology estimated evolution of three-dimensional properties of PSBs and PSB colonies.

5.4.3.5 Angular orientation distribution of the PSBs

As discussed in Chapter 2, fatigue literature consists of a considerable amount of work with respect to the characterization of the PSBs, which are often the precursors of cracks in a material [1, 31, 168]. However, most of these studies are qualitative in nature with almost no attention given to the three-dimensional (3D) angular orientation distribution of the PSBs with respect to the number of cycles and its variation with strain amplitude and/or microstructure. The objectives of this section are (1) to present a flexible and straight-forward practical quantitative metallographic technique for estimation of morphological 3D angular orientation distribution of PSBs from experimentally measured angular orientation distribution of the PSMs observed in a specimen surface plane(s) parallel to the loading direction, and (2) to apply the new technique for characterization of the evolution of the 3D angular orientation distribution of the PSBs formed during cyclic loading of cold rolled DP 590 steel as a function of number of fatigue cycles. In this context, as discussed before, it is important to point out that although PSBs have been studied extensively, majority of the earlier investigations were on FCC single crystals, and the studies on polycrystalline metals are mostly limited to FCC single phase metals and alloys. There have been a few investigations on characterization of PSBs in two-phase or multi-phase polycrystalline alloys having BCC matrix phase. To the best of authors' knowledge this is the first investigation on characterization of PSBs in advanced high strength sheet (AHSS) steels including steels with multiple phases.

The stereological technique presented in this section is applicable for characterization of 3D morphological orientation distribution of PSBs in single phase or multiphase polycrystalline metals having equiaxed grain shape and no preferred crystallographic texture (or crystallographic texture and morphological anisotropy that is symmetric with respect to the loading direction) deformed under uniaxial loading. The technique is also applicable for characterization of 3D morphological orientation distribution of grain boundary facets or any microstructural interfaces, in general, where 3D angular orientation distribution has a symmetry axis.

Characterization of 3D angular orientation distribution of the PSBs essentially involves estimation of morphological anisotropy of the faces of the bands. Hilliard [140] has given a rigorous stereological analysis of the problem of estimation of 3D angular orientation distribution of an ensemble of microstructural surfaces from the measurements of intersection counts performed with straight test lines of different angular orientations placed in the test planes of different orientations in the 3D microstructural space. Nevertheless, the technique requires measurements on metallographic sections of different orientations in 3D space through the specimen so as to uniformly sample the whole range of orientation in the 3D space, which is very tedious and time consuming. Further, application of Hilliard's theoretical results involves complex numerical computations involving representation of the orientation distribution in terms of a series of spherical harmonics. Consequently, although Hilliard's method has been available for more than 50 years, there have been very few practical applications of the method reported in the literature. Davies and Wilshire [169] have analyzed geometric problem of estimation of 3D angular orientation distribution of planes of infinite extent in

3D space from the measurements performed on their traces in sectioning planes. As the deformation bands (and therefore, their faces) are of finite size, Davies and Wilshire's method is not applicable for their characterization. Scriven and Williams [170] have given an integral equation that relates the 3D angular orientation distribution of planar grain boundary facets of finite extent to the apparent distribution of their traces in the metallographic sections. Nonetheless, Scriven and Williams [170] assumed that all grain boundary facets are of the same size and are of equiaxed shape. Further, their analysis ignores the size dependence of the probability of intersection of grain boundary facets with sectioning planes. These assumptions and approximations are not necessarily applicable to the deformation bands generated by cyclic loading. The present analysis does not involve any assumptions concerning sizes and shapes of the bands or parallel faces of the deformation bands and it leads to a straight-forward computational algorithm that can be implemented in an Excel spread-sheet. The method enables estimation of distribution of 3D orientations of the *surface areas* of parallel faces of the deformation bands which is more useful than their number distribution (as in Scriven and William's approach) as larger bands with higher surface areas contribute more to the global plastic fatigue strain. The analysis draws significantly from the design-based stereological sampling technique of vertical sections [145, 146, 148]. The theoretical development has been presented in the chapter 3. This chapter presents a practical application of the methodology for estimation of 3D orientation distribution of the PSBs in fatigued specimens of cold rolled DP 590, DP 980 and hot rolled HR 590 steels.

Images used for making surface measurements such as PSB colony area fraction have been used for this analysis. The methodology used for obtaining the images has

been described in section 4.6. Using these images, the two-dimensional (2D) angular orientation distributions of the PSMs have been made using the process described in detail in section 4.6.2. Figures 5.26 (a) – (d) depict typical fields of view with PSB colonies as observed in the cycle range 15 through 30 for DP 590 steel. This data is utilized to estimate 3D angular orientation distributions of PSBs at different fatigue cycles as discussed in the next section.

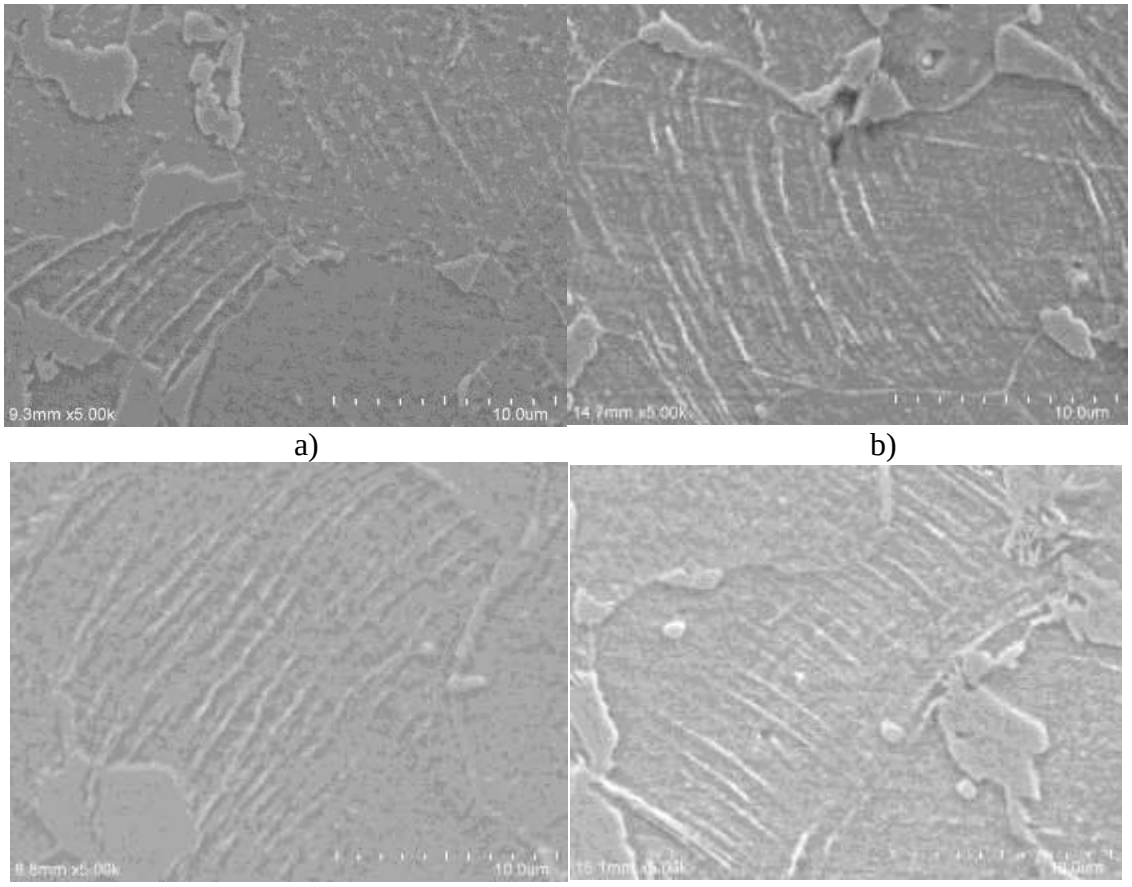

Figure 5.26: Representative images for extrusion colonies for sample fatigued at 1% strain amplitude after a) 15 cycles; b) 20 cycles; c) 25 cycles and d) 30 cycles. Horizontal direction represents the loading axis.

A) 2-D Angular Orientation Distributions of PSMs

2-D angular orientation distributions of the PSM's at different numbers of cycles for the three steels are shown in Figure 5.27, Figure 5.28 and Figure 5.29. Only the

samples fatigued at 1.0% total strain amplitude have been included. The x-axis in these figures represents the 2-D angular range while the y-axis represents the fraction of the total length of all the PSBs across all orientations within that 2-D angular range. It is observed that 2D angles (α) less than 30^0 are rarely observed. Also, irrespective of the steel microstructure, the 2D angles between 40^0 and 60^0 with respect to stress axis had the highest frequency.

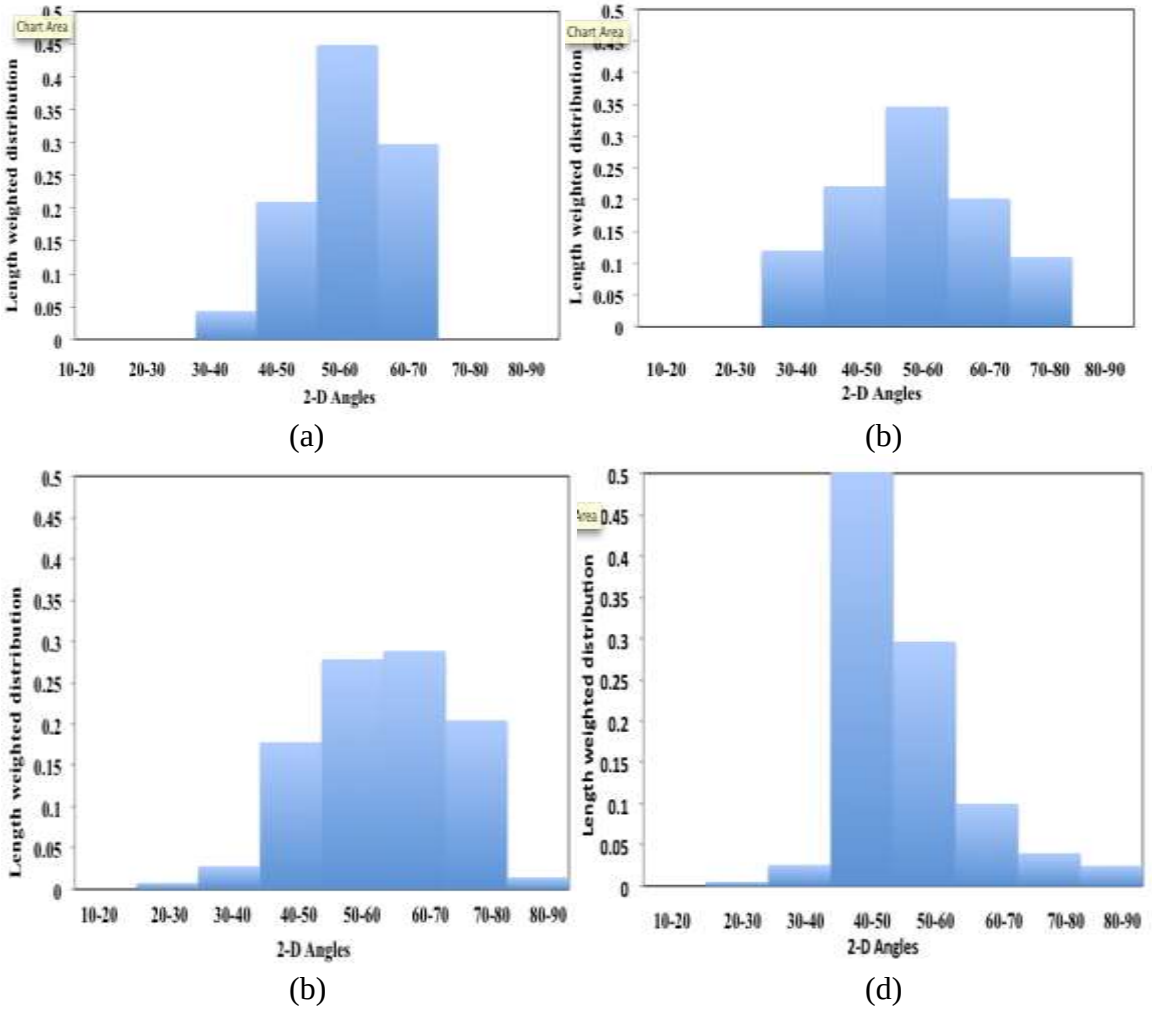

Figure 5.27: 2D angular distribution of the PSMs on the DP 590 (1.0%) interrupted fatigue test specimen. Figures (a) – (i) represent the measured distributions at a) 15 cycles; b) 20 cycles; c) 25 cycles; d) 30 cycles; e) 50 cycles; f) 80 cycles; g) 130 cycles; h) 200 cycles; and i) 526 cycles (at failure).

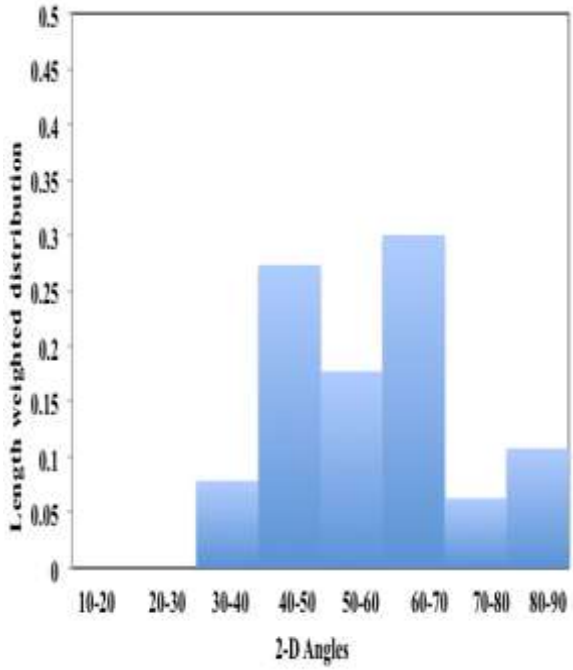

(e)

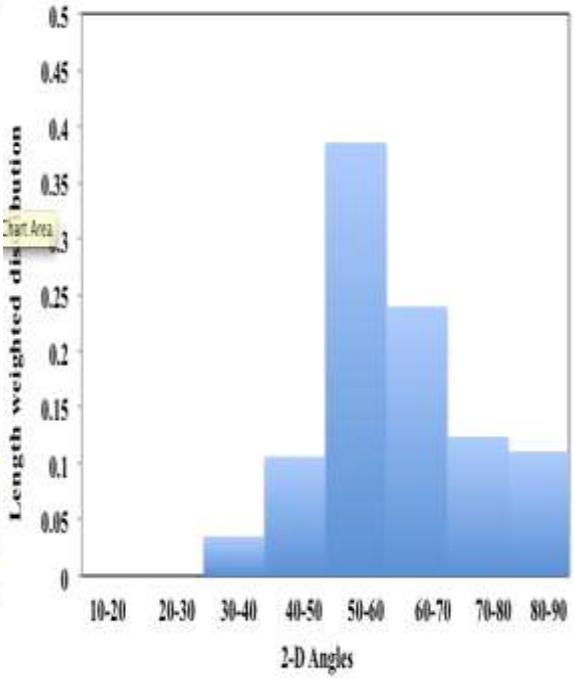

(f)

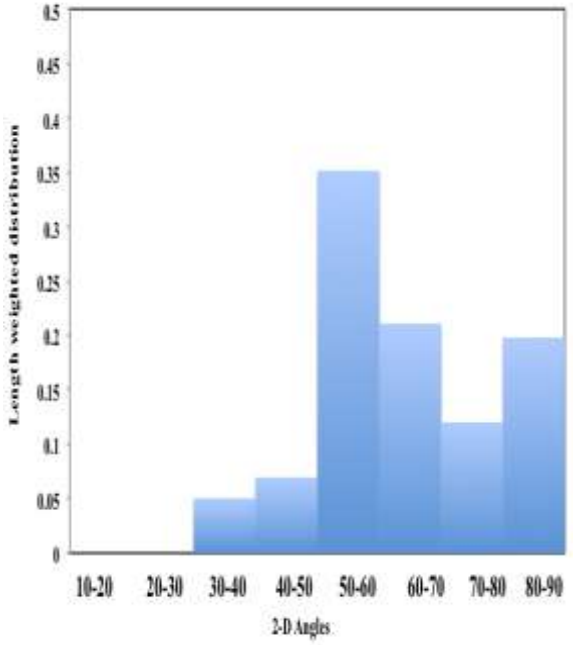

(g)

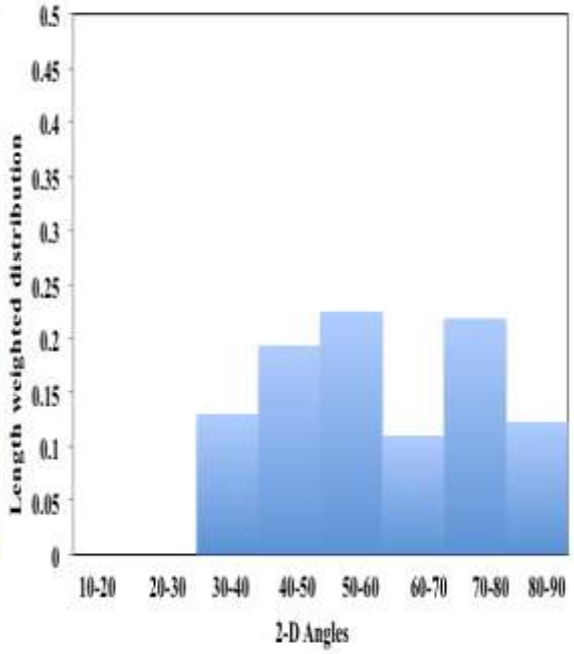

(h)

(Figure 5.27 continued)

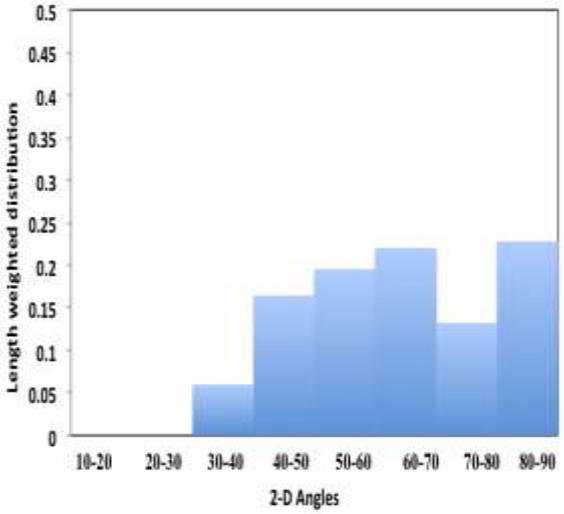

(i)

(Figure 5.27 continued)

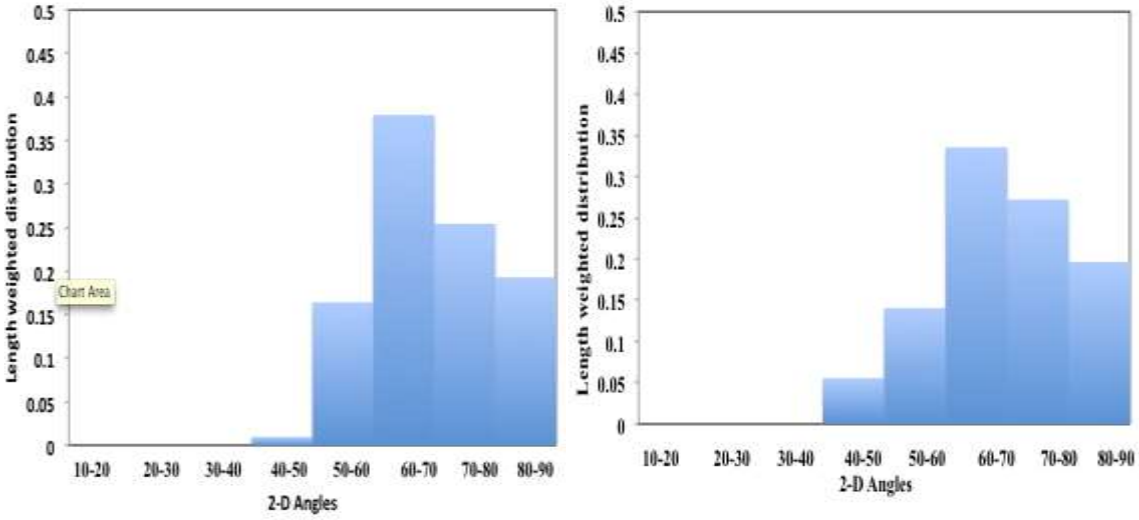

a) b)

Figure 5.28: 2D angular distribution of the PSMs on the HR 590 (1.0%) interrupted fatigue test specimen. Figures (a) – (g) represent the measured distributions a) 200 cycles; b) 250 cycles; c) 300 cycles; d) 335 cycles; e) 385 cycles; and f) 518 cycles (at failure).

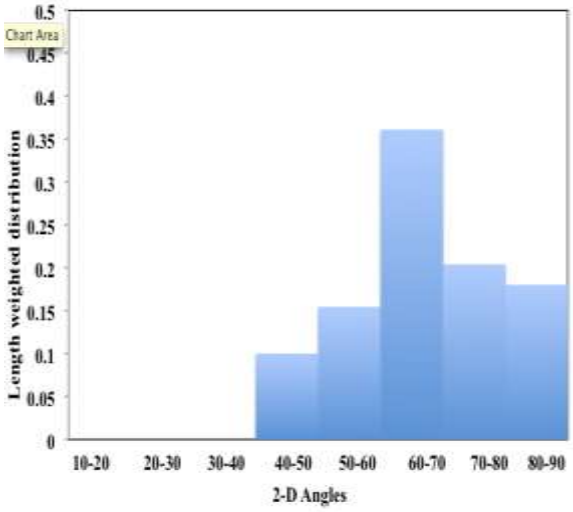

c)

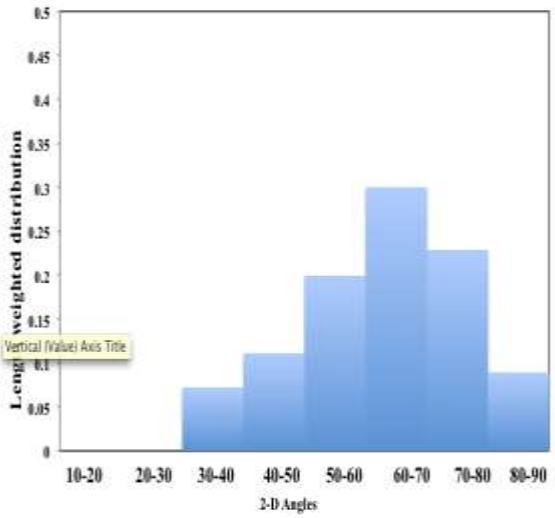

d)

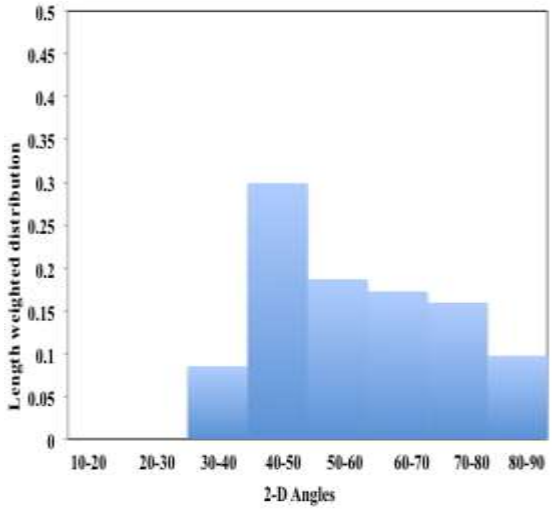

(e)

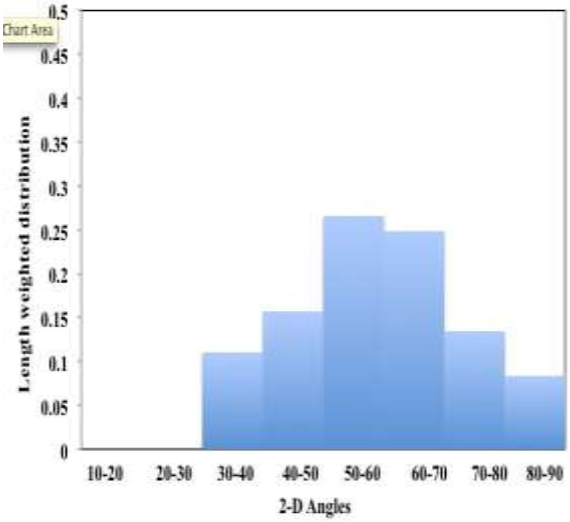

(f)

(Figure 5.28 continued)

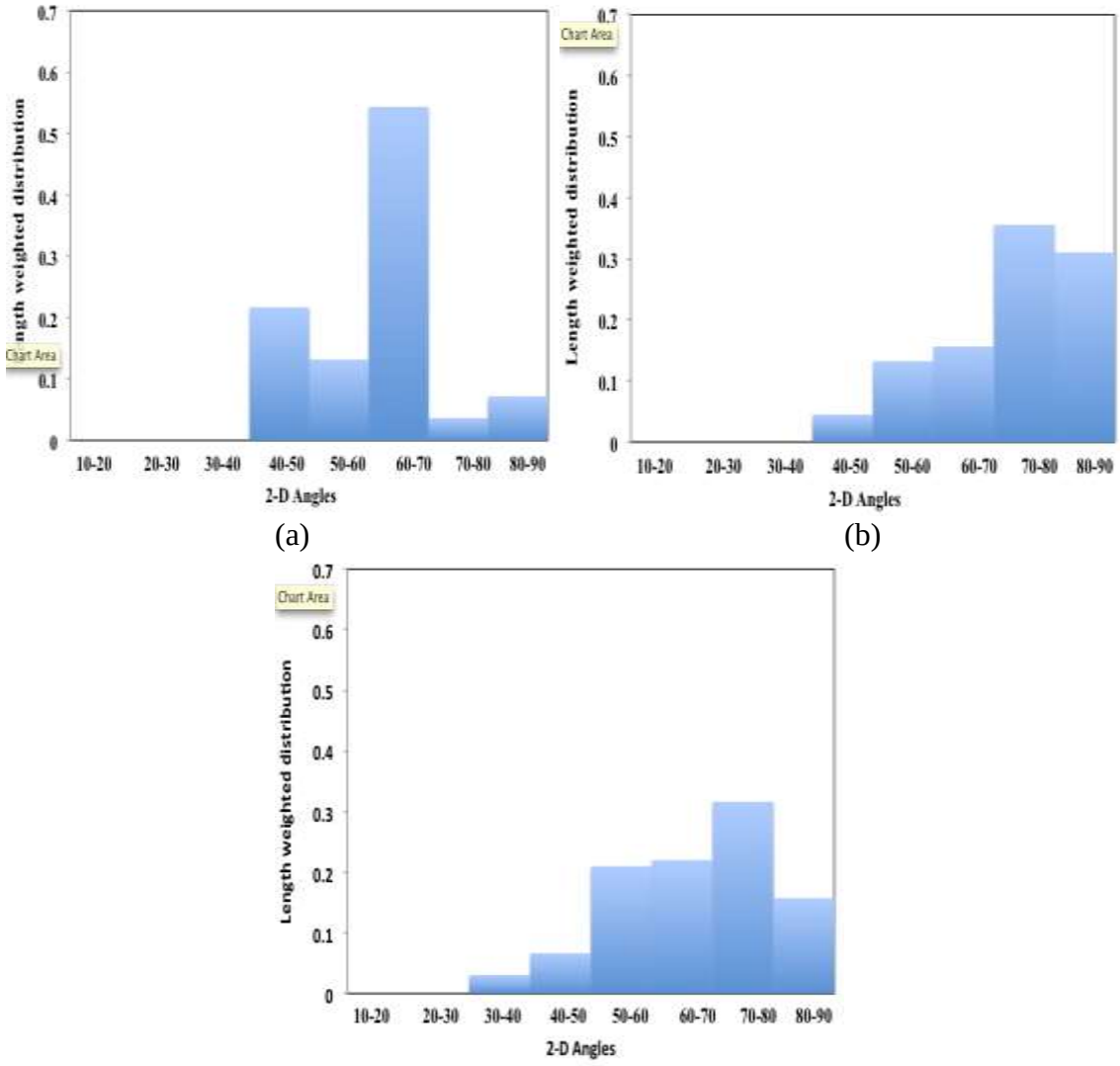

Figure 5.29: 2D angular distribution of the PSMs on the DP 980 (1.0%) interrupted fatigue test specimen. Figures (a) – (c) represent the measured distributions at a) 300 cycles; b) 350 cycles; and c) 385 cycles (at failure).

It is observed that in all three steels, as the number of cycles increased, the 2D orientations between 50^0 and 80^0 became the preferred orientations. Also, it should be mentioned that for any given steel, the number of PSB colonies increased with the number of fatigue cycles. As a result, for the same area, the sample size of the colonies on which measurements were performed also increased reducing the sampling error. The 2D angular distribution was not obtained for the DP 590 specimen fatigued at 0.2% total

strain amplitude. This was because even at failure, the total number of colonies present on the surface was too low to make any reasonable quantitative estimates for the angular distribution of the PSBs.

B) 3-D Angular Orientation Distributions of PSBs

Using the methodology described in section 3.1, one can obtain the discretized 3D angular distribution for the PSBs from the 2D angular distribution data obtained in the previous section. The coefficients a[i, j] are used to obtain the distributions for the three steels in the study as shown in Figure 5.30, Figure 5.31 and Figure 5.32.

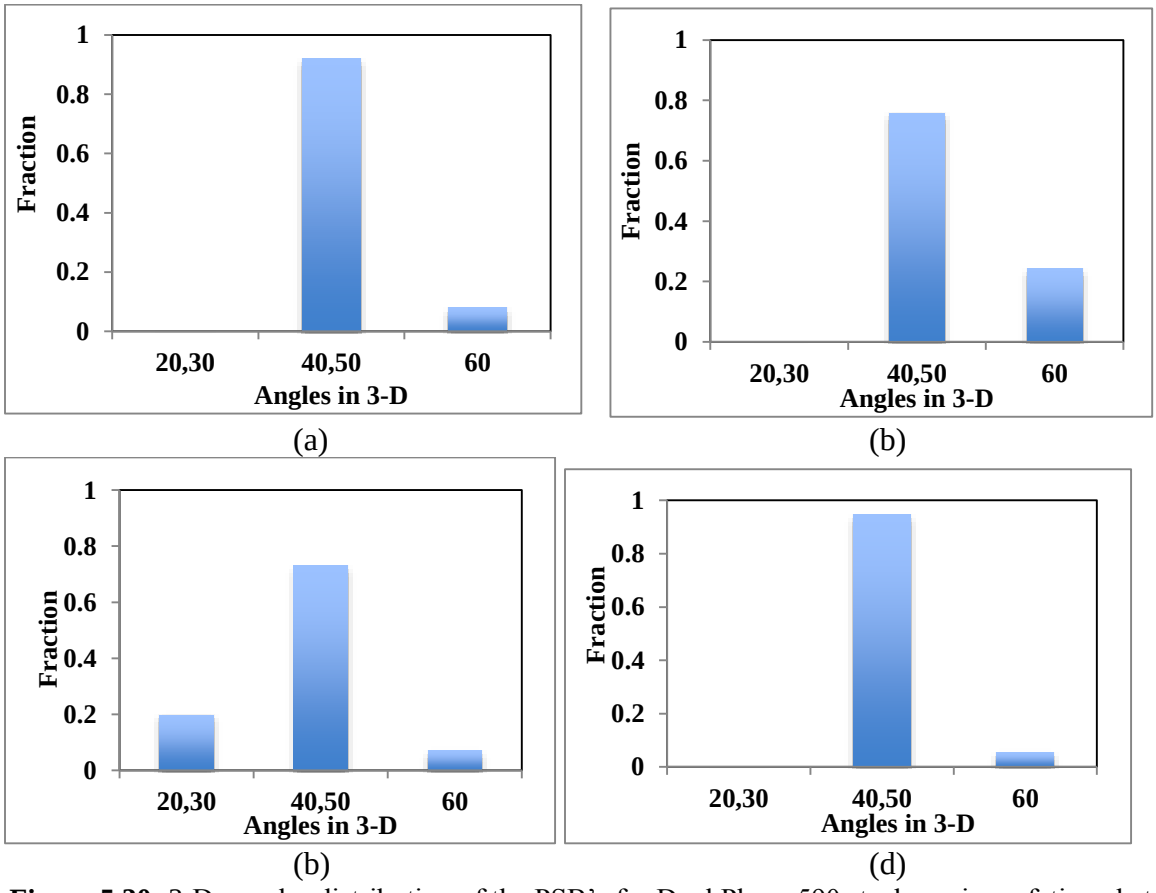

Figure 5.30: 3-D angular distribution of the PSB's for Dual Phase 590 steel specimen fatigued at 1% strain amplitude at a) 15 cycles; b) 20 cycles; c) 25 cycles; d) 30 cycles; e) 50 cycles; f) 80 cycles; g) 130 cycles; h) 200 cycles; and i) 526 cycles (at failure. It can be observed that angles greater than 60 degrees and lower than 30 degrees are almost negligible and that the bulk of the angles are composed of discreet values of 40 and 50 degrees.

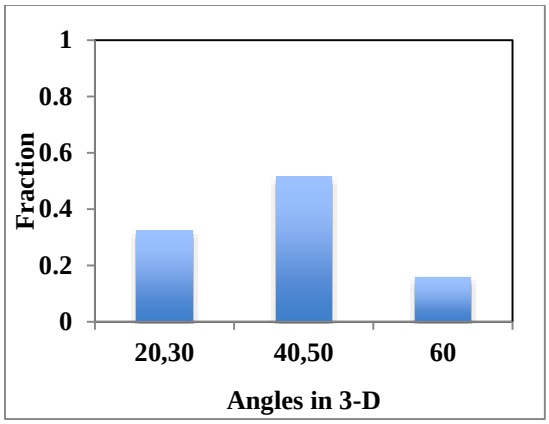

(e)

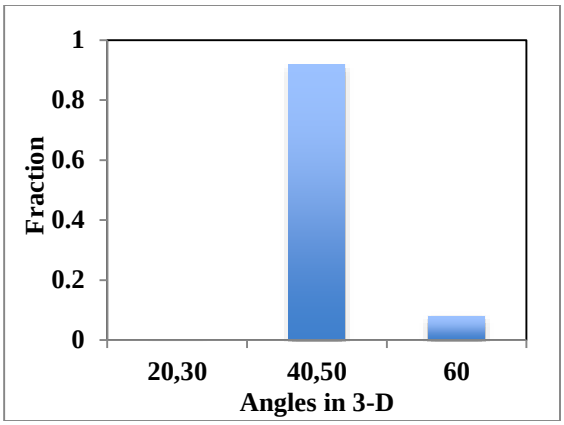

(f)

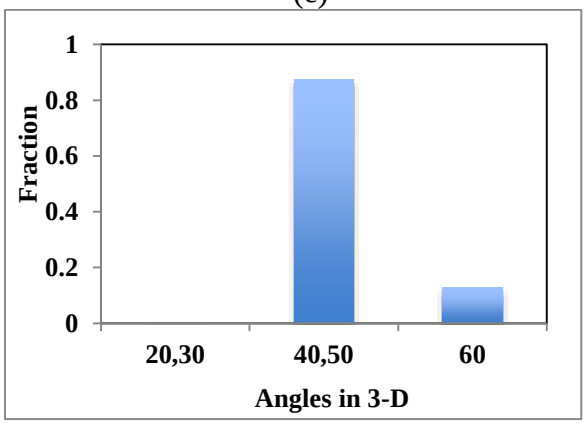

(g)

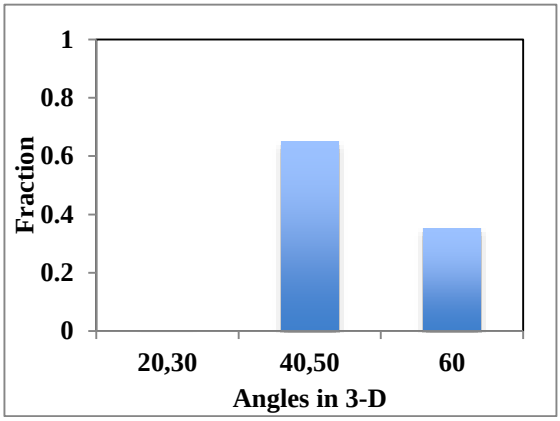

(h)

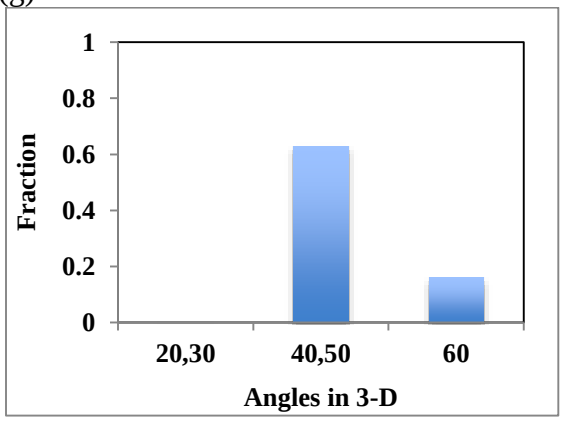

(i)

(Figure 5.30 continued)

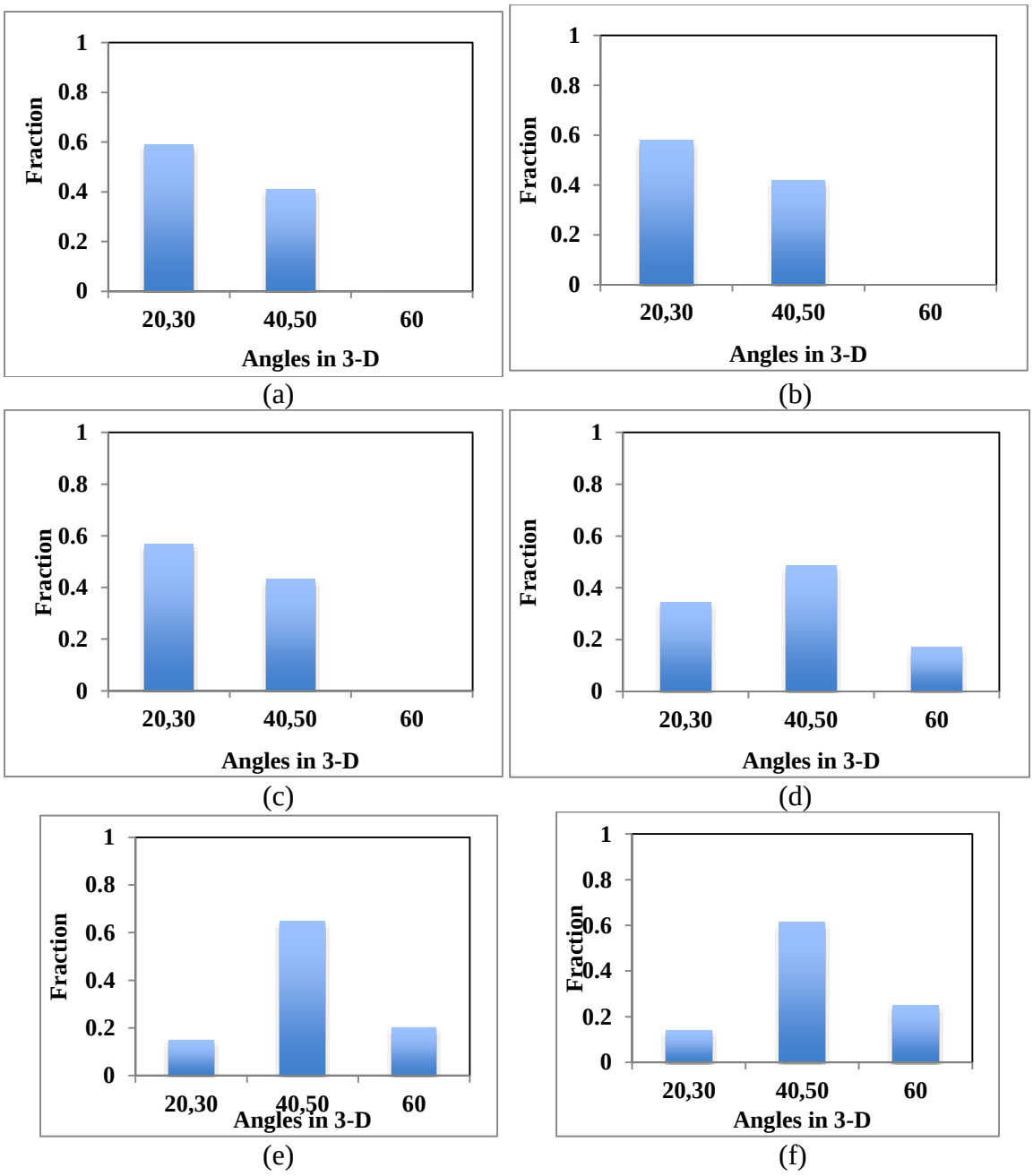

Figure 5.31: 3-D angular distribution of the PSB's for HR 590 steel specimen fatigued at 1% strain amplitude at a) 200 cycles; b) 250 cycles; c) 300 cycles; d) 350 cycles; e) 385 cycles; and f) 518 cycles (at failure).

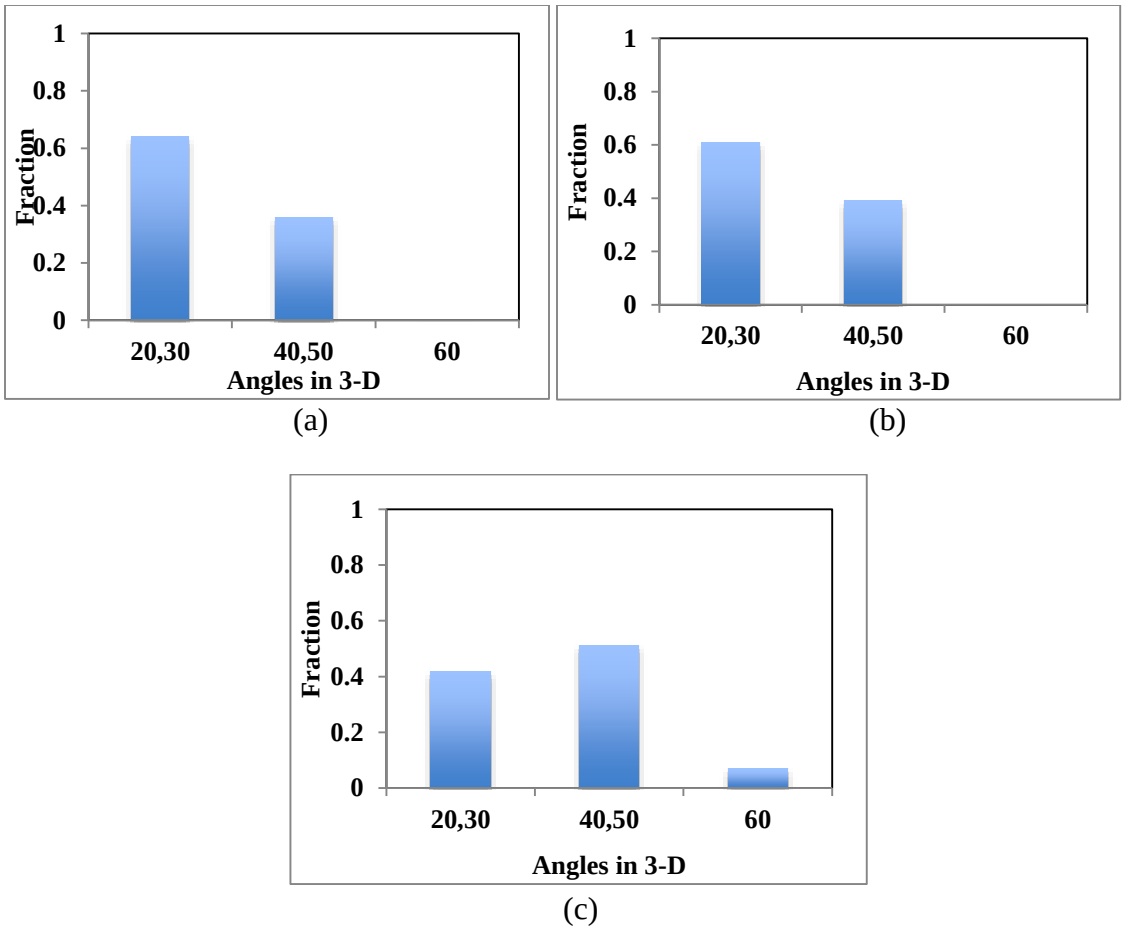

Figure 5.32: 3-D angular distribution of the PSB's for DP 980 steel specimen fatigued at 1% strain amplitude at a) 300 cycles; b) 350 cycles; and c) 385 cycles (at failure).

Several interesting observations can be made from the analysis of the 2D and 3D angular distributions of the PSMs/PSBs. For example, PSMs with α orientations less than 30^0 were found to be rare. As mentioned in section 2.2.5, similar observations have been made by Polak et al [125] and Girones et al [126] who found the lowest 2D angular orientation of the PSMs to be 25^0. These studies have reported the 2D angles to range between 25^0 and 90^0. The range for these angles in the present study was also found to be similar and lying between 30^0 and 90^0. The same studies have reported that the most common α value was 45^0. However in the present work, no such clear trend was observed. The 2D angular orientation bin having the highest frequency ranged anywhere

between the 20^0-30^0 bin to the 60^0-70^0 bin. It is important to point out here that the 2D orientations of the PSMs are not only dependent on the orientation of the bulk PSB but also on the orientation of the sectioning plane. Therefore a PSM emerging on the surface at an angle θ with the loading axis can, in principle, originate from a PSB in bulk oriented at a very different angle ϕ with the loading axis. However, to the best of the author's knowledge, there is no available literature that quantitatively determines the 3D orientation distribution of PSBs.

It terms of the representation of the 3D angular distributions in Figure 5.30, Figure 5.31 and Figure 5.32, it should be noted that for ease of representation, the bins of discretized 3D angles of 20^0 and 30^0 have been combined. Similarly the bins of discretized 3D angles of 40^0 and 50^0 have also been combined. PSB angular orientation studies conducted in single crystals such as Mughrabi [16] have shown that all PSBs were formed at approximately 45^0 to the loading axis. This is because the maximum critical resolved shear stress (CRSS) for a single crystal occurs at an orientation of 45^0 to the loading axis that is also the orientation with the maximum Schmid factor. However, it is clear from the present study that in case of polycrystal microstructure having randomly oriented grains, instead of having a single preferred 3D orientation, the PSBs exhibit a *distribution* of 3D orientations. The range of 3D angles is between 20^0 and 60^0 and this range is independent of the microstructure. The most frequent 3D orientations for failed samples of all three steels are always within the 40^0-50^0 bin. This indicates that the CRSS still has a role to play in determining the orientations at which the slip occurs. However the cause for the spread in the distribution could be a combination of the lattice friction stresses (or internal stresses) and the orientation distribution of the grains.

Comparing the distributions of the failed samples for the three steels, it is observed that there are no clear differences with all three steels showing a peak in the '40,50' bin. This is agreement with the observations made in section 5.4.3.3 and section 5.4.3.4 suggesting that the path of damage due to PSBs is essentially the same across all steels and that the role of microstructure is much more significant in the initiation of the PSBs. It should be noted that 2D observations alone are not sufficient for reaching this conclusion and that unbiased quantitative estimations using a combination of advanced microscopy as well as stereology are needed for relating the evolution of microstructure with the fatigue damage evolution of the materials.

In terms of variation of the distributions of Figure 5.30 – Figure 5.32 with the number of cycles, it can be noticed that in all three steels a larger range in terms of the 3D orientations is observed in the earlier cycles. The reason behind this observation is not yet certain. However, it is possible that as the cumulative strain increases, PSBs tend to orient themselves closer towards the orientation of maximum resolved shear stress, which is 45^0. It should also be pointed out that at low number of cycles, the number of colonies is also often low. Therefore the statistical sample size of 2D orientations to make accurate quantitative estimations of 3D angular distributions is also comparatively much lower increasing the likelihood of higher sampling error as compared to similar estimations made at higher cycles having a higher number of PSB colonies.

Chapter 6

Summary, Conclusions, and Recommendations

Global geometric evolution of persistent slip bands (PSB) and PSB colonies has been quantitatively characterized as a function of number of fatigue cycles at two strain amplitudes in three AHSS steels having different microstructures. The quantitative characterization was performed using digital image processing and unbiased stereological techniques. SEM and AFM based qualitative microstructural observations, quantitative microstructural data, and data analysis led to development of a simple geometric model for PSB evolution in the AHSS steels of interest. The main observations, results and conclusions of this research are summarized as follows.

1. Atomic force microscopy observations show that formation of individual PSBs initiates at very early stages of the fatigue damage evolution process. For example, the extrusions generated by PSBs emerging at the specimen surface have been observed at 5 cycles in DP 590 steel fatigued at 1% strain amplitude.
2. Scanning electron microscopy revealed that (a) PSBs do not cross the ferrite grain boundaries and martensite/ferrite interfaces associated with the ferrite grains in which they form, (b) even at failure, PSBs are not observed in all ferrite grains, PSBs do not always completely cover the ferrite grains in which they are formed, (c) in DP590 steel containing 25% martensite, PSBs are not observed in the martensite islands even at failure, and (d) although majority of individual PSBs appear to be oriented at an angle of

45 degrees with respect to the loading direction, there is a distribution of the PSB angular orientations.

3. Stereological data reveal that at any given fraction of fatigue life, the ferrite normalized volume fraction of PSB colonies is substantially higher in DP 590 steel compared to HR 590 and DP 980 steels, whereas ferrite normalized volume fractions of PSB colonies in HR 590 and DP 980 steels have comparable values at any given fraction of fatigue life. It is also observed that the rate of change of ferrite normalized volume fraction of PSBs decreases with the number of cycles in the DP 590 steel, whereas it increases with the number of cycles in HR 590 and DP 980 steel. These observations have been explained on the basis of microstructural effects of martensite and differences in the yield stress and carbon content of martensite in DP 590 and DP 980 steels.

4. The path of PSB colony damage evolution is described by variation of ferrite normalized total PSB colony surface area with the ferrite normalized PSB colony volume fraction. Interestingly, in all three AHSS steels, the path of damage evolution is linear, and when appropriately normalized, the paths for all three steel collapse on the same straight line. The behavior of total surface area of individual PSBs shows similar trend.

5. A simple geometric model is proposed for path of evolution of PSB colonies that successfully accounts for observed linear relationship between ferrite normalized total PSB colony surface area and ferrite normalized PSB colony volume fraction.

6. On the basis of the proposed model and agreement of its predictions with the experimental data, it is concluded that as soon as a PSB colony forms it quickly reaches a saturation size (equal to or less than size of ferrite grain in which it is formed) and does

not grow thereafter. PSB colony damage then evolves only through continuous formation of new PSB colonies. Therefore, the PSB colony damage evolution is primarily governed by rate of formation of new PSB colonies (which depends on steel microstructure and strain amplitude) and average grain size/mean intercept of ferrite.

7. A new stereological technique is developed for unbiased estimation of three-dimensional angular orientation distribution of individual PSBs from experimental data on the corresponding two-dimensional apparent angular orientation distribution. The estimated three-dimensional angular orientation distributions show a peak around 45 degrees. However, the three-dimensional angular distributions also contain other angles ranging from 20 to 60 degrees.

Recommendations

From the data obtained in the current work and an analysis of this data along with a detailed review of the available literature in the subject, the importance of the grain size in fatigue related damage, especially due to the formation of PSBs for ferritic HSLA steels and DP steels is clear. It is observed that smaller grain size of ferrite delays the formation of PSB related damage. Thus, it is recommended that for applications that are sensitive to PSB induced crack initiation, materials with smaller ferrite grains will be more desirable in order to increase the fatigue life prior to crack initiation. It is also recommended that further quantitative research be carried out for other materials in order to validate the effect of grain size in PSB related damage.

References

[1] N. Thompson, N. Wadsworth, and N. Louat, "The origin of fatigue fracture in copper," *Philosophical Magazine,* vol. 1, pp. 113-126, 1956/02/01 1956.

[2] Z. Jiang, Z. Guan, and J. Lian, "Effects of microstructural variables on the deformation behaviour of dual-phase steel," *Materials Science and Engineering: A,* vol. 190, pp. 55-64, 1995.

[3] M. Erdogan and R. Priestner, "Effect of martensite content, its dispersion, and epitaxial ferrite content on Bauschinger behaviour of dual phase steel," *Materials Science and Technology,* vol. 18, pp. 369-376, 2002.

[4] S. K. Akay, M. Yazici, A. Bayram, and A. Avinc, "Fatigue life behaviour of the dual-phase low carbon steel sheets," *Journal of Materials Processing Technology,* vol. 209, pp. 3358-3365, 2009.

[5] K. S. Chan, "Roles of microstructure in fatigue crack initiation," *International Journal of Fatigue,* vol. 32, pp. 1428-1447, 2010.

[6] R. Davies, "Influence of martensite composition and content on the properties of dual phase steels," *Metallurgical and Materials Transactions A,* vol. 9, pp. 671-679, 1978.

[7] Y. Kim and M. Fine, "Fatigue crack initiation and strain-controlled fatigue of some high strength low alloy steels," *Metallurgical and Materials Transactions A,* vol. 13, pp. 59-72, 1982.

[8] Z. S. Basinski and S. J. Basinski, "Fundamental aspects of low amplitude cyclic deformation in face-centred cubic crystals," *Progress in Materials Science,* vol. 36, pp. 89-148, 1992.

[9] Z. S. Basinski and S. J. Basinski, "Surface-related phenomena in low amplitude fatigue of fcc metals," *Scripta Metallurgica et Materialia,* vol. 26, pp. 1505-1510, 1992.

[10] T. H. Courtney, *Mechanical Behavior of Materials*, second ed.: McGraw Hill-Higher Education, 2000.

[11] C. Laird and L. Buchinger, "Hardening behavior in fatigue," *Metallurgical and Materials Transactions A,* vol. 16, pp. 2201-2214, 1985.

[12] L. Llanes and C. Laird, "The role of annealing twin boundaries in the cyclic deformation of f.c.c. materials," *Materials Science and Engineering: A,* vol. 157, pp. 21-27, 1992.

[13] P. Lukas and K. L., "Role of persistent slip bands in fatigue," *Philosophical Magazine,* vol. 84, pp. 317-330, 2004/01/21 2004.

[14] J. Polak, "Mechanisms and kinetics of the early fatigue damage in crystalline materials," *Materials Science and Engineering: A,* vol. 468-470, pp. 33-39, 2007.

[15] Y. Yu, J. L. Gu, F. L. Shou, L. Xu, B. Z. Bai, and Y. B. Liu, "Competition mechanism between microstructure type and inclusion level in determining VHCF behavior of bainite/martensite dual phase steels," *International Journal of Fatigue,* vol. 33, pp. 500-506, 2011.

[16] H. Mughrabi, F. Ackermann, and K. Herz, "Persistent slip bands in fatigued Face-Centered and Body Centered cubic metals " presented at the Fatigue Mechanisms, ASTM STP 675, Philadelphia, PA, 1979.

[17] J. A. Ewing and J. C. W. Humfrey, "The Fracture of Metals under Repeated Alterations of Stress," *Philosophical Transactions of the Royal Society, A,* vol. 221, pp. 241-253, 1903.
[18] W. A. Wood, "Formation of Fatigue Cracks," *Philosophical Magazine,* vol. 3, 1958.
[19] M. Hempel, "Fatigue in aircraft structures," *Fracture,* 1959.
[20] W. N. Roberts, "Persistent slip bands in fatigued copper," *Philosophical Magazine,* vol. 20, pp. 675-686, 1969.
[21] L. P, "Fatigue Crack Initiation Mechanisms," in *Encyclopedia of Materials: Science and Technology (Second Edition)*, K. H. J. r. B. Editors-in-Chief:¬†¬†, W. C. Robert, C. F. Merton, I. Bernard, J. K. Edward, M. Subhash*, et al.*, Eds., ed Oxford: Elsevier, 2001, pp. 2882-2891.
[22] P. Lukáš, M. Klesnil, and J. Krejčí, "Dislocations and Persistent Slip Bands in Copper Single Crystals Fatigued at Low Stress Amplitude," *Physica Status Solidi (b),* vol. 27, pp. 545-558, 1968.
[23] K. Pohl, P. Mayr, and E. Macherauch, "Persistent slip bands in the interior of a fatigued low carbon steel," *Scripta Metallurgica,* vol. 14, pp. 1167-1169, 1980.
[24] K. Pohl, P. Mayr, and E. Macherauch, "Shape and structure of persistent slip bands in iron carbon alloys," in *Defects, Fracture and Fatigue, Proceedings of the second internation symposium*, Mont Gambriel, Canada, 1983, pp. 147-159.
[25] H. Mughrabi, "The cyclic hardening and saturation behaviour of copper single crystals," *Materials Science and Engineering,* vol. 33, pp. 207-223, 1978.
[26] P. Lukas and L. Kunz, "Cyclic slip localisation and fatigue crack initiation in fcc single crystals," *Materials Science and Engineering A,* vol. 314, pp. 75-80, 2001.
[27] C. Blochwitz and E. Kahle, "A method for the determination of the cyclic stress-strain curve of presistent slip bands in fatigued single crystals," *Kristall und Technik,* vol. 15, pp. 977-986, 1980.
[28] C. Blochwitz and U. Veit, "Plateau Behaviour of Fatigued FCC Single Crystals," *Crystal Research and Technology,* vol. 17, pp. 529-551, 1982.
[29] G. Gonzalez and C. Laird, "CYCLIC RESPONSE OF DILUTE IRON ALLOYS," *Metallurgical transactions. A, Physical metallurgy and materials science,* vol. 14 A, pp. 2507-2515, 1983.
[30] Z. F. Zhang and Z. G. Wang, "Dependence of intergranular fatigue cracking on the interactions of persistent slip bands with grain boundaries," *Acta Materialia,* vol. 51, pp. 347-364, 2003.
[31] J. Man, M. Petrenec, K. ObrtlÌk, and J. Polak, "AFM and TEM study of cyclic slip localization in fatigued ferritic X10CrAl24 stainless steel," *Acta Materialia,* vol. 52, pp. 5551-5561, 2004.
[32] J. Polak, M. Petrenec, J. Man, and K. Obrtlik, "Initiation and short crack growth in austenitic-ferritic duplex steel-effect of positive mean stress," 2011.
[33] J. Man, K. ObrtlÌk, and J. Polak, "Study of surface relief evolution in fatigued 316L austenitic stainless steel by AFM," *Materials Science and Engineering A,* vol. 351, pp. 123-132, 2003.

[34] S. K. a. P. Ulintz, "Advanced High-Strength Steels Solve Growing Demands for Formability," *Metal Forming,* pp. 24-28, May 2011.
[35] M. C. Kyle Bevans, Brandon Ensor, Jamie F, "Importance of Advanced High-Strength Steels and Electronic Units on the Recycling of Automobiles: A Review," in *AISTech Conference Proceedings*, May, 2013, pp. 266-277.
[36] U. C. Jindal, *Machine Design*: Pearson Education India, 2010.
[37] S. N. Bagchi and K. Prakash, *Industrial Steel Reference Book*. New Delhi: New Age International, 1979.
[38] R. Kuziak, R. Kawalla, and S. Waengler, "Adcanced high strength steels for automotive industry," *Archives of Civil and Mechanical Engineering,* vol. 8, pp. 103-117, 2008.
[39] Y. Toji, T. Yamashita, K. Nakajima, and K. Seto, "Effect of Mn Partitioning during Intercritical Annealing on Following $\gamma \rightarrow \alpha$ Transformation and Resultant Mechanical Properties of Cold-rolled Dual Phase Steels," *ISIJ Int.,* vol. 51, pp. 818-825, 2011.
[40] G. Krauss, "Solidification, segregation, and banding in carbon and alloy steels," *Metallurgical and Materials Transactions B,* vol. 34, pp. 781-792, 2003.
[41] A. R. Salehi, S. Serajzadeh, and A. K. Taheri, "A study on the microstructural changes in hot rolling of dual-phase steels," *Journal of Materials Science,* vol. 41, pp. 1917-1925, 2006/04/01 2006.
[42] R. W. Landgraf, "Fatigue Resistance and Microstructure of Ferrous Alloys," *ASM Handbook: 10th Edition American Society of Materials: Materials Park,* vol. 1996, pp. 605-613, 1996.
[43] B. Leis, "Effect of Surface Condition and Processing on Fatigue Performance," *ASM Handbook,* vol. 19, pp. 314-320, 1996.
[44] L. Llanes, A. Mateo, L. Iturgoyen, and M. Anglada, "Aging effects on the cyclic deformation mechanisms of a duplex stainless steel," *Acta Materialia,* vol. 44, pp. 3967-3978, 1996.
[45] C. Lester, "Analysis of fatigue behavior, fatigue damage and fatigue fracture surfaces of two high strength steels," Masters, Materials Science and Engineering, Georgia Institute of Technology, Atlanta, 2011.
[46] I. Picas, N. Cuadrado, D. Casellas, A. Goez, and L. Llanes, "Microstructural effects on the fatigue crack nucleation in cold work tool steels," *Procedia Engineering,* vol. 2, pp. 1777-1785, 4// 2010.
[47] (July 1). http://www.arcelormittal.com/fce/saturnus/sheets/F_EN.pdf
[48] A. M. Sherman, "Fatigue Properties of High Strength-Low Alloy Steels," *Metallurgical Transactions A,* vol. 6A, pp. 1035-1040, 1975.
[49] A. M. Sherman and R. G. Davies, "Influence of martensite carbon content on the cyclic properties of dual-phase steel," *International Journal of Fatigue,* vol. 3, pp. 195-198, 1981.
[50] A. M. Sherman and R. G. Davies, "The effect of martensite content on the fatigue of a dual-phase steel," *International Journal of Fatigue,* vol. 3, pp. 36-40, 1981.

[51] S. R. Mediratta, V. Ramaswamy, and R. R. P, "Low cycle fatigue behaviour of dual-phase steel with different volume fractions of martensite," *International Journal of Fatigue,* vol. 7, pp. 101-106, 1985.
[52] T. Hilditch, H. Beladi, P. Hodgson, and N. Stanford, "Role of microstructure in the low cycle fatigue of multi-phase steels," *Materials Science and Engineering: A,* vol. 534, pp. 288-296, 2/1/ 2012.
[53] A. Kumar, S. B. Singh, and K. K. Ray, "Influence of bainite/martensite-content on the tensile properties of low carbon dual-phase steels," *Materials Science and Engineering: A,* vol. 474, pp. 270-282, 2008.
[54] A. Bag, K. Ray, and E. Dwarakadasa, "Influence of martensite content and morphology on tensile and impact properties of high-martensite dual-phase steels," *Metallurgical and Materials Transactions A,* vol. 30, pp. 1193-1202, 1999.
[55] A. Bag, K. Ray, and E. Dwarakadasa, "Influence of martensite content and morphology on the toughness and fatigue behavior of high-martensite dual-phase steels," *Metallurgical and Materials Transactions A,* vol. 32, pp. 2207-2217, 2001.
[56] W. Zhongguang, W. Guonan, K. Wei, and H. Haicai, "Influence of the martensite content on the fatigue behaviour of a dual-phase steel," *Materials Science and Engineering,* vol. 91, pp. 39-44, 7// 1987.
[57] P. C. Chakraborti and M. K. Mitra, "Microstructure and tensile properties of high strength duplex ferrite,Äìmartensite (DFM) steels," *Materials Science and Engineering: A,* vol. 466, pp. 123-133, 2007.
[58] S. Sun and M. Pugh, "Properties of thermomechanically processes dual-phase steels containing fibrous martensite," *Materials Science and Engineering,* vol. A335, pp. 298-308, 2002.
[59] V. B. Dutta, S. Suresh, and R. O. Ritchie, "Fatigue crack propagation in dual-phase steels: Effects of ferritic-martensitic microstructures on crack path morphology," *Metallurgical Transactions A,* vol. 15, pp. 1193-1207, 1984/06/01 1984.
[60] F. Ellyin, *Fatigue Damage, Crack Growth and Life Prediction*, 1996.
[61] N. Recho, *Fracture Mechanics and Crack Growth*: Wiley Publications, 2012.
[62] M. J. Hadianfard, "Low cycle fatigue behavior and failure mechanism of a dual-phase steel," *Materials Science and Engineering: A,* vol. 499, pp. 493-499, 2009.
[63] S. P. Bhat, R. S. Cline, and Y. W. Chung, "Fatigue crack initiaion in iron and a high strength low alloy steel," presented at the Morris E. Fine Symposium, Detroit, Michigan, 1991.
[64] M. Fine, "Fatigue resistance of metals," *Metallurgical and Materials Transactions A,* vol. 11, pp. 365-379-379, 1980.
[65] J. T. McGrath and W. J. Bratina, "Interaction of dislocations and precipitates in quench-aged iron-carbon alloys subjected to cyclic stressing," *Acta Metallurgica,* vol. 15, pp. 329-339, 2// 1967.
[66] S. P. Bhat and C. Laird, "Cyclic Stress-Strain Response and Damage Mechanisms at High Temperature," *ASTM STP 675,* p. 592, 1979.

[67] A. T. Winter, "A model for the fatigue of copper at low plastic strain amplitudes," *Philosophical Magazine,* vol. 30, pp. 719-738, 1974.
[68] L. M. Brown, "Dislocation substructures and the initiation of cracks by fatigue," *Metal Science,* vol. 11, pp. 315-320(6), 1977.
[69] B. Šesták and A. Seeger, "The Relationship between the Work-Hardening of B.C.C. and F.C.C. Metals," *physica status solidi (b),* vol. 43, pp. 433-444, 1971.
[70] H. Mughrabi, "Dislocations and Properties of Real Materials," London, 1984, pp. 244-260.
[71] H. Mughrabi and C. Wüthrich, "Asymmetry of slip and shape changes during cyclic deformation of α-iron single crystals," *Philosophical Magazine,* vol. 33, pp. 963-984, 1976/06/01 1976.
[72] H. D. Nine, "Asymmetric deformation in fatigue of body‐centered‐cubic single crystals," *Journal of Applied Physics,* vol. 44, pp. 4875-81, 1973.
[73] D. V. Wilson and J. K. Tromans, "Effects of strain ageing on fatigue damage in low-carbon steel," *Acta Metallurgica,* vol. 18, pp. 1197-1208, 1970.
[74] A. S. Cheng and C. Laird, "The high cycle fatigue life of copper single crystals tested under plastic-strain-controlled conditions," *Materials Science and Engineering,* vol. 51, pp. 55-60, 1981.
[75] F. V. L. Jr. and R. C. Jones, *Metallurgical Transactions I,* 1970.
[76] S. P. Bhat and M. E. Fine, "Fatigue crack nucleation in iron and a high strength low alloy steel," *Materials Science and Engineering A,* vol. 314, pp. 90-96, 2001.
[77] M. R. Krishnadev, R. Ghosh, and A. Galibois, "EFFECT OF LOW-TEMPERATURE ON THE FATIGUE PROPERTIES OF TWO HSLA (HIGH STRENGTH LOW ALLOY) PIPELINE STEELS," *Fatigue & Fracture of Engineering Materials & Structures,* vol. 2, pp. 107-119, 1979.
[78] F. Boehme, K. Hidaka, and J. R. Weertman, "PSB observation in copper fatigued at one half the melting temperature," *Scripta Metallurgica et Materialia,* vol. 24, pp. 2341-2346, 12// 1990.
[79] T. P. Gabb, R. V. Miner, and J. Gayda, "The tensile and fatigue deformation structures in a single crystal Ni-base superalloy," *Scripta Metallurgica,* vol. 20, pp. 513-518, 4// 1986.
[80] K. Obrtlik, P. Lukas, and J. Polak, *Low Cycle Fatigue and Elasto-Plastic Behavior of Materials*. Amsterdam: Elsevier, 1998.
[81] H. Mughrabi, K. Herz, and X. Stark, "The effect of strain-rate on the cyclic deformation properties of α-iron single crystals," *Acta Metallurgica,* vol. 24, pp. 659-668, 7// 1976.
[82] M. D. Sangid, "The physics of fatigue crack initiation," *International Journal of Fatigue,* vol. 57, pp. 58-72, 12// 2013.
[83] D. Davidson, K. Chan, R. McClung, and S. Hudak, "4.05 - Small Fatigue Cracks," in *Comprehensive Structural Integrity*, I. Milne, R. O. Ritchie, and B. Karihaloo, Eds., ed Oxford: Pergamon, 2003, pp. 129-164.
[84] H. Mughrabi, "Specific features and mechanisms of fatigue in the ultrahigh-cycle regime," *International Journal of Fatigue,* vol. 28, pp. 1501-1508, 2006.

[85] P. Lukas, "Fatigue Crack Nucleation and Microstructure," *ASM Handbook: Fatigue and Fracture,* vol. 19, pp. 96-109, 1996.
[86] K. Tanaka and T. Mura, "A Dislocation Model for Fatigue Crack Initiation," *Journal of Applied Mechanics,* vol. 48, pp. 97-103, 1981.
[87] M. R. Lin, M. E. Fine, and T. Mura, "Fatigue crack initiation on slip bands: Theory and experiment," *Acta Metallurgica,* vol. 34, pp. 619-628, 1986.
[88] T. Mura and Y. Nakasone, "A Theory of Fatigue Crack Initiation in Solids," *Journal of Applied Mechanics,* vol. 57, pp. 1-6, 1990.
[89] M. Fine and S. Bhat, "A model of fatigue crack nucleation in single crystal iron and copper," *Materials Science and Engineering: A,* vol. 468-470, pp. 64-69, 2007.
[90] S. Suresh, *Fatigue of Materials* vol. 2: Cambridge University Press, 1998.
[91] H. J. Roven and E. Nes, "Cyclic deformation of ferritic steel—I. Stress-strain response and structure evolution," *Acta Metallurgica et Materialia,* vol. 39, pp. 1719-1733, 8// 1991.
[92] K. Pohl, P. Mayr, and E. Macherauch, "Cyclic deformation behavior of a low carbon steel in the temperature range between room temperature and 850 K," *International Journal of Fracture,* vol. 17, pp. 221-233, 1981/04/01 1981.
[93] T. Petersmeier, U. Martint, D. Eifler, and H. Oettelt, "Cyclic fatigue loading and characterization of dislocation evolution in the ferritic steel X22CrMoV121," *International Journal of Fatigue,* vol. 20, pp. 251-255, // 1998.
[94] C. L. Xie, S. Ghosh, and M. Groeber, "Modeling Cyclic Deformation of HSLA Steels Using Crystal Plasticity," *Journal of Engineering Materials and Technology,* vol. 126, pp. 339-352, 2004.
[95] Z. Wang and C. Laird, "Cyclic stress—strain response of polycrystalline copper under fatigue conditions producing enhanced strain localization," *Materials Science and Engineering,* vol. 100, pp. 57-68, 4// 1988.
[96] S. P. Bhat and C. Laird, "The cyclic stress-strain curves in monocrystalline and polycrystalline metals," *Scripta Metallurgica,* vol. 12, pp. 687-692, 8// 1978.
[97] P. Kettunen, T. Lepisto, and V. T. Kuokkala, "CYCLING STRAINING AND FATIGUE AT CONSTANT AND VARIABLE AMPLITUDES," *Scandinavian Journal of Metallurgy,* vol. 14, pp. 121-126, 1985.
[98] C. Laird, F. Lorenzo, and A. S. Cheng, "Design Against Variable Amplitude Fatigue — an approach through Cyclic Stress-Strain Response," in *Strength of Metals and Alloys (ICSMA 6)*, R. C. Gifkins, Ed., ed: Pergamon, 1982, pp. 1147-1163.
[99] J. Polák, "4.20 - Fatigue of Steels," in *Comprehensive Structural Integrity*. vol. 4, ed, 2007, pp. 504-537.
[100] S. Sinha and S. Ghosh, "Modeling cyclic ratcheting based fatigue life of HSLA steels using crystal plasticity FEM simulations and experiments," *International Journal of Fatigue,* vol. 28, pp. 1690-1704, 12// 2006.
[101] S. Zhengming and W. Zhongguang, "The Study of Dual-phase Steel after Cyclic Deformation at Various Strain Amplitudes," *Journal of Materials Science and Technology,* vol. 6, 1989.

[102] Y. S. Zheng, Z. G. Wang, and S. H. Ai, "Effect of dislocation substructure of crack tip on near fatigue threshold in dual-phase steels," *Materials Science and Engineering: A,* vol. 176, pp. 393-396, 1994.
[103] T. Hilditch, I. Timokhina, L. Robertson, E. Pereloma, and P. Hodgson, "Cyclic Deformation of Advanced High-Strength Steels: Mechanical Behavior and Microstructural Analysis," *Metallurgical and Materials Transactions A,* vol. 40, pp. 342-353, 2009/02/01 2009.
[104] A. M. Sarosiek and W. S. Owen, "The work hardening of dual-phase steels at small plastic strains," *Materials Science and Engineering,* vol. 66, pp. 13-34, 9/1/ 1984.
[105] J. Kang, Y. Ososkov, J. D. Embury, and D. S. Wilkinson, "Digital image correlation studies for microscopic strain distribution and damage in dual phase steels," *Scripta Materialia,* vol. 56, pp. 999-1002, 6// 2007.
[106] P. Neumann, "Coarse slip model of fatigue," *Acta Metallurgica,* vol. 17, pp. 1219-1225, 9// 1969.
[107] H. Mughrabi, "Cyclic Slip Irreversibilities and the Evolution of Fatigue Damage," *Metallurgical and Materials Transactions A,* vol. 40, pp. 1257-1279, 2009.
[108] S. D. Antolovich and R. W. Armstrong, "Plastic Strain Localization in Metals: Origins and Consequences," *Progress in Materials Science*.
[109] J. C. Grosskreutz and H. Mughrabi, *Description of the work-hardened strucutre at low temperature in cyclic deformation*. Cambridge, MA: MIT Press, 1975.
[110] H. Mughrabi, "On the Grain-Size Dependence of Metal Fatigue: Outlook on the Fatigue of Ultrafine-Grained Metals," in *Investigations and Applications of Severe Plastic Deformation*. vol. 80, T. Lowe and R. Valiev, Eds., ed: Springer Netherlands, 2000, pp. 241-253.
[111] P. Lukáš and L. Kunz, "Effect of low temperatures on the cyclic stress-strain response and high cycle fatigue life of polycrystalline copper," *Materials Science and Engineering: A,* vol. 103, pp. 233-239, 9// 1988.
[112] P. Lukáš, L. Kunz, and J. Krejčí, "Effect of slip planarity on the cyclic stress-strain curve, dislocation structure and surface relief in f.c.c. single crystals," *Scripta Metallurgica et Materialia,* vol. 26, pp. 1511-1516, 5/15/ 1992.
[113] S. I. Hong and C. Laird, "FATIGUE CRACK INITIATION AND GROWTH BEHAVIOR OF Cu-16 at.% A1 SINGLE CRYSTALS," *Fatigue & Fracture of Engineering Materials & Structures,* vol. 14, pp. 143-169, 1991.
[114] J. POLÁK, S. DEGALLAIX, and G. DEGALLAIX, "The role of cyclic slip localization in fatigue damage of materials," *Journal of Physics IV France,* vol. 3, pp. 679-684, 1993.
[115] J. Man, K. Obrtllk, and J. Polak, "Extrusions and intrusions in fatigued metals. Part 1. State of the art and history,Ä†," *Philosophical Magazine,* vol. 89, pp. 1295-1336, 2009/06/01 2009.
[116] Z. F. Zhang, Z. G. Wang, and Y. M. Hu, "Fatigue crack initiation and fracture behavior of a copper bicrystal with a perpendicular grain boundary," *Materials Science and Engineering: A,* vol. 269, pp. 136-141, 8/30/ 1999.

[117] A. Hunsche and P. Neumann, "Quantitative measurement of persistent slip band profiles and crack initiation," *Acta Metallurgica,* vol. 34, pp. 207-217, 1986.
[118] P. J. E. Forsyth, "Exudation of Material from Slip Bands at the Surface of Fatigued Crystals of an Aluminium-Copper Alloy," *Nature Methods,* vol. 171, pp. 172-173, 1953.
[119] W. D. Dover and E. J. D. Jones, "The initiation of fatigue cracks in copper," *Journal of Applied Physics,* vol. 18, p. 1257, 1967.
[120] "Extrusions and intrusions in fatigued metals. Part 1. State of the art and history,Ä†," *Philosophical Magazine,* vol. 89, p. 1295, 2009.
[121] U. Essmann, "Irreversibility of cyclic slip in persistent slip bands of fatigued pure f.c.c. metals," *Philosophical Magazine A,* vol. 45, pp. 171-190, 1982/01/01 1982.
[122] Mughrabi, "On the life-controlling microstructural fatigue mechanisms in ductile metals and alloys in the gigacycle regime," *Fatigue & Fracture of Engineering Materials & Structures,* vol. 22, pp. 633-641, 1999.
[123] W. J. Baxter and T. R. McKinney, "Growth of slip bands during fatigue of 6061-T6 aluminum," *Metallurgical Transactions A,* vol. 19, pp. 83-91, 1988/01/01 1988.
[124] B. Šesták, Z. Vicherková, V. Novák, S. Libovický, and J. Brádler, "Cyclic plastic deformation of Fe–13.6 wt% Cr single crystals," *physica status solidi (a),* vol. 104, pp. 79-93, 1987.
[125] J. Poláak, A. Vašek, and K. Obrtlíak, "FATIGUE DAMAGE IN TWO STEP LOADING OF 316L STEEL I. EVOLUTION OF PERSISTENT SLIP BANDS," *Fatigue & Fracture of Engineering Materials & Structures,* vol. 19, pp. 147-155, 1996.
[126] A. Gironès, P. Villechaise, A. Mateo, M. Anglada, and J. Méndez, "EBSD studies on the influence of texture on the surface damage mechanisms developed in cyclically loaded aged duplex stainless steels," *Materials Science and Engineering: A,* vol. 387–389, pp. 516-521, 12/15/ 2004.
[127] C. A. N. Lanzillotto and F. B. Pickering, "Structure–property relationships in dual-phase steels," *Metal Science,* vol. 16, pp. 371-382, 1982.
[128] M. Sarwar, R. Priestner, and E. Ahmad, "Influence of martensite volume fraction on fatigue limit of a dual-phase steel," *Journal of Materials Engineering and Performance,* vol. 11, pp. 274-277, 2002.
[129] Y. Murakami, S. Kodama, and S. Konuma, "Quantitative evaluation of effects of non-metallic inclusions on fatigue strength of high strength steels. I: Basic fatigue mechanism and evaluation of correlation between the fatigue fracture stress and the size and location of non-metallic inclusions," *International Journal of Fatigue,* vol. 11, pp. 291-298, 1989.
[130] H. Liao, Y. Sun, and G. Sun, "Correlation between mechanical properties and amount of dendritic α-Al phase in as-cast near-eutectic Al–11.6% Si alloys modified with strontium," *Materials Science and Engineering: A,* vol. 335, pp. 62-66, 9/25/ 2002.
[131] E. E. Underwood, *Quantitative Stereology*: Addison Wesley, 1970.

[132] P. R. Mouton, *Principles and practices of unbiased stereology: An introduction for bioscientists*: The Johns Hopkins University Press, 2002.
[133] R. T. DeHoff and F. N. Rhnes, "Quantitative Microscopy," *McGraw Hill,* 1968.
[134] A. Gokhale, "Quantitative Characterization and Representation of Global Microstructural Geometry," *ASM Handbook* vol. IX: Metallography and Microstructures, 2004.
[135] F. Chayes, *Petrographic Modal Analysis*: John Wiley, 1956.
[136] S. A. Saltykov, *Stereometric Metallography*, 2nd ed. Moscow: Metallurgizdat, 1958.
[137] L. M. Cruz-Orive, "On the precision of systematic sampling: a review of Matheron's transitive methods," *Journal of Microscopy,* vol. 153, pp. 315-333, 1989.
[138] L. M. C. Drive, "Systematic Sampling in Stereology," *Bulletin of International Statistical Institute,* vol. 55, pp. 451-468, 1993.
[139] L. M. Cruz-Orive and X. Gual-Arnau, "Precision of circular systematic sampling," *Journal of Microscopy,* vol. 207, pp. 225-242, 2002.
[140] J. E. Hilliard, "Specification and Measurement of Microstructural Anisotropy," *Transactions of the Metallurgical Society of AIME* vol. 224, pp. 1201-1211, 1962.
[141] J. E. Hilliard and J. W. Cahn, "An Evaluation of Procedures in Quantitative Metallography for Volume-Fraction Analysis," in *The Selected Works of John W. Cahn*, ed: John Wiley & Sons, Inc., 2013, pp. 63-64.
[142] H. J. Gundersen and E. B. Jensen, "The Efficiency of Systematic Sampling in Stereology and Its Prediction," *Journal of Microscopy* vol. 121, pp. 65-73, 1987.
[143] H. J. G. Gundersen, E. B. V. Jensen, K. KiÊU, and J. Nielsen, "The efficiency of systematic sampling in stereology — reconsidered," *Journal of Microscopy,* vol. 193, pp. 199-211, 1999.
[144] C. S. Smith and L. Guttman, " Measurement of Internal Boundaries in Three-Dimensional Structures by Random Sectioning," *Transaction of AIME,* vol. 97, p. 81, 1953.
[145] Baddeley A. J., Gundersen H. J. G, and C.-O. L. M., "Estimation of surface area from vertical sections," *Journal of Microscopy,* vol. 142, pp. 259-276, 1986.
[146] A. Gokhale and W. Drury, "Efficient measurement of microstructural surface area using trisector," *Metallurgical and Materials Transactions A,* vol. 25, pp. 919-928, 1994.
[147] A. M. Gokhale and E. E. Underwood, "A general method for estimation of fracture surface roughness: Part I. Theoretical aspects," *Metallurgical Transactions A,* vol. 21, pp. 1193-1199, 1990/05/01 1990.
[148] A. M. Gokhale, "Estimation of bivariate size and orientation distribution of microcracks," *Acta Materialia,* vol. 44, pp. 475-485, 1996.
[149] ASTM, "Standard Practice for Strain Controlled Fatigue Testing," vol. 606-04, ed, 2004.
[150] H. Mughrabi, K. Herz, and F. Ackermann, "A comparison of steady-state cyclic deformation of fcc and bcc metals," in *Proceedings of the 4th International Conference on the Strength of Metals and Alloys* 1976, pp. 1244-1248.

[151] H. Mughrabi, "Fatigue, an everlasting materials problem - still en vogue," *Procedia Engineering,* vol. 2, pp. 3-26, 2010.
[152] J. E. Hilliard and J. W. Cahn, "An evaluation of Procedures in Quantitative Metalography for Volume Fraction Analysis," *Trasactions of AIME,* vol. 221, pp. 344-354, 1961.
[153] C. A. Schneider, W. S. Rasband, and K. W. Eliceiri, "NIH Image to ImageJ: 25 years of image analysis," *Nature Methods,* vol. 9, pp. 671-675, 2012.
[154] ASTM, "Standard Test Methods for Determining Average Grain Size," vol. E112 - E10, ed: ASTM International, 2012.
[155] J. H. Hollomon, "Tensile Deformation," *AIME: Transaction of Iron Steel Div,* vol. 162, pp. 268-289, 1945.
[156] M. A. Meyers and K. K. Chawla, *Solid Solution, Preciptation, and Dispersion Hardening*: Cambridge University press, 2009.
[157] C. Gupta, J. Nagchaudhury, J. K. Chakravartty, and R. C. Prasad, "Cyclic stress-strain characteristics of two microalloyed steels," *Materials Science & Technology,* vol. 25, pp. 760-769, 2009.
[158] M. Sarwar and R. Priestner, "Influence of ferrite-martensite microstructural morphology on tensile properties of dual-phase steel," *Journal of Materials Science,* vol. 31, pp. 2091-2095, 1996.
[159] N. Farabi, D. L. Chen, and Y. Zhou, "Tensile Properties and Work Hardening Behavior of Laser-Welded Dual-Phase Steel Joints," *Journal of Materials Engineering and Performance,* vol. 21, pp. 222-230, 2012/02/01 2012.
[160] N. J. Kim and G. Thomas, "Effects of morphology on the mechanical behavior of a dual phase Fe/2Si/0.1C steel," *Metallurgical Transactions A,* vol. 12, pp. 483-489, 1981/03/01 1981.
[161] T. Kruml and J. Polák, "Fatigue softening of X10CrAl24 ferritic steel," *Materials Science and Engineering: A,* vol. 319–321, pp. 564-568, 12// 2001.
[162] M. R. Mitchell, *Fundamentals of Modern Fatigue Analysis for Design* vol. 19. Materials Park, OH: ASM International, 1996.
[163] S. R. Mediratta, V. Ramaswamy, and P. R. Rao, "Influence of ferrite-martensite microstructural morphology on the low cycle fatigue of a dual-phase steel," *International Journal of Fatigue,* vol. 7, pp. 107-115, 4// 1985.
[164] C. R. Brooks, *Principles of the Heat Treatment of Plain Carbon and Low Alloy Steels*. Materials Park OH: ASM International, 1996.
[165] P. Chen, H. Ghassemi-Armaki, S. Kumar, A. Bower, S. Bhat, and S. Sadagopan, "Microscale-calibrated modeling of the deformation response of dual-phase steels," *Acta Materialia,* vol. 65, pp. 133-149, 2/15/ 2014.
[166] R. W. Cahn and P. Hassen, *Physical Metallurgy*, Fourth ed. vol. 3: North Holland, 1996.
[167] A. M. Gokhale, "Estimation of average size of convex particles," *Metallurgical Transactions A,* vol. 17, pp. 742-745, 1986/04/01 1986.
[168] J. Polak, J. Man, and K. ObrtlÌk, "AFM evidence of surface relief formation and models of fatigue crack nucleation," *International Journal of Fatigue,* vol. 25, pp. 1027-1036, 2003.
[169] P. W. Davies and W. B., "An experiment on void nucleation during creep," *Journal of the Institute of Metals,* vol. 90, pp. 470-72, 1961-62.

[170] Scriven R.A. and W. H.D., "The derivation of angular distributions of planes by sectioning methods," *Transactions of the Metals Society,* vol. 233, pp. 1593-1602, 1965.